Characterization of the flow field and shape of de-fluidized regions in the wake of large submerged objects in small particle fluidized beds

by

Prakash R. Rao

A Dissertation submitted to the

Graduate School – New Brunswick

Rutgers, The State University of New Jersey

in partial fulfillment of the requirements

for the degree of

Doctor of Philosophy

Graduate Program in Mechanical and Aerospace Engineering

written under the direction of

Professor Michael R. Muller

and approved by

New Brunswick, New Jersey

May 2012

`

Abstract of the Dissertation

Characterization of the flow field and shape of de-fluidized regions in the wake of large submerged objects in small particle fluidized beds

By Prakash Rao

Dissertation Director:

Dr. Michael Muller

The structure of the de-fluidized hood, an area of un-fluidized material found in the wake downstream of submerged objects, is studied with special interest on the internal fluidization structure and shape of the hood. Previously, the structure of the region was determined based on indirect photographic evidence rather than direct measurement. Also, the wake region had been considered to be entirely packed and focus had only been on the de-fluidized region in the near wake.

In the present study, an experimental set-up was created which allowed for spheres and disks of various radii to be suspended within a fluidized bed of Geldart A particles. The force imparted by the wake region at various depths on a submerged object was measured providing insight into the downstream extent of the region, as well as the nature of the fluidization within the wake. Additionally, bed collapse with an object near the surface was studied to gain insight into particle mobility within the wake. Experiments were conducted to measure the maximum normal force supported by the wake region, as well as the shear and drag, at various depths above the submerged object surface providing an indirect measure of the velocity within the wake and its effect on neighboring structures.

The results show the region to have several fluidization states: a dead region, a stagnant percolating region, a large percolating region of mobile particles, and an expanding region. The overall shape is found to resemble cylinder with a rounded top. Voids generated at the hemisphere of the submerged objects and particle circulation into and out of the region were found to play a key role in determining the shape and height of the hood, as well as playing a key role in the re-fluidization of the region. Using the data collected from the experiments, a model of the weight force imparted by the de-fluidized region on a submerged object was developed.

Acknowledgment

When Hakeem Olajuwon won the 1994 NBA MVP award, he brought his whole team onto the court to accept the award because no individual accomplishment can be achieved without great teammates. My research is the same.

First and foremost, I would like to thank my adviser, Dr. Michael Muller. While he has taught me a great deal about the fundamentals of engineering, his greatest lessons have been to always strive for good data and to always ask “why?”, particularly when something does not work.

I would also like to thank Mr. John Petrowski for all his help with designing and constructing the experimental apparatuses used herein.

I would like to thank all the staff and students at CAES. All the staff and students that have come and gone have made my experience so much more enjoyable. I would like to thank in particular Thor Duann for his help in acquiring data, and Mike Muller, Jill Mesonas and Don Kasten.

I would like to thank my wife for supporting me through all these years. From our first Calc 3D exam to writing this dissertation, she has been with me, encouraging me every step of the way. I would like to thank my parents for supporting me throughout my 23 years of education and my brother for reminding me that there is life outside of engineering.

Table of Contents

List of tables

List of figures

Chapter 1 Introduction

1.1 Motivation for research

Fluidization plays a key role in several industrial applications, such as coal combustion, gasification, oil refining, pharmaceutical drug manufacturing, and powder drying. Within the power generation sector, fluidized bed combustion of coal represents a cleaner method compared to the traditional pulverized coal methods. By aerating the particles such that they are not in contact with each other, a large surface area for reaction is guaranteed. Yet the particles are large enough such that they act as a lumped mass, ensuring uniform temperature throughout the bed. By maintaining a constant temperature within the combustion chamber, hot spots are avoided, and combustion can occur at lower temperatures, generally around 700^0 C - 800^0 C. At these temperatures, thermal NO_x will not form. Furthermore, limestone can be added to the bed and will combine with the SO_x created during combustion to create gypsum, which can be sold.

Fluidization is conducted within a fluidized bed. A fluidized bed is a chamber that consists of three components: a plenum, a perforated sheet, and a chamber. Gas enters into the plenum where it buffers and reaches a uniform pressure and effectively zero velocity across the plenum. The air then passes through a perforated sheet which serves to separate the particles from the plenum. A pressure drop is created due to the weight of the particles and the blockage created by the perforated sheet. As the air passes through the particles in the chamber, it begins to reduce the contact force between adjacent particles. This regime is called percolation. As the air velocity is increased further, the particles separate from each other and are levitated until the air velocity matches the terminal velocity of the particles. At this velocity, the particles are considered fluidized.

This levitation is accompanied by a rise in surface level of the bed. At fluidization, the particles take on some of the properties of a fluid: the bed can be stirred with minimal resistance, the free surface of the bed remains parallel to the plane of the floor when the bed is tilted, an object of greater density than the fluidized particles sinks when placed on the bed surface.

In a bed having uniform size and shape spherical particles, fluidization will occur with minimal local deviation from the bulk characteristics. However, in most applications, the particles that are fluidized are not of the same size or shape. Furthermore, the fluidized bed is just one step of a larger process and objects within the bed, such as heat exchanger tubes or internal baffles, will exist in order to achieve the end results, i.e. make steam for a steam turbine. Additionally, electrostatic forces and humidity may cause clumping of particles. All of these practical considerations cause inhomogeneity within the fluidized system and local variations in the fluidization characterization. For the purposes of predicting the performance of a fluidized bed (examples include heat transfer from the bed to a heat exchanger, composition of a drug manufactured in a fluidized bed, time required for powder drying), these variations within the bed should be taken into account.

For example, the amount of heat imparted to a heat exchanger within a fluidized bed is proportional to the number of new coal particles it comes into contact with. However, downstream of the tubes, there is a local velocity deficit which leads to a region of seemingly “dead” or immobile particles. This stagnant cap will hinder the heat transfer to the tube, thus lowering the overall efficiency of the combustion system. It therefore becomes relevant to either account for the loss associated with the stagnant cap

when designing the fluidized bed reactor or to design heat exchanger tubes such that the bed is equally fluidized upstream and downstream of the tube(s).

1.2 Objectives of thesis

The research conducted and presented for this thesis provides a better understanding of the downstream region past a submerged object within a fluidized bed. Previously, researchers used optical techniques to determine the size and shape of the de-fluidized region [Rees 2005, Grace and Hosney 1985, Hager and Schrag 1976, Kulkarni 1987]. As some researchers point out [Kulkarni 1987], it is difficult to determine the boundary between the de-fluidized region and the fluidized region from the pictures, and more research is needed to determine the levels of de-fluidization within the region. Those that did not use optical measurement techniques only studied the region in the near wake [Rathbone 1989].

In the present work, direct measurements are used to determine the shape, size and structure of the entire de-fluidized hood region (may be referred to as the ‘stagnant cap’ or simply the‘hood’). Also, the mechanism by which the hood re-fluidizes is investigated. Specifically, the nature of the fluidization – meaning whether or not the de-fluidized region is completely ‘dead’ – is determined. The effect of voids – pockets of excess gas - and particle circulation on the shape of the hood is shown to be important. With the results, a model of the forces on a submerged object is constructed based on the shape, size and levels of de-fluidization within the hood. Experiments are conducted with round and ground particles using spheres and disks of various diameters as submerged objects, and the effect of these parameters on the shape and structure of the de-fluidized region and on the overall force balance of the hood are examined.

The findings can be used to better predict the heat and mass transfer around a submerged heat exchanger tube, as well as aid in designing heat exchanger tube banks to minimize the effect of one tube on another.

1.3 Fluidized bed operation

A background on the relevant factors concerning fluidized bed operation is provided in this section.

1.3.1 Stages of fluidization

The fluidized material is initially at rest with no air supplied to the bed. As air is slowly introduced, the pressure drop through the bed increases and the surface level increases. Figure 1 [Howard 1989] shows the relation between bed pressure drop and the gas velocity. Figure 2 **[**Jackson 2000] shows the relation between bed height and gas velocity.

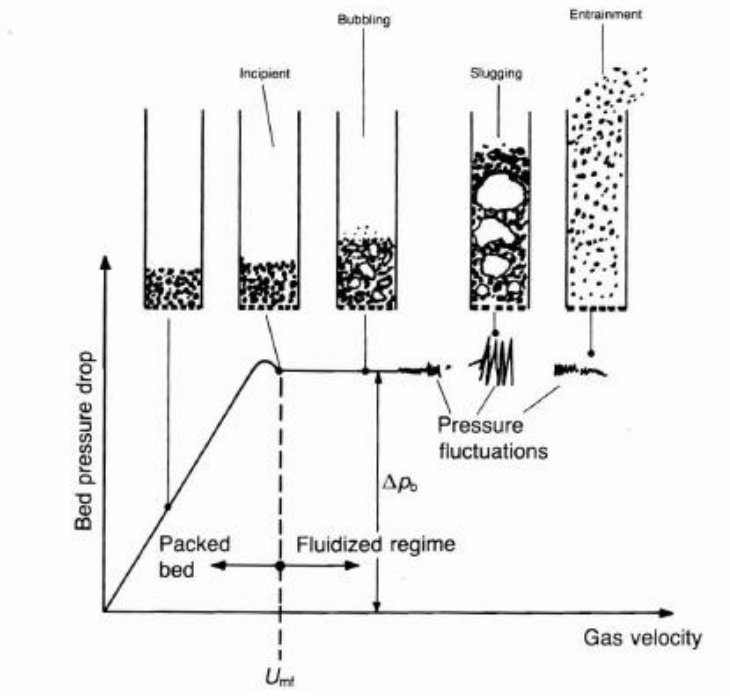

Figure 1: Pressure drop versus gas velocity and the accompanying stages of fluidization [Howard 1989]

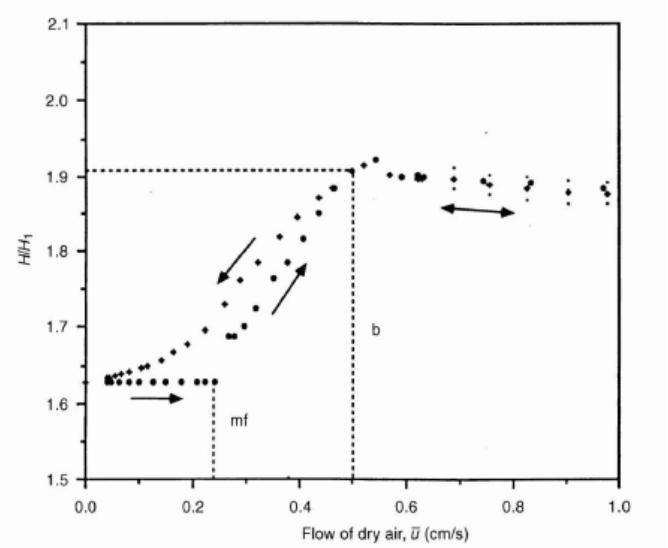

Figure 2: Bed height changes with increase in flow rate [Jackson 2000]

Studied together, the two graphs, illustrate the stages of fluidization. Initially, when gas is passed through the bed of particles, the pressure drop increases, but there is no expansion of the bed. This regime is called percolation. The particles within the bed are still packed and in contact with each other, but the contact force between adjacent particles is reduced by the drag imposed by the upward flowing gas.

Percolation continues until the drag on the particles imposed by the gas velocity matches the weight of the particles. This is known as the minimum fluidization velocity, U_{mf}, of the bed. Beyond this velocity, the bed begins to expand and the particles are no longer in permanent contact with each other, although they do collide with each other. Also, the pressure drop through the bed reduces. As the interparticle spacing increases, the interstitial air velocity decreases resulting in a slight pressure drop. As the gas flow increases, the bed will continue to expand but the pressure drop will remain relatively constant.

Depending on the particle size, density and the gas velocity, voids may form at gas velocities in excess of U_{mf}. Voids are pockets of gas that may appear as 'bubbles', but do not have any surface tension. Voids play a key role in particle mixing. As they travel through the bed, they pull air into them and are followed by a trail of particles. The voids burst at the surface, redistributing the particles in its wake. Figure 3 [Jackson 2000] shows a photograph of a void traveling through a bed.

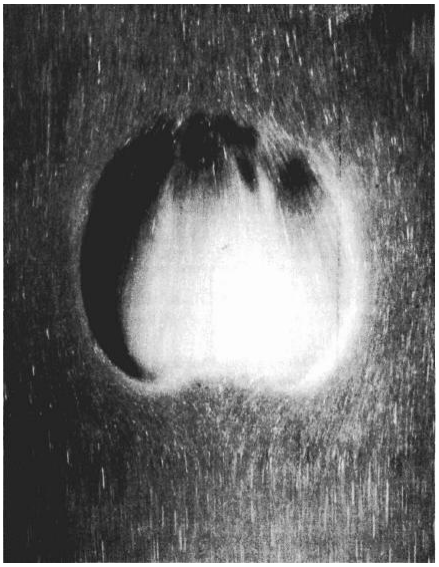

Figure 3: Voids shape in a fluidized bed [Jackson 2000]

Once the gas supply to the bed is shut off, the bed will return to its 'dead' state meaning that the particles will no longer be suspended due to the lack of any as flow. The process is described by Rietama [1991]. First, all of the excess gas within the bed trapped as bubbles will vacate. The remaining gas will vacate next until the bed returns to its packed state. The process is known as bed collapse.

1.3.2 Particle characterization

The particle to be fluidized is at the heart of fluidization. The properties of these particles characterize the manner in which they will fluidize.

Initially, before gas is supplied to the fluidized bed, the particles are at rest and are said to be packed or dead. The manner in which the particles pack is dependent upon their shape and size distribution. The simplest packing structure would be an ordered packing of monosized particles of perfectly geometric shapes, such as spheres, diamonds, cubes, etc.

An ordered packing is such that a long range structure exists. In contrast, random packing would exhibit no such structure. Figure 4 [German 1989] shows the difference between ordered and random packing for spheres.

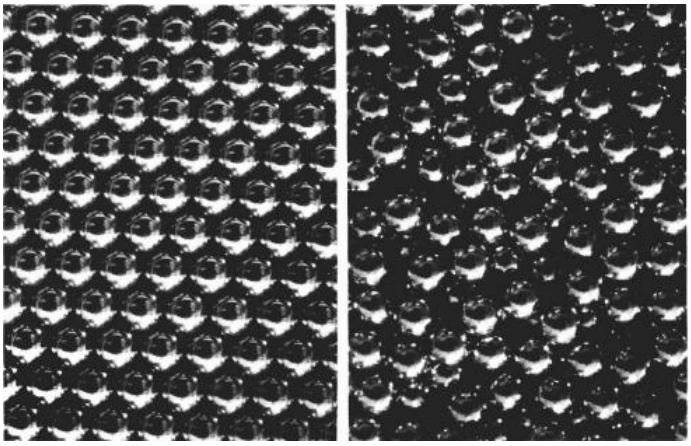

Figure 4: Ordered (left) and random or loose (right) packing of spheres [German 1989]

Table 1 (reproduced from German 1989) shows the coordination number, the packing density, and the porosity for various packing types. The packing type refers to the geometric shape of the particle, the coordination number refers to the number of contact points between the particle and its neighboring particles, the packing density

refers to the ratio of volume occupied by particles to the total volume, and the porosity is the ratio of air volume to total volume within the packing. When dealing with fluidized beds, the porosity is a commonly measured parameter used to determine the degree of fluidization. It is sometimes reported as the voidage, which is

$$\text{Voidage} = 1 - \text{porosity}$$

Packing Type	Coordination number	Packing density	Porosity
Face-centered cubic	12	0.7405	0.2595
	11	0.712	0.2880
Simple cubic	6	0.5236	0.4764
	5	0.4031	0.5969
Diamond	4	0.3401	0.6599

Table 1: Packing densities for various packing types and coordination numbers [taken from German 1989]

When the packing is ordered and of monosize particles, the particle density can be predicted. However, when particles are multisized, irregularly shaped and ordered randomly, the packing becomes more stochastic. This is seen in Figure 5, which shows the variation in packing density with particle size variation [German 1989].

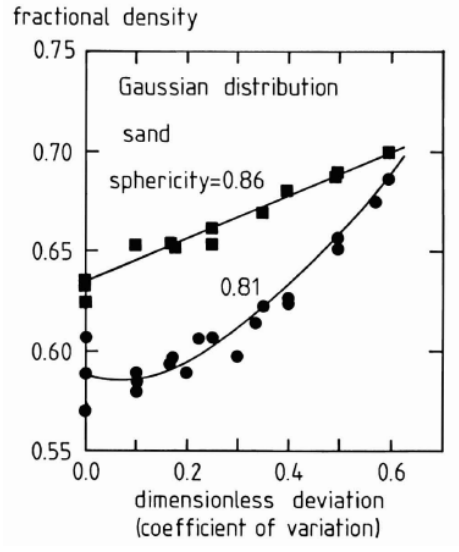

Figure 5: Packing density (fractional density) of multisized shape and size particles [German 1989]

Sphericity is a term used to describe the shape of an irregular shaped particle. It is defined by Equation 1.

$$\varphi = \frac{surface\ area\ of\ a\ sphere\ of\ the\ same\ volume\ as\ the\ particle}{surface\ area\ of\ the\ particle}$$

Equation 1

A perfectly round particle will have a sphericity of 1. A lower sphericity, indicates a more irregularly shaped particle.

Vibration can also affect the degree of packing – particularly for particles with low sphericities. If a bed of particles is vibrated, the particles will pack "tighter", meaning that they will re-orient themselves so as to minimize any space between adjacent particles. The packing of round particles with a sphericity of 1 will not be affected by vibration because they will already pack in a manner such that the space between adjacent particles is minimized.

The packing densities will remain the same while the bed is still percolating, but once it fluidizes, the bed will expand. This can be observed visually by a rise in the bed surface. The expanding bed will exhibit a lower packing density, or a higher porosity. The gas flow at which the particles are suspended is dependent upon the terminal velocity of the particle group. In turn, this is related to the density of the particle and its size. Geldart [1973] proposed a categorization of particles based on their ability to fluidize. The boundaries between particle classes are illustrated in the chart reprinted in Figure 6.

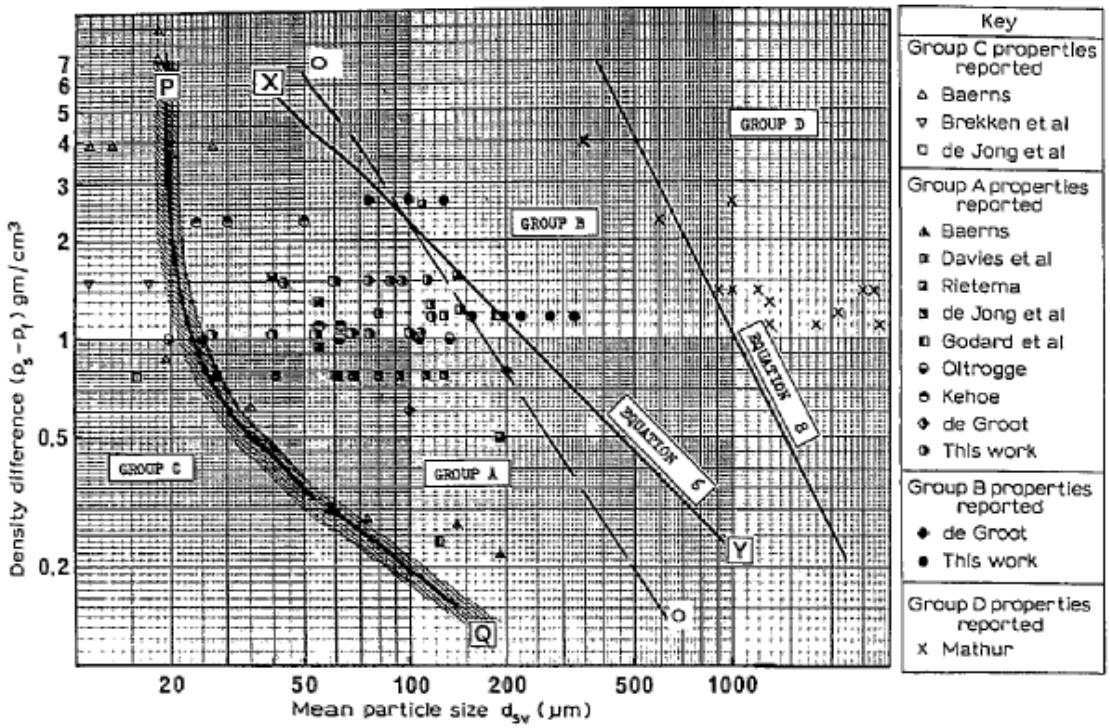

Figure 6: Geldart classification of particles [Geldart 1973]

Particles in group A have a small size and low density. These particles will expand a significant amount before the onset of bubbling. Also, the particles will circulate through the bed at fluidization when only a few bubbles are present.

Particles in group B range in diameter between 40 μm and 500 μm with a density in the range of 1.4 g/cm^3 to 4 g/cm^3. These particles do not expand much and bubbling occurs soon after the onset of fluidization.

Particles in group C are very small. They do not fluidize well and do not circulate. These particles are referred to as fines.

Particles in group D are large or very dense, or a combination of both. They fluidize at high velocities and there is little particle mixing.

Equation 2 gives a relation for minimum fluidization velocity as presented by Geldart [1973]

$$U_{mf} = \frac{8 \times 10^{-4} g d_{SV}^2 (\rho_S - \rho_f)}{\mu}$$

Equation 2

with

U_{mf} = minimum fluidization velocity

g = gravitational acceleration

d_{SV} = effective diameter of a particle

ρ_s = density of the particles

ρ_f = density of the fluid

μ = viscosity of fluidizing gas

While Geldart's classic study on particles yielded a powder classification system and a relation for the minimum fluidization velocities, another classic study by Ergun and Orning (1949) developed a relation for the pressure drop through the bed. The relation accounts for particle size and spherecity. The authors analyze a fluidized bed as a series of straight channels.

The pressure drop through a channel is defined by Equation 3.

$$\frac{dP}{dL} = \frac{32 u^* \mu}{D^2}$$

Equation 3

where,

P = pressure

L = bed height

u* = average velocity through the channel

μ = air viscosity

D = bed diameter

To this, Ergun and Orning add another term to account for kinetic energy losses due to turbulence or eddies. Equation 3 becomes Equation 4:

$$\frac{dP}{dL} = \frac{32u^{*}\mu}{D^{2}} + \frac{\rho_{f}u^{*2}}{2D^{2}}$$

Equation 4

where,

ρ_f = the density of the air.

Allowing

$$u^{*} = \frac{u}{\varepsilon} \text{ and } D = \frac{4\varepsilon}{1-\varepsilon}\frac{1}{S}$$

with,

ε = voidage

S = specific surface of the particles

and including two factors for each term, α and β, to account for the sinuous nature of the flow through a packed bed, the final form of the pressure drop per unit length through a packed bed, after integration on L is given in Equation 5.

$$\frac{\Delta P}{Lu_{m}} = \frac{(1-\varepsilon)^{2}}{\varepsilon^{3}} 2\alpha\mu S^{2} + \frac{(1-\varepsilon)}{\varepsilon^{3}}\frac{\beta}{8}(W/A)S$$

Equation 5

where,

u_m = mean velocity

W = mass flow rate

α = 1.8 - 1.9 for glass beads in gas

β = 2.8 – 3.1 for glass beads in gas

And allowing: S = 6/D based on geometry. It should be noted that values for α and β for other mediums are also presented by the authors.

Also, the authors state that for a Reynolds number of 60, both terms (the kinetic energy dissipation term and the frictional loss term) contribute equally to the pressure drop. At Re = 0.1, the friction term accounts for 99.8% of the pressure drop whereas at Re = 3000 the kinetic energy term accounts for 97% of the pressure drop. The authors define the Re as Equation 6.

$$Re = \frac{DU_{mf}\rho_{mf}}{\mu}$$

Equation 6

1.3.3 Angle of repose

A feature of particle packing relevant to the subject studied herein is the angle of repose, or the highest angle as measured from the base to the apex that grains/sand can be piled. This angle will dictate the volume and shape of particles that can sit at rest on any internal surface within a bed of particles.

The free body diagram of a section of particles shown in Figure 7 illustrates the forces on a particle at its maximum angle of repose. The particle is static and any particle added will roll down the pile. The particle size has been exaggerated for illustration.

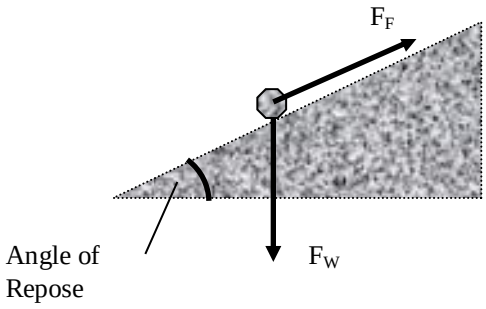

Figure 7: Free body diagram on a particle on an incline equivalent to the angle of repose

Here,

F_F = force of friction

F_W = force of weight

If the angle of repose is large, the interparticle forces are high.

Within a fluidized or percolating bed, as gas is passed through the pack of particles, the angle of repose will decrease. The gas adds a drag force acting upwards opposing the weight force. Consequently, the force of friction required to hold the particles in place is reduced, thus necessitating a lower angle of repose. The angle of repose at fluidization is 0^0 owing to the particles being weightless. This explains another feature of fluidized beds – the fluidizing medium cannot be piled up to form a 'hill' or 'mound' when fluidized.

Chapter 2 Literature review

2.1 Observances of a de-fluidized hood

Many researchers have studied the effect of the de-fluidized hood on mechanisms within a fluidized bed ranging from voids to heat exchanger tubes.

Glass and Harrison [1964] studied the flow around solid obstacles in a fluidized bed. The fluidized bed was comprised of sand and the gas velocity was held to 2-3 times that of minimum fluidization. Their findings showed three regions of flow around the object: 1) an area of air immediately below the object 2) a seemingly de-fluidized region above the sphere and 3) chains of bubbles at the sides of the obstacle. They state that the de-fluidized region would most likely disappear at higher gas flow rates.

Hager and Schrag [1976] studied the de-fluidized hood on fixed cylinders in a rectangular fluidized bed of uniform glass beads. The goal was to take photographs of the hood and determine the particle motion within the hood. This was done by using tinted beads to initially form the stagnant cap and then tracking the tinted beads over time. The bed was fluidized under bubbling conditions. The resulting hood shape and growth with time is shown in Figure 8.

As one can see, the work of Hager and Schrag indicates that the hood is similar in size to a cone with a wide and rounded top (image on the left of Figure 8). Also visible is the motion of the top layer of the hood. Over time, the particles composing the top layer erode until it is all but gone. However, as is evident from the image on the right of Figure 8, the initial cap is replaced and “overturns”, meaning that new particles replace the previous particles leading to a constant hood shape. The hood shape can be considered to be in steady state because it maintains the same shape, although the particles within the

hood are in flux. Thus, they report a secondary flow pattern within the bed causing particles to move inward toward the center of the bed. This would appear to be the mechanism by which the hood is sustained.

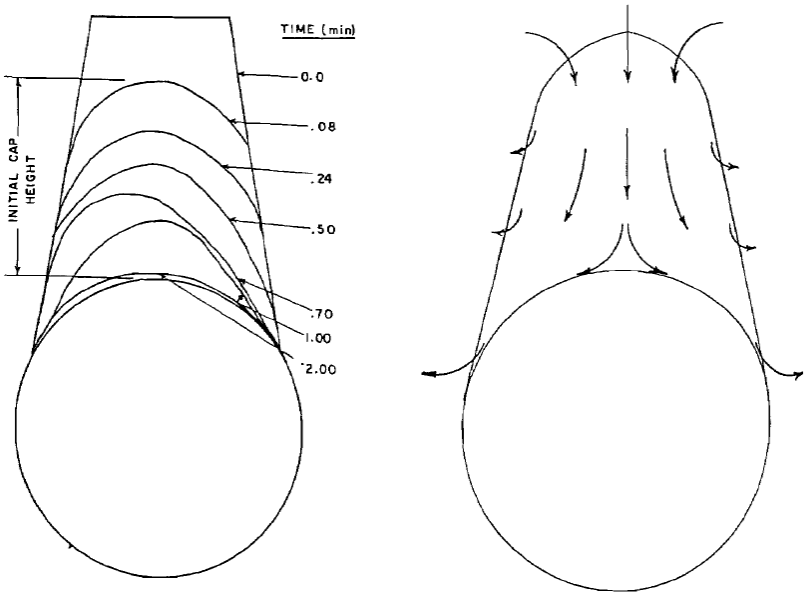

Figure 8: De-fluidized hood growth with time (left) and particle movement within (right) [Hager and Schrag 1975]

Hager and Schrag, based on visual evidence, found the ratio of the hood height to the object diameter to be 0.80. Other researchers reported values of 1 to 4, but these works did not have the benefit of tracking the hood.

Kulkarni [1987] observed the same de-fluidized region. He looked at tubes immersed in a rectangular fluidized bed of spherical glass beads with air as the fluidizing gas. His objective was to study time averaged characteristics of properties of the hood such as height and its relation to fluidizing gas velocities and particle size using long exposure still photography. His photographs confirmed the existence of the de-fluidized hood. He also confirms the gap of air, as reported by Glass and Harrison, below the

object. From his estimations of the hood height, Kulkarni proposes that the height of the hood is related to the fluidizing velocity by Equation 7.

$$\frac{H_{hood}}{d} = 0.489\left(\frac{U}{U_{mf}}\right)^{1.035}$$

Equation 7

With

H_{hood} = the hood height

d = the diameter of the immersed object

U = the gas velocity

U_{mf} = the minimum fluidization velocity.

Additionally, A.C. Rees *et al* [2005] studied the rise of spheres in fluidized beds with air as the fluidizing medium. The bed was fluidized such that it was bubbling or slugging. The authors found that the spheres rose faster when subjected to higher gas velocities. Peculiarities were observed in that objects that were expected to rise, based upon the predicted density difference between the object and the fluidizing medium, would sink instead. Furthermore, rise velocities were lower than the predicted rise velocities. These phenomena were attributed to the presence of the de-fluidized region above the spheres. Shapes and relations for the dimensions of the hood were derived assuming Stokes' flow. The authors conclude that the rise of buoyant objects in a fluidized bed can be predicted using Stokes's Law for a sphere moving in a viscous liquid.

Rees *et al* [2005] assumed the shape of the de-fluidized hood was that of a cylinder with a rounded end. Figure 9, reproduced from the original work, shows the assumed shape of the hood.

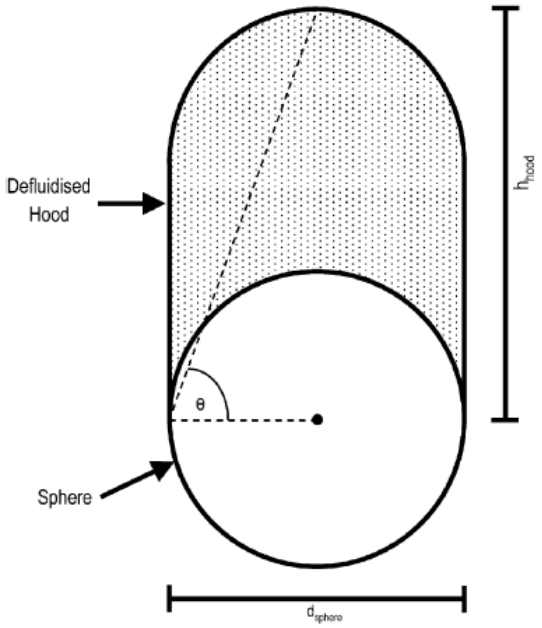

Figure 9: Shape of the de-fluidized region as modeled by Rees et al

An expression for the height of the hood is given in Equation 8.

$$H_{hood} = \frac{4\,V_{HOOD}}{\pi d_{SPHERE}^2} + \frac{D_{sphere}}{2}$$

Equation 8

where

V_{Hood} = the volume of the hood

D_{sphere} = the diameter of the sphere

The volume of the hood was not directly calculated by Rees, but rather it was inferred from other calculations, such as relations he has given for the minimum fluidization velocity, shape factors proposed by Bowen and Masliyah [1973], and wall correction factors proposed by Perry and Green [1998]. His relation for the minimum fluidization velocity is given in Equation 9.

$$U_{mf} = \frac{gVol_t(\rho_f - \rho_s)k_w}{3\Delta\pi\mu_{f(mf)}d}$$

Equation 9

Where

Vol_t = the total volume of the particle and hood

ρ_f = density of the gas

ρ_s = density of the particle

k_w = the wall correction factor

Δ = a shape correction factor for the total particle

Rees *et al* [2005] provide relations for all of the unknowns in Equation 9 except μ_f, the viscosity at minimum fluidization, and the volume of the hood, which, along with the volume of the submerged object, make up Vol_t. By taking two sets of data points, the authors can solve for these two unknowns. He finds the viscosity to be 0.66 Pa-s, which is in good agreement with the value proposed by Davidson [1977] of 1 kg/m-sec. Rees *et al* [2005] also found that the hood height can be scaled with the diameter of the immersed object, as proposed by Hager and Schrag.

Rees *et al* [2007] building upon Rees et al [2005] took previous data from Daniels 1959 of falling spheres in a fluidized bed, introduced the concept of the de-fluidized hood and found good agreement between experimental data and theory for calculating apparent viscosities of a fluidized bed.

In a study unrelated to his previous studies, Rees *et al* [2006] use magnetic resonance imaging to observe the bottom of a fluidized bed near the distributor. They observe a de-fluidized region between the jets that emerge from the holes of the perforated plate. Figure 10 diagrams the size and dimensions of two adjacent jets as well as the de-fluidized region. The authors establish a dimension from the center of the

distributor hole to the top of the de-fluidized zone and name this angle, denoted as θ_2, the 'jet initial angle'.

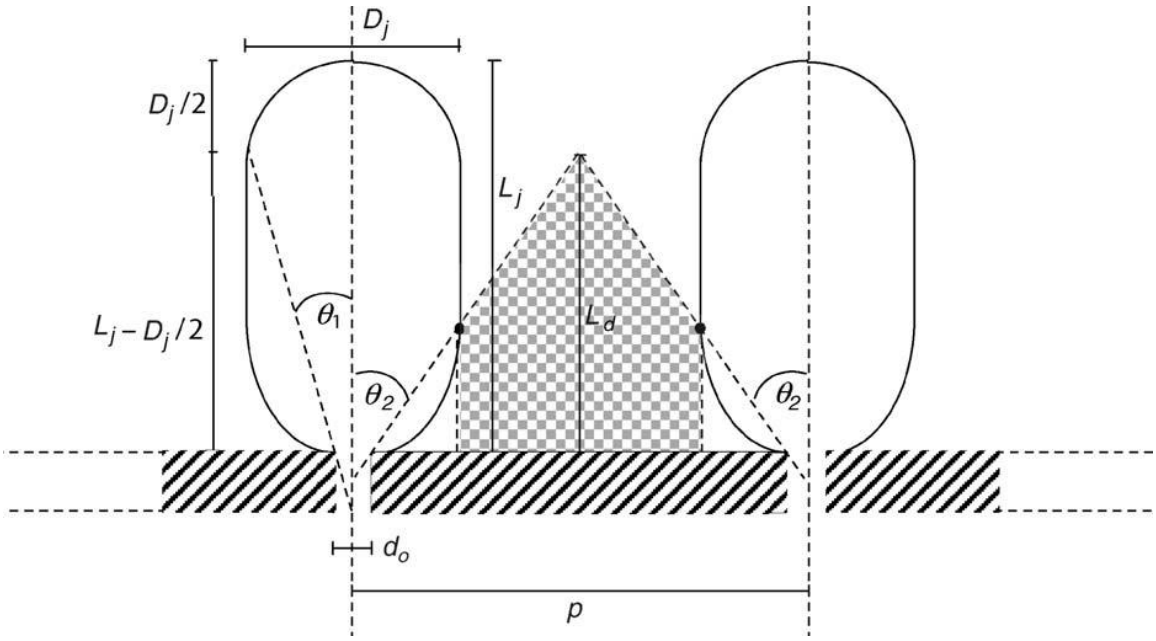

Figure 10: Diagram of the de-fluidized region between jets emerging from the distrubutor plate [Rees 2006]

The authors assert that the jet height, L_D, is a function of diameter of the holes in the distributor, the minimum fluidization velocity, the jet velocity, and the available area of the bed per hole. They determine these dependencies by charting the jet length against various variables. Using their data, the authors suggest that the height of the dead zone is approximately 0.5 – 0.9 times the pitch, with the pitch being defined as *p* in Figure 10. The authors propose setting the pitch equal to the diameter of the jet in order to eliminate the dead region between jets.

2.2 Drag in a fluidized bed

While the de-fluidized hood adds another level of complexity to the study of submerged objects in a fluidized bed, drag on the submerged object requires further study

as well. Of particular difficulty is determining the viscosity or C_D (drag coefficient) of the fluidized bed.

The work of Rees [2007] builds upon that of others who studied the viscosity of gas-solid fluidized beds. The most common treatment for beds under low Reynolds number flows has been to look at the well documented Stokes drag on a sphere, where, for Re < 1, the drag coefficient, C_D, can be estimated as shown in Equation 10.

$$C_D = \frac{24}{\mathrm{Re}}$$

Equation 10

with

$$Re = \frac{\rho_f U d_p}{\mu_f}$$

where ρ_f is the density of the fluid, U the fluid velocity, d_p the diameter of the particle and μ_f the viscosity of the fluid.

However, experimental data from studies on drag coefficients within fluidized beds shows that the above does not match well. In Crowe *et al* [1998] the data is summarized and compared to the well-known drag coefficient versus Re curve. This has been reprinted in Figure 11. The lines resembling scratches are data for C_D in fluidized beds obtained from previous researchers' work.

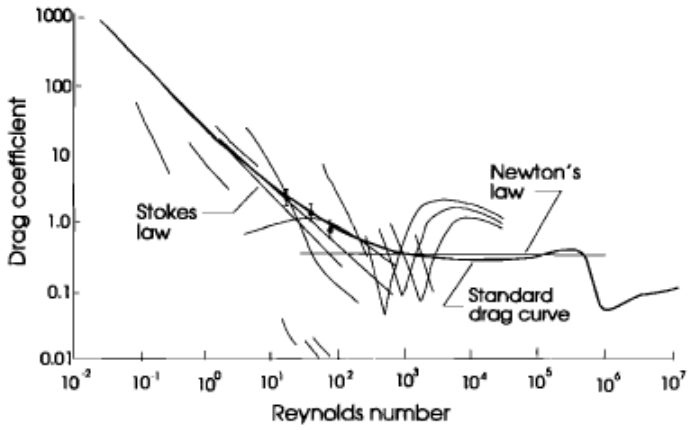

Figure 11: Comparison of Stokes Drag on a sphere to experimental results for drag on a sphere in a fluidized bed [Crowe 1998]

A correction for drag coefficient, *j*, for a particle under steady state has been given in Equation 11.

$$j = \frac{C_D \, \mathrm{Re}_r}{24}$$

Equation 11

where Re_r is the Reynolds number based on the relative velocity of the gas to the particles.

Clift and Gauvin [1970] give the following relation for *j* over the entire subcritical Re_r ($Re_r < 3x10^5$) range in Equation 12.

$$j = 1 + 0.15\mathrm{Re}_r^{\,0.687} + 0.0175\mathrm{Re}_r(1 + 4.25\times10^4\,\mathrm{Re}_r^{-1.16})^{-1}$$

Equation 12

Liu et al [1960] stirred a paddle in a fluidized bed of glass beads in an attempt to measure the apparent viscosity of a gas-solid fluidized system. His results showed that viscosity would decrease as the gas flow rate was increased. He attributes this to particle number density. With low flow rates, the paddle would have to stir through more particles than it would at higher flow rates since the bed is less fluidized. This result is

intuitive; a dense fluid is harder to stir through compared to a less dense fluid. Batchelor [1988] states the same conclusion; that the apparent viscosity will change with flow rate.

Tardos and Khan [1997] measured the forces on a slowly rotating Couette device in a fluidized bed operated at a low Re. The fluidized bed was continuously sheared by the Couette device, distinguishing this work from the bulk of the literature. The bed was operated between $0< U < U_{mf}$. The authors aimed to determine if the normal and shear stresses increase quadratically or linearly with depth.

When the bed height was increased by a factor of 1.46, the torque increased by a factor of 2. The authors conclude that the dependence on depth is linear.

2.3 Interactions of voids with submerged objects

Voids play a significant role in the development and cessation of the de-fluidized hood. Investigations into the interaction between voids and submerged objects have been carried out by many researchers.

As has been reported, voids form around solid obstructions. Building upon his work with Glass, Harrison [1971] produced images of bubbles forming around internal baffles. This has been reproduced in Figure 12. The void forms along the side of the obstruction and shoots off. The flow rate of the experiment shown is 1.5 U_{mf}.

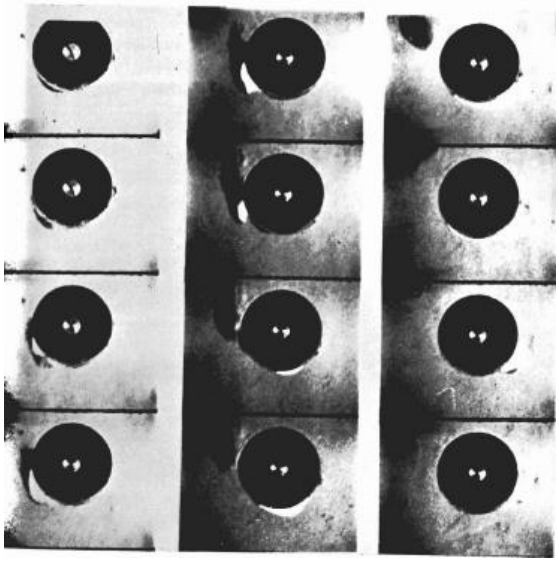

Figure 12: Evolution of a void around a submerged object [Harrison 1971]

Loew *et al* [1979] studied particle and bubble velocities in a fluidized bed of spherical Geldart D particles (of various diameters and densities) with a submerged object. The authors use a stereo-photogrammetric technique on a two dimensional bed. They, like Glass and Harrison [1967], observe a stagnant cap of particles on the upper surface of a submerged cylindrical object, as well as a bubble or air pocket on the underside and smaller bubbles along the side. As increasingly streamlined objects were used, i.e. more oval like, the stagnant cap became much smaller and particle and air velocities within the wake region became faster. Conversely, the particles above a square object were entirely stagnant.

Loew *et al* [1979] also studied the influence of voids on the motion of the particles within the cap. At velocities very near U_{mf}, the interaction between the void and the submerged object had no effect on the particles within the cap, and the particles remained still with no new particles entering the region. As the air velocity was increased, the particles within the de-fluidized region moved and were replaced with

fresh particles when a void passed. The exchange of particles induced by the bubbles took place in less than 1/60 seconds.

The authors moved the submerged object deeper into the bed and observed a larger de-fluidized region with less influence of passing voids. The authors make no mention of bed stratification and its potential impact on the hood. At the velocities studied, particles remained in the region, although at higher velocities, the particles did oscillate within the hood. Any particle leaving the region left on account of slippage off of the object surface.

For narrow oval shaped objects, the authors observed constant replacement of particles.

The authors used the images from the experiments to generate velocity and particle motion plots. They are reproduced in Figure 13 and Figure 14. The upper two numbers in Figure 13 represent the magnitude of the velocity (first number) and the direction in degrees (second number). The bottom two numbers represent the position of the particle. The hashed figures in both are bubbles while the smaller circle is the submerged object. The authors conclude that the submerged object splits the bed into two regions, one with bubbles and faster moving particles and another with no bubbles and slow moving particles.

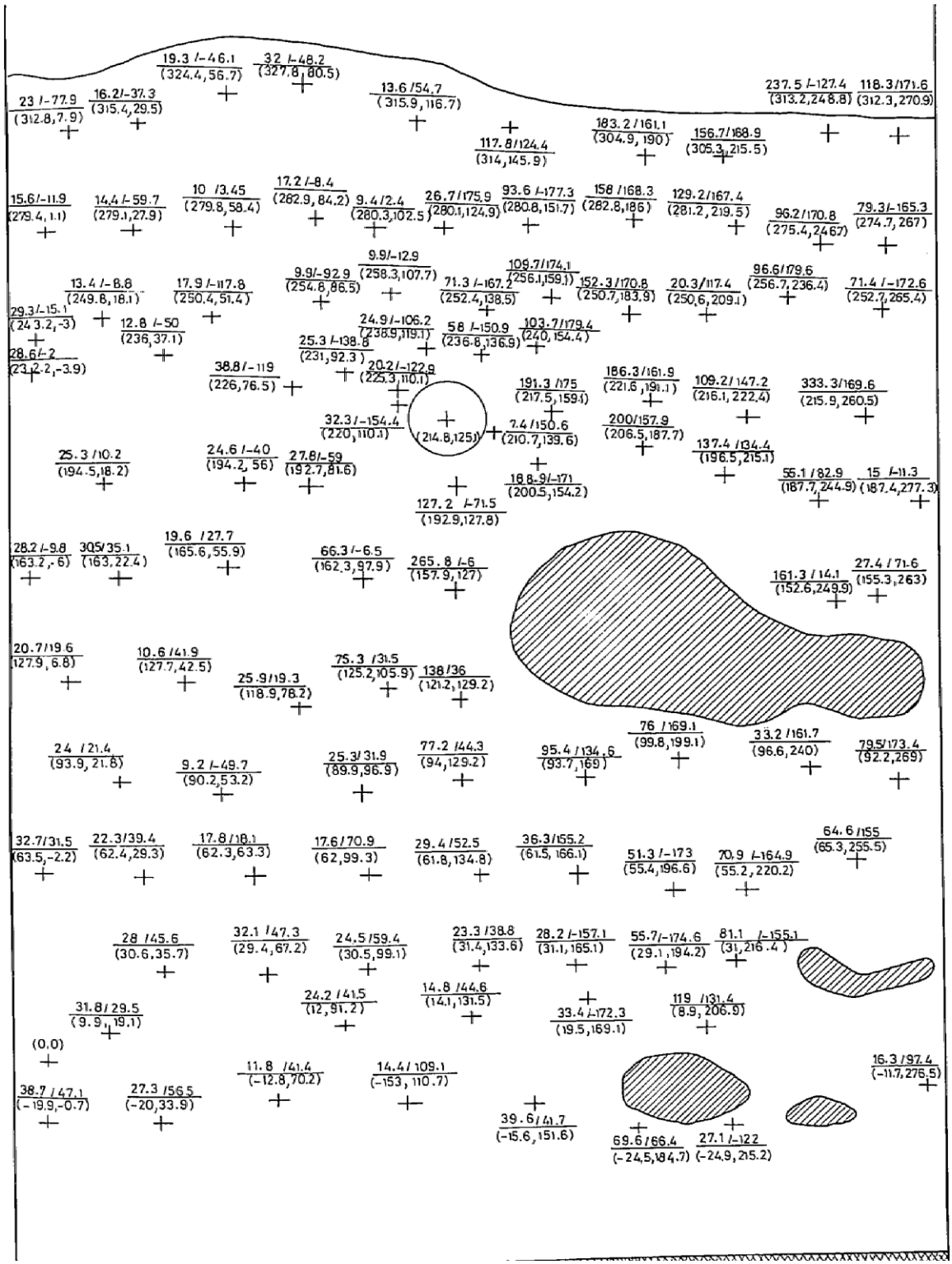

Figure 13: Particle velocities in a fluidized bed with a submerged cylinder [Loew 1978]

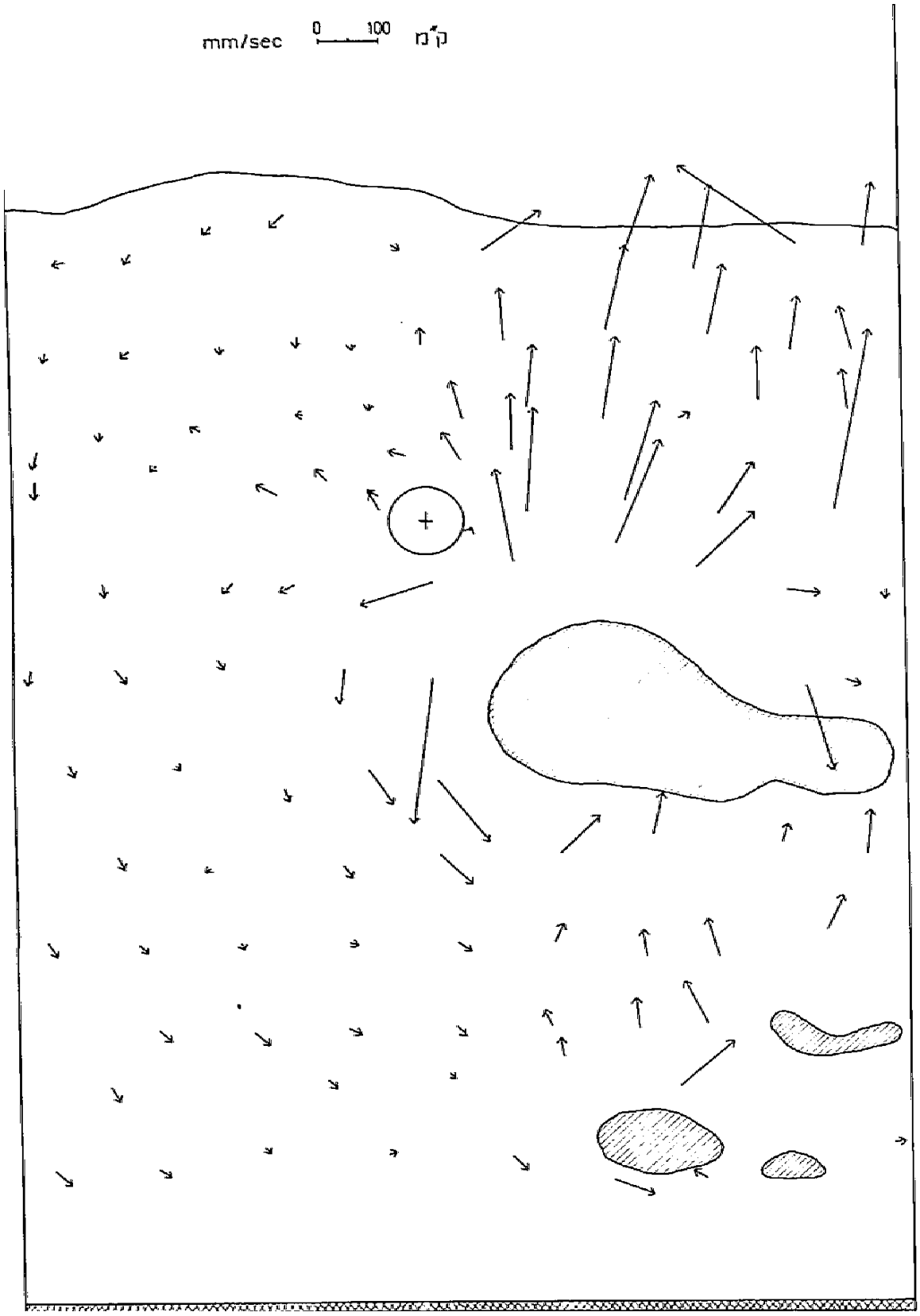

Figure 14: Particle velocity vectors in a fluidized bed with a submerged object [Loew 1978]

Visual investigations into the structure of the de-fluidized hood have improved over the years from photographic evidence (Glass and Harrison, Kulkarni, Hager and Schrag, Loew) to MRI images producing higher resolution photographs. Umekawa et al [1999] used neutron radiography techniques to visualize the movement of particles above a heat exchanger in a fluidized bed.

The authors used a 300 mm width x 700 mm height x 100 mm deep fluidized bed of 0.218 mm sand mixed with 2 mm tracer particles to visually determine particle movement around a heat exchanger tube in a fluidized bed. The heat exchanger tube was mimicked by a 40 mm aluminum rod. The bed was fluidized to 1.5 U_{mf} and the rod was located 280 mm from the bottom of the bed.

They found the void fraction peaked at 0.6 below the tube (the location of the gas pocket) and reached a minimum of 0.4 above the tube surface – in the de-fluidized zone. Figure 15 shows the creation of bubbles around the tube. Specifically, the images show the events transitioning from a steady bed around a tube to bubble growth to bubble shedding.

Figure 16 shows particle movement within the hood (particle A). As a bubble passes, it attracts particles causing them to move in a “zigzag” manner, with some moving deeper into the wake and others falling off the side of the tube. Here, the flow velocity is 1.5 U_{mf}.

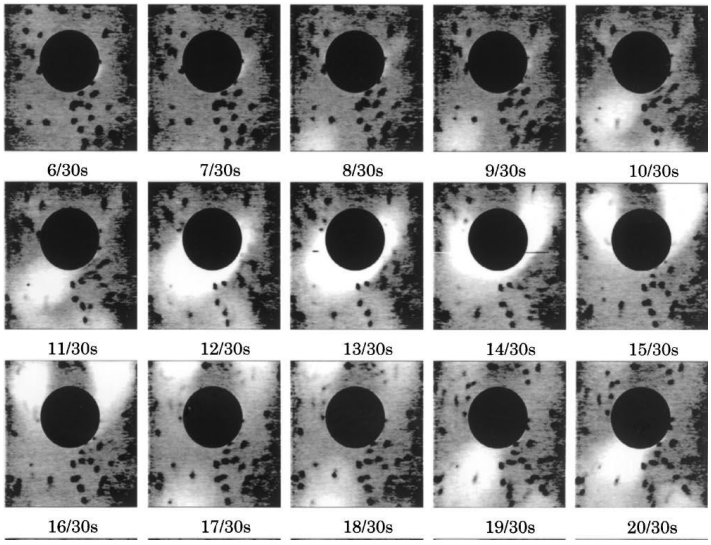

Figure 15: Flow around a sphere at 1.5 Umf [Umekawa 1999]

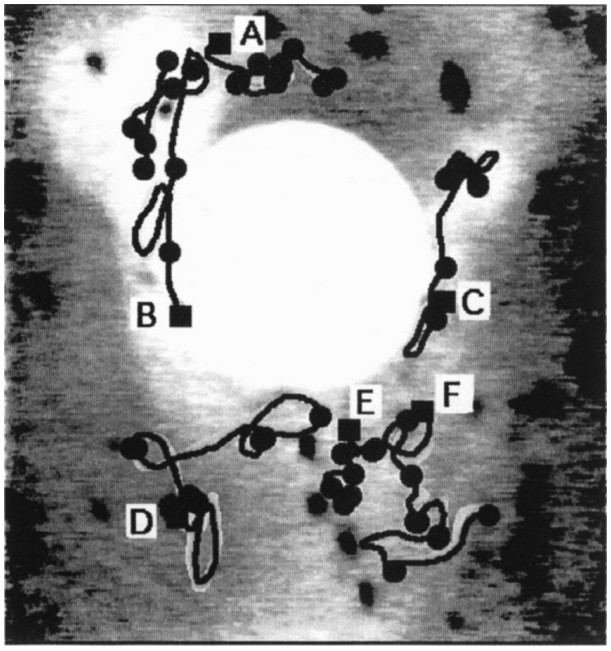

Figure 16: Particle motion above a sphere [Umekawa 1999]

Considering the work of Umekawa *et al* [1999] with the work of Rahman [2002], the role of voids on particle motion can more readily be understood. Rahman [2002] studied bubble induced particle pressures in a gas-solid fluidized bed. Particle pressure is the pressure exerted by the fluidizing medium on a surface due solely to the solid phase.

The authors' findings suggest that the strongest particle pressures are seen below and to the sides of the bubbles, peaking when the bubble erupts at the surface. As Rahman indicates, voids can cause a preferential flow of gas towards them. The gas will pull particles in its wake. The authors explain their results by hypothesizing that the bubbles create a region of de-fluidized particles by pulling gas away from the bed and into the voids. This results in de-fluidizing the bubble's surroundings thus leading to higher particle pressures as a result of particles being supported by particles rather than gas.

Further studies on voids created by submerged objects were carried out by Duursma *et al* [1994]. The authors investigate the formation and growth of voids created by obstacles in a bed operating at minimum fluidization velocity. They combine video observations with a mathematical model to determine the points around the obstacle where tube erosion can be expected to be greatest.

Using a two dimensional fluidized bed of 500 micrometer particles with a 2.54 cm circular tube operated at $1.8U_{mf}$, the authors observed void formations that were periodic and symmetric about the vertical axis. The voids detach from the tube and move out at a 45^0 angle from the obstruction. The cycle repeats every 0.8 seconds. The authors do state that visually, they observed the de-fluidized regions extending across the top third of the tube surface. Also, as the velocity is dropped closer to U_{mf}, the de-fluidized region becomes larger. The authors show the modeled vertical velocity around the tube at the time a void exists at 41^0 relative to the bottom of the tube (Figure 17). The velocity is 0 at the top of the tube. The velocity is highest at the void.

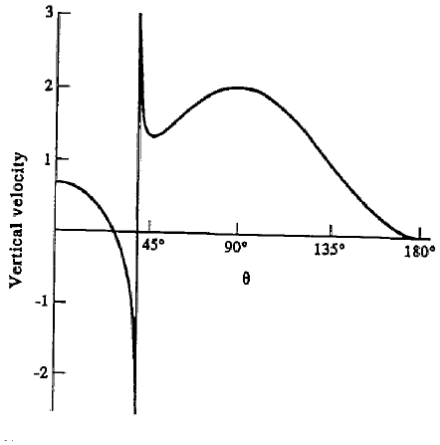

Figure 17: Velocity at submerged tube surface for a void at 41 deg [Duursma 1993]

Rafailidis et al [1992] studied experimentally and numerically the motion of a bubble in the vicinity of a horizontal tube in a fluidized bed. In their experiments, the authors observed that the tube appears to attract bubbles to it. The authors state that owing to a de-fluidized region below the tube, a pocket of air exists. This air pocket offers a path of least resistance for gas flow, and consequently, air is attracted to it. This creates voids around the tube surface.

Clift and Rafailidis [1993] studied the effect bubbling has on immersed surfaces within a fluidized bed. They were interested in learning about the stress felt by the tubes due to bubble motion. The authors assert, through literature review, that particle pressure on surfaces is caused by a disturbance of the particle phase arising from bubbling motion.

The authors find that the pressure drop across the tube is much less than it would be across the bed. The pressure difference around a 50 mm tube was 150 Pa as opposed to 700 – 800 Pa over a 50 mm section of the bed. Furthermore, the pressure at the tube surface was 1 – 2 kPa below the bed pressure at the same height. Thus, the authors claim, the flow is preferentially attracted to the tube rather than the surrounding bed. This

additional air leads to void formations. In an incipiently fluidized bed, voids form at the 4 o'clock to 8 o'clock positions. The surfaces attract bubbles as demonstrated by referenced experiments. Furthermore, as a bubble leaves the vicinity of the surface, it will draw gas away from the surface.

2.4 Bed Properties in the vicinity of submerged objects

As the submerged objects change the flow fields within the bed, one would expect the bed properties in the vicinity of the tube to change as well. Several researchers have studied the voidage – ratio of gas to particles in the bed and not to be confused with "voids" which are packets of excess gas - and heat and mass transfer coefficients around submerged objects.

2.4.1 Submerged object effect on voidage

Fakhimi and Harrison [1980] use a capacitance method to study voidage fractions near a single immersed tube placed horizontally in a 2D fluidized bed.

The apparatus was 1.2 m high by 0.38 m wide. Two tubes were used: a 28 mm diameter tube and a 51 mm diameter tube. Experiments were carried out with the tube in isolation, with the 28 mm tube in three square pitch arrays and with the 28 mm tube in a triangular array. The fluidizing medium was six different types of sand varying primarily in diameter. Three types were used for the 28 mm tube and three for the 51 mm tube. The capacitance method creates varying dielectric constants between adjacent plates with the constant being dependent on the amount of sand between the plates. These plates surround the tubes and allow for local voidage fractions near the tube to be determined. The flow rate chosen was between 1 to 5 U_{mf}.

The results show a much lower voidage fraction near the top of the tubes. This indicates a more packed region at the top of the tube as compared to the rest of the tube. From $3\pi/4$ to π (with zero being the bottom of the tube), the voidage stays constant over the flow rates tested. The authors state that the de-fluidized hood exists in this region, but that its significance diminishes with increasing flow rate.

Garim *et al* 1999 studied the mass transfer coefficients around a horizontal cylinder immersed in a fluidized bed. They studied the Sherwood number (Sh), which is a measure of the mass transfer due to convection compared to diffusion, at different angular positions and flow rates around the tube. They found the minimum and maximum Sh at the top and bottom of the tube respectively.

Garim *et al* 1999 experimental apparatus consisted of a 0.4 m high by 0.20 wide fluidized bed with a 0.0356 m dia by 0.0508 m long cylinder placed 0.075 m above the distributor. The fluidizing medium was glass beads. The cylinder was coated in naphthalene and the initial surface profile was recorded. The experiment was run with the cylinder in the fluidized bed. The naphthalene would evaporate off of the surface of the cylinder and the evaporation rate was based on the flow velocity at that point along the cylinder. The tube was removed and the surface profile was re-measured.

He defines the Sh as Equation 13.

$$Sh = \frac{k_p D_{tube}}{D_{diff}}$$

Equation 13

Where

k_p = mass transfer coefficient

D_{tube} = tube diameter

D_{diff} = diffusion coefficient

The results are shown in Figure 18. He finds the highest Sh to be between 0 (bottom of the cylinder) and 30 deg. The highest is 175 at 0 deg. Between 30 and 120 deg, the Sh decreases sharply from 150 to 50. The Sh decreases from 50 to 10 from 120^0 to 180^0, which corresponds with the de-fluidized region.

Transition between fluidized and de-fluidized seems to be around 112.5 deg and 135 deg.

An increase in gas velocity serves to increase the mass transfer coefficient.

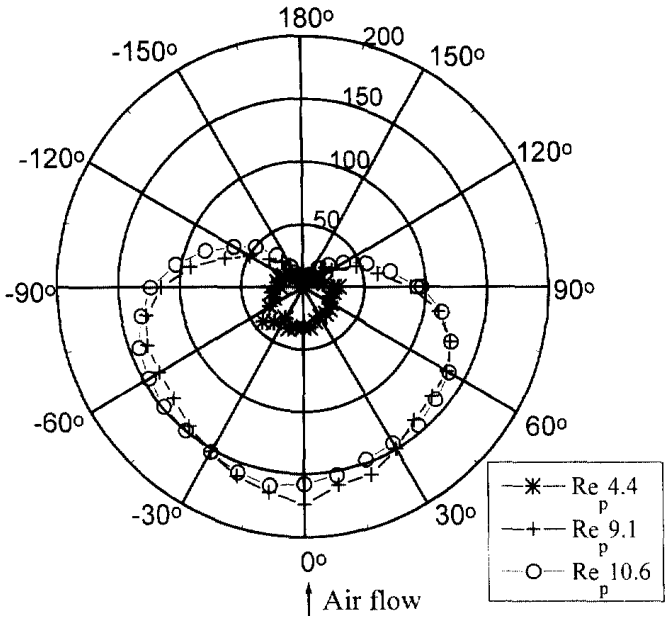

Figure 18: Sh numbers around a submerged sphere in a fluidized bed [Garim 1999]

2.4.2 Submerged object effect on heat transfer coefficient

The heat transfer coefficient in a fluidized bed has been well studied. Of particular interest are the heat transfer characteristics in the de-fluidized region.

Peeler and Whitehead [1982] studied the effect bubbles motion has on the heat transfer coefficient in the vicinity of a submerged tube. Of note, the authors distinguish

themselves from previous works by using a three-dimensional bed rather than a two-dimensional bed. The authors state that an important consequence of extending the study to three dimensions is the decreased size of the stagnant cap found above heat transfer surfaces in three dimensional beds. The authors also use a bed that was 1.22 m square, making it similar in size to that used in industry. This allows for bubbles to grow to the size commonly seen in industrial applications.

The authors track the motion of particles as a bubble passes the tube. The bed is fluidized to $3U_{mf}$. Before the bubble approaches, the particles in the cap 'vibrate', but do not move. As the bubble approaches, the particles in the cap remain in contact with the tube, unlike in any other region around the tube where they are freely mixing. However, the particles in the cap do slide down the side of the tube, and are swept into the rest of the bed. As the bubble engulfs the tube, the particles in the de-fluidized region are pulled away leaving the tube exposed. Integrated over the entire bubble period, the top of the tube experiences greater particle contact than the bottom of the tube. This correlates to previous work cited by the author showing that the lowest heat transfer coefficients are found at the top of tubes due to the stagnant cap of particles. As the air velocity increases, the stagnant cap is replenished more frequently and the overall heat transfer coefficient gets larger.

Kurosaki *et al* [1988] conducted a similar investigation on the heat transfer characteristics around immersed tubes in a gas solid fluidized bed. The authors used Geldart B particles and studied the change in heat transfer and flow characteristics as the flow was brought from a sub minimum fluidization regime to a turbulent regime. The authors found that the particles in the top region remain still until the gas velocity is very

large (relative to the gas velocity required to see particle motion elsewhere) and it is the last region to exhibit particle motion as the gas flow rate is increased. At near minimum fluidization velocities, the particles in the top region remain still. At bubbling velocities, the authors observed particles sliding from the still region at the top down the sides of the tube. Sliding continued through the slugging regime and when the flow was increased further such that the bed was turbulent, the authors found the top region to be fully mixed and fluidized.

Regarding the heat transfer coefficient, the authors found the top region to exhibit some of the lowest Nusselt numbers at the fluidized and bubbling stages compared to other positions along the tube during. The Nusselt number provides a measure of the increase in overall heat transfer coefficient due to an increase in air velocity. The authors define the Nusselt number as Equation 14.

$$Nu = \frac{hD_{cyl}}{\lambda}$$

Equation 14

Where

h = the heat transfer coefficient

D_{cyl} = the diameter of the cylinder

λ = the thermal conductivity

As the bed was transitioned through slugging and into turbulent, the top of the tube demonstrated the largest Nusselt number of any position along the tube. The authors attribute this to significant particle mixing in the top region at higher air velocities.

Over the course of two papers, Molerus *et al* [1995] studied the relationship between heat transfer from an immersed tube and the particle velocity. In the first paper, the authors state that the main mode of heat transfer in a fluidized bed is particle

convection. Their findings are the result of observing an increase in particle exchange frequency near a heat transfer surface and in increase in the heat transfer from the immersed tube as the air flow velocity is increased. Thus, the authors conclude, the particles are the heat carriers. In the second part, the authors find that the heat transfer coefficient increases as the velocity increases.

Kim *et al* [2002] also studied the heat transfer characteristics around an immersed tube with bubbles. The authors used a tube bundle rather than a single tube for their study, but concentrated on the particle motion, velocities and heat transfer at a tube situated in the middle of the bundle. The findings are summarized in Figure 19.

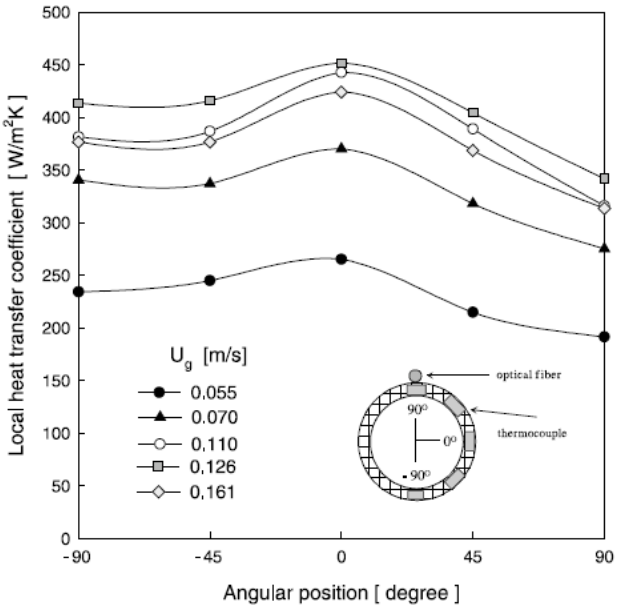

Figure 19: Heat transfer coefficient around a tube in a bundle [Kim et al 2005]

The heat transfer coefficient was found to be the lowest in the region of the stagnant cap at the top of the tube. Although not cited by the authors, Garim [1999] found the mass transfer coefficient to be smallest in this region as well. The authors also note that the temperature at the top of the tube varies less than it does at other locations around

the tube. The authors attribute this to the lack of bubbles around the internal tubes in a tube bundle. The bubbles induce particle motion and since heat transfer is carried through particle motion, these regions will see less heat exchange. The authors show that the bubble frequency is lowest at the top of the tube.

The authors continue by developing a relationship for the average heat transfer coefficient around a submerged tube. Typically, a 'packet model' is used to estimate the heat transfer coefficient. This model assumes that the heat transfer from a tube is dictated by the residence time of a packet of particles. The relation for heat transfer coefficient is dependent upon the fraction of the bed occupied by bubbles and the particle contact time.

The authors state that the packet model cannot be used to model the heat transfer coefficient at the top of the tube because the region experiences less bubble contact than the rest of the bed. The packet model assumes a bubble frequency for the whole bed. The authors assert that the heat transfer coefficient at the top of the tube is only dependent on the residence time of the particles.

By collecting experimental data and correlated their data with that of other researchers, the authors present a correlation for the Nusselt (Nu) at the top surface of a heat exchanger tube in a fluidized bed. The correlation is given in Equation 15.

$$Nu_{top} = 47.56Re^{0.43}Pr^{0.33}\left(\frac{D}{d_p}\right)^{-0.74}\left(\frac{C_{ps}}{C_{pg}}\right)^{-1.69}$$

Equation 15

Where Re is the Reynolds number, Pr the Prandtl number, D the tube diameter, dp the particle diameter, Cps the specific heat of the particles and Cpg the specific heat of the gas. His correlation is correct to within ±20% of the reported data.

2.5 Forces on submerged objects within a fluidized bed

The de-fluidized hood exerts an added force on a submerged object. For comparison and in order to determine the overall force balance on a submerged object, it is necessary to review some of the previous relevant work on forces on submerged objects in a fluidized bed.

Nguyen and Grace [1978] studied forces on horizontal tubes as bubbles passed in a 2D fluidized bed using pressure measurements. By integrating the pressure around the tube, a graph of force versus time on the tube is obtained. The form is a sine wave with the greatest upward force corresponding to the arrival of a bubble and the greatest downward force corresponding to the wake of a bubble. The authors cite the need to understand dynamic loads on immersed objects in a fluidized bed as well as the need to understand floating within a fluidized bed as the motivation for their work. The paper studies objects floating on the bed surface, as well as the transient forces on a horizontal tube. The conclusions from this study is of particular interest to the present work

The experimental set-up for testing floating objects consisted of a fluidized bed (45.7 cm in dia and 99 cm tall) with 291 micrometer sand (Geldart B) as the fluidizing medium. U_{mf} was 7 cm/sec and experiments were carried out at 1.08, 1.24 and 1.47 times U_{mf}. Spheres, cylinders and rectangular parallelepipeds were used as the immersed objects. At higher fluidized velocities, particles thrown on top of the objects were quickly swept away, thus making it difficult to take readings at these settings.

The authors state that when the immersed object is much larger than the fluidizing medium, the drag on the object is negligible compared to the buoyant force. Thus Archimedes principle can be used to determine the apparent density of objects. By doing

so, the authors determine that the immersed volume is linearly related to the immersed object mass. The authors conclude that when calculating the buoyancy on a floating object, the density of the bed at minimum fluidization can be used. However, the authors state that this assumption may not be valid if the object is completely immersed within the bed.

In testing the buoyancy force of a floating object, the authors characterize the experiments into four categories: 1) object density much less than bed density; 2) object density less than bed density; 3) object and bed density same; and 4) object much more dense than the bed. For scenario 1, objects will at all times stay at the surface. For scenario 2, objects will spend the majority of their time at the bed surface, but will intermittently be completely submerged as particles are splashed on top of it. Bubbles remove the particles, thus allowing the objects to rise again. For scenario 3, the object could circulate throughout the bed, but never rest at the surface or sink to the bottom. For scenario 4, the object will sink to the bottom.

Grace and Hosney [1985] investigated the forces on horizontal tubes in a fluidized bed of spherical and non-spherical objects as bubbles passed by the tubes. The tubes were attached to the bed by two strain gauges at either end. The researchers were interested in discerning the effects of superficial gas velocity, static bed height, particle diameter, particle density, tube diameter and tube shape on the vertical forces on tubes. The conclusions reached are that the buoyant force at times when bubbles are not present is very nearly approximated by Archimedes Principle, but corrected by Equation 16:

$$F_B = 0.7\rho_s(1-\varepsilon_{mf})gV$$

Equation 16

Where,

F_B = the buoyant force

ρ_{db} = the density of the dead bed

ε_{mf} = the voidage at the minimum fluidization velocity

V = the displaced volume.

Grace and Hosney attribute the correction factor of 0.7 "to the tendency for a 'stagnant cap' of particles to form on top of an immersed tube". This cap would weigh the tube down, thus counteracting the upward loading due to buoyancy on the tube. The coefficient of 0.7 was developed experimentally.

Additional studies on the apparent buoyancy of large spheres at several locations in fluidized beds were carried out by Oshitani *et al* [2000]. The fluidizing medium was spherical glass beads. Their goal was to measure local particle flow velocities by measuring the buoyancy of a submerged object at different locations. Their experimental set-up was very similar to that of the present work, as will be explained later. However, they did not consider the effect of the de-fluidized region above the sphere. Oshitani *et al* used Equation 17 to determine the buoyancy:

$$Apparent\ Buoyant\ Force = \frac{weight\ of\ the\ sphere\ in\ atmosphere - weight\ of\ the\ sphere\ in\ bed}{weight\ of\ sphere\ in\ atmosphere}$$

Equation 17

Their results showed variation in apparent buoyancy and thus flow velocity as particle size, superficial gas velocity and bed height are increased. Therefore, it can be assumed that the apparent buoyancy is a function of the studied parameters.

Rios *et al* [1986] studied the motion of a large light object in a fluidized bed of small heavy particles in an attempt to better understand segregation patterns and circulation within a fluidized bed. As stated by Nguyen and Grace [1978], objects less

dense should float in a fluidized bed while more dense objects should sink. Rios *et al* note that flat objects sink to the bottom regardless of density.

The authors tested small spheres and large spheres in a fluidized bed. Without mentioning the de-fluidized regions above the large spheres, the authors note that the smaller large objects move about more freely than the bigger large objects (both had the same density) in a bed of Geldart B particles. The authors state that large light object motion in a fluidized bed is controlled by a force balance between gravity, buoyancy and drag as well as mixing caused by bubbles and their influence on the surrounding medium. Slugging velocity represents a boundary, above which bubble motion plays a large role in object motion and below which a hydrodynamic force balance takes over.

2.6 Stick-slip phenomenon within packed beds

Making force measurements within packed, percolating or fluidizing regions is made difficult by the complexity of the shear forces within granular media. The following reviews some of these complexities.

Albert *et al* [2001] studied the drag forces on an object dragged through a granular medium. The authors note "jammed" states give the data a "stick – slip" characteristic. These jammed states are dependent on the direction and magnitude of the applied loads and are a result of directional force chains that do not propagate uniformly through the media. As an object imposes a force on the granular media, it remains still until the force exceeds that of the jammed state. Once it exceeds this force, it moves, reorganizing the grains around it. This creates "chatter" in the data, with the peaks corresponding to the strengths of the jammed states. The authors state that the force of the

jammed state dominates the drag force. The size of the chamber used to hold the grains can affect the strength of the jammed state.

The authors used a 150 mm vessel filled with glass beads of varying density as their test apparatus. Within the vessel is a rod attached to a spring. A force cell is attached to the spring. A comb is located opposite the rod. The vessel rotates and the force on the spring is measured. The spring allows the force to slowly build up and allows the elastic response of the rod to be controlled by adjusting the spring constant k. The comb reorganizes the granular medium after the rod passes through. The sphere diameter is varied from 0.3 – 5 mm, the vessel diameter is varied from 8 to 24 mm, depth of insertion from 20 – 190 mm, and the speed from 0.04 – 1.4 mm/sec. The grains are not fluidized.

The authors observe regimes of stick-slip fluctuations which are represented in Figure 20:

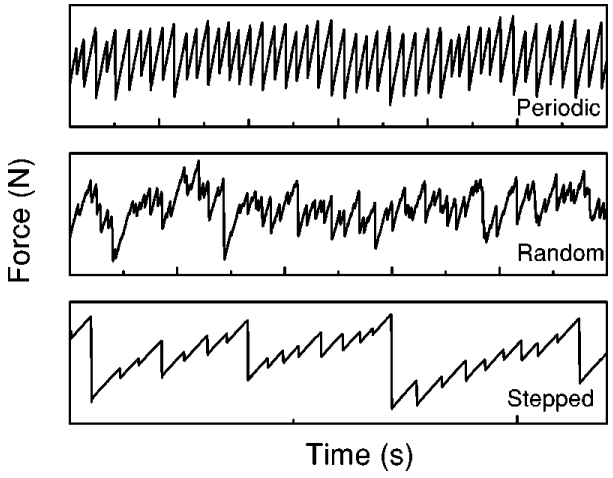

Figure 20: Characteristics of stick-slip motions from [Albert et al 2001]

The difference between the three graphs is determined by grain size, rod depth, and vessel diameter. Periodic behavior is observed for smaller grain sizes and shallower rod immersion depths. The random behavior is observed for middle range grain

diameters. The authors did not further investigate the random behavior. The stepped behavior is observed for deep immersion depths and shows small saw tooth fluctuations forming larger saw tooth swings. Vessel diameter will also determine the transition between these regimes.

Figure 21 shows the transition from periodic to stepped regimes as a function of immersion depth. Figure 22 shows the average force required to move the rod versus depth. The dip in the data corresponds to the transition from periodic to stepped.

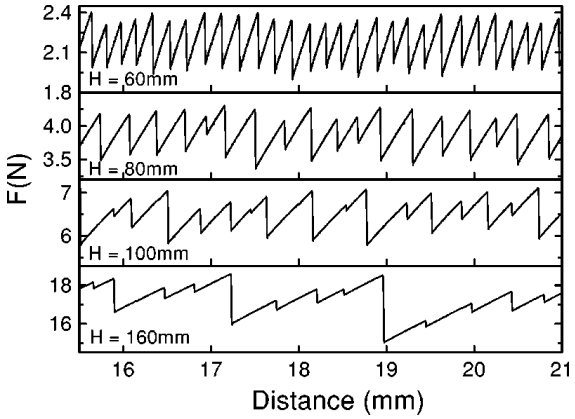

Figure 21: Transition from periodic to stepped behavior with submersion depth [Albert et al 2001]

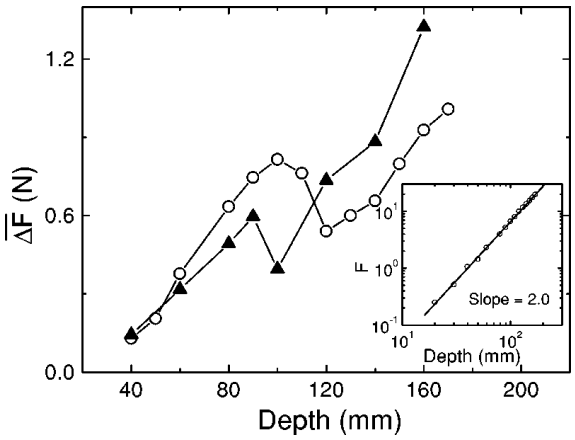

Figure 22: Average force required to move rod with increased submersion depth measured from bed surface [Albert et al 2001]

The graphs show that with everything else held constant, the behavior of the force changes with rod depth from periodic to stepped. The authors also show that in the stepped regime, the force peaks are followed by even greater peaks showing a dependence of the jammed state on the previous jammed event. For shallow depths, there is no dependence.

To explain the transition, the authors hypothesize that the force chains propagate as shown in Figure 23:

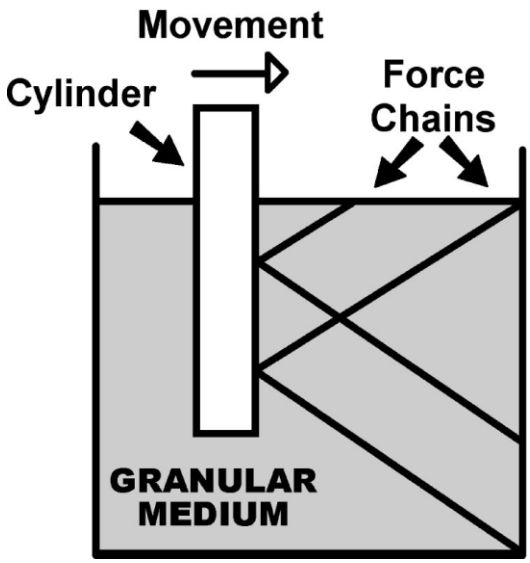

Figure 23: Explanation of path of travel for force chains [Albert 2001]

For shallow H, the free surface can adjust to accommodate for the force chains thus breaking them. For deeper H, the force chains hit the cylinder walls, which are rigid. This causes the force chains to grow more than they would at shallow depths. Since the force chains also grow in magnitude due to normal forces from the wall, more small slips will occur. The authors suggest that wall effects are very important in determining the characteristics of the slip stick behavior.

Anjaneyulu and Khakhar [1994] argue that a fluidized bed behaves like a Bingham fluid rather than a Newtonian fluid. A Bingham fluid will only shear after a certain stress is applied, as opposed to a Newtonian fluid which will shear the instant a stress is applied. Once in shear, the Bingham fluid will shear linearly with strain up until an elastic limit. The authors use a circular measuring device to determine the viscosity and yield stress of a fluidized bed operating at near minimum fluidization conditions.

The authors note the pitfall of the traditional method of measuring viscosity in fluidized bed – using an impeller – stating that these methods disturb void formation and growth and do not account for the de-fluidized region found above the obstacles. Another inherent assumption in this method as well as other methods is that the bed behaves as a Newtonian fluid.

For their experiments, the authors used a fluidized bed of glass beads operating at minimum fluidization such that the voidage was similar to that of a bubbling bed but the bed was not bubbling. A roughened cylinder was placed in the fluidized bed and rotated. The torque on the cylinder was measured by a viscometer. The authors varied bead size, cylinder rotation speed, depth of immersion, flow rate (without deviating too far from minimum fluidization) and cylinder radius.

Theoretically, the authors use the Bingham model for plastics when developing their set of equations relating the speed of the cylinder to the wall shear stress. The equations are fitted to the experimental data. The authors see a behavior between the stress and the shear in the fluidized bed similar to that of a Bingham fluid. There is a shear layer around the rotating cylinder, beyond which shearing does not occur and the bed remains unaffected. This critical radius is the point at which the shear stress equals

the yield stress. The authors find good agreement between their equation for the location of the critical radius of thickness and the data. This provides some support to the claim that a fluidized bed behaves like a Bingham plastic.

The authors also show that the viscosity decreases up until minimum fluidization at which point it flattens. The yield stress on the other hand decreases monotonically. The authors argue that this makes physical sense. In the shear layer near the cylinder, any excess velocity beyond minimum fluidization would relieve itself as bubbles. Since the solids fraction is nearly constant in this region, the viscosity would remain the same. The yield stress would continually decrease because it is in effect a measure of the force of the particles on one another. With increasing gas velocity, this force decreases and thus the yield stress decreases.

2.7 Flow field behind objects at low Reynolds numbers

The present study will examine the effects of placing a disk and a sphere in a fluidized bed. Since an air flow will be passing these structures, it is relevant to review the flow around such objects in a single phase fluid at a low Reynolds number.

2.7.1 Flow field behind a sphere at low Reynolds numbers

The momentum deficit behind a sphere in a flow of a fluid has been well studied. Batchelor [2000] and White [1974] have provided an analysis of the special case of viscous flow around a submerged sphere. Due to the drag imparted on the sphere, there is a momentum deficit behind it. Referred to as a wake, its nature depends on the Reynolds number of the flow. At very low Reynold's numbers ($Re < 1$), the flow sticks to the

object and there is no wake. Figure 24 shows flow past a sphere at Re = 0.25. As can be seen, the flow remains in contact with the sphere and there is fore and aft symmetry.

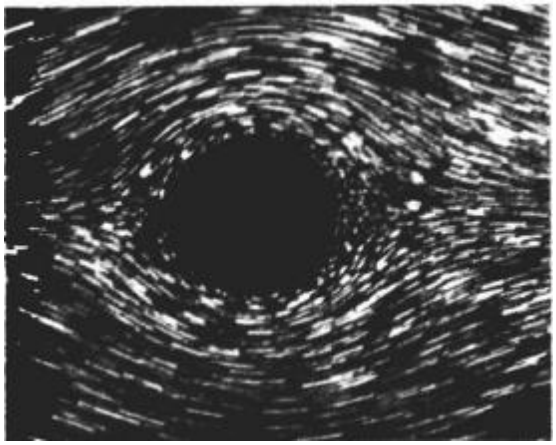

Figure 24: Wake behind a sphere at Re = 0.25 [Batchelor 2000]

The flow field in Figure 24 has been solved by many, including White (1974). For a flow field with Re<<1, commonly referred to as creeping flow, the solution is in spherical coordinates in Equation 18.

$$u_r = U\cos\theta\left(1+\frac{a^3}{2r^3}-\frac{3a}{2r}\right)$$

and

$$u_\theta = U\sin\theta\left(-1+\frac{a^3}{4r^3}+\frac{3a}{4r}\right)$$

Equation 18

Where,

u_r = velocity in radial direction

u_θ = velocity in tangential direction

θ = theta direction of interest with 0 being parallel to the free stream flow

U = free stream velocity

a = object radius

r = location of interest

Some key results from this solution are that it is independent of material properties, such as viscosity and density. Furthermore, the solution is symmetric, implying a retardation of the flow before and after the object. Also, as far downstream as 10a the velocity has only recovered 90% of its free stream value.

Figure 25 shows the flow past a sphere at Re = 9.15. As the Re increases past Re ~ 1, it separates from the body due to the inability of the flow to overcome the adverse pressure gradient within the boundary layer. This separation can be seen in Figure 25 towards the rear of the object. The separation becomes more evident as the Re increases. Once separation occurs, recirculation patterns caused by the vorticity in the wake can be seen behind the object where the flow circles back towards the submerged object. This can be seen in Figure 26.

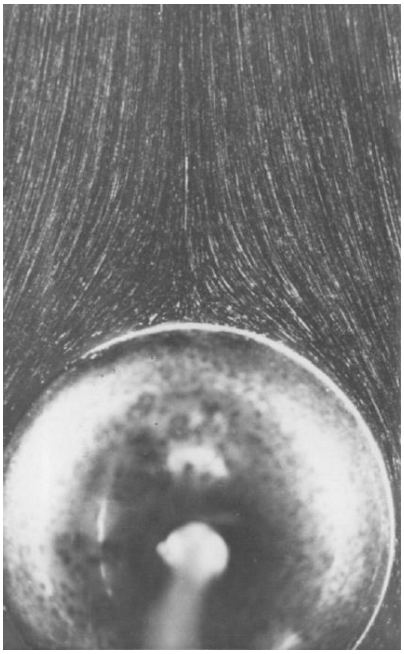

Figure 25: Flow past a sphere at Re = 9.15. [Taneda 1979]

Figure 26:Flow past a sphere at Re = 37.7. [Taneda 1979]

2.7.2 Flow field behind a disk at low Reynolds numbers

Due to the complexity of the geometry and the subsequent increased difficulty in the flow turning around the object, the structure of the wake behind a disk is difficult to calculate by hand and has been solved numerically.

Myagi and Kamei [1983] studied the vortex behind a disk at small Reynolds numbers. The authors consider the steady viscous incompressible fluid flow past a circular disk positioned perpendicular to the flow. The authors find that at a small, but finite, Reynolds numbers, vortices appear behind the disk and the flow separates from the disk. Using the relations developed in the study, the authors predict that the separation angle of the flow will be a function of the Reynolds number (Re) and occur at 41.5^0 x Re. For the case of Re = 0.3, the authors produce the streamlines around a disk as shown in Figure 27.

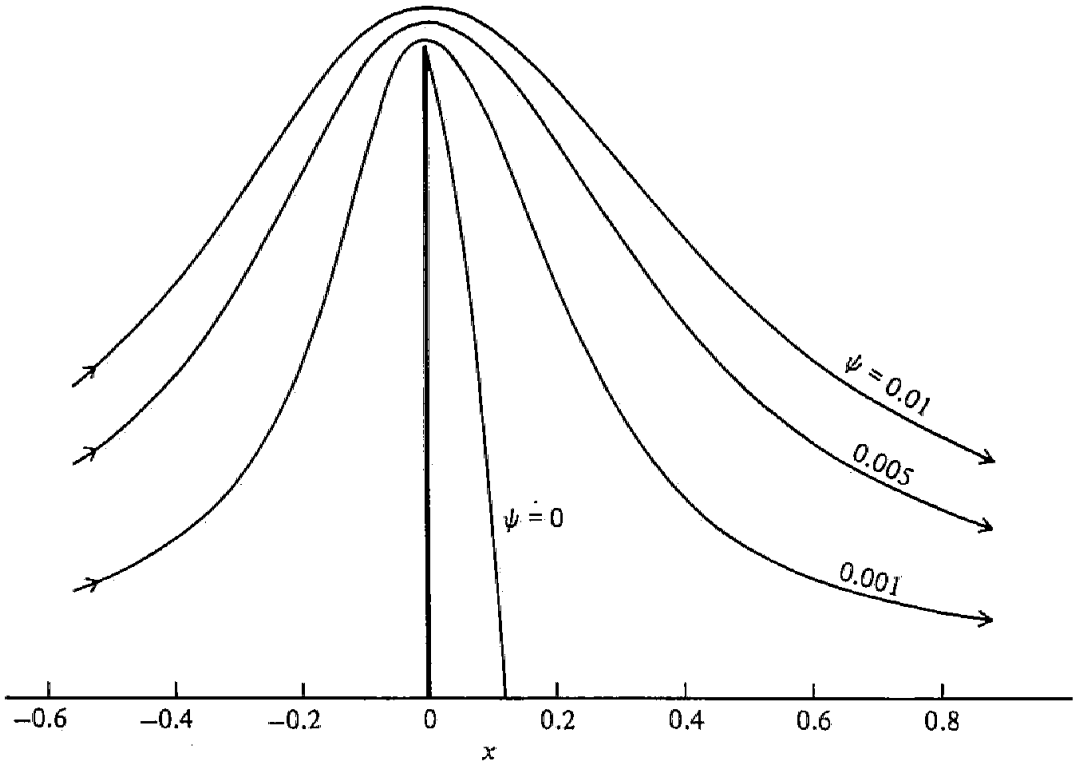

Figure 27: Flow around a disk at Re = 0.3 from Miyagi and Kamei (1983)

In another study on the flow over a thin disk, Shenoy and Kleinstreuer [2008] numerically studied the phenomenon at a slightly higher Reynolds number. The disk was considered thin and had a thickness/diameter ratio of 10. The flow was perpendicular to the disk and held at a range of Re from 10 – 300.

For the lower ranges of Re studied (~10) the authors find the flow to be steady and axisymmetric. The flow separates from the leading edge and forms vortices behind the disk. Figure 28, taken from the work, shows the flow around a thin disk at Re = 10.

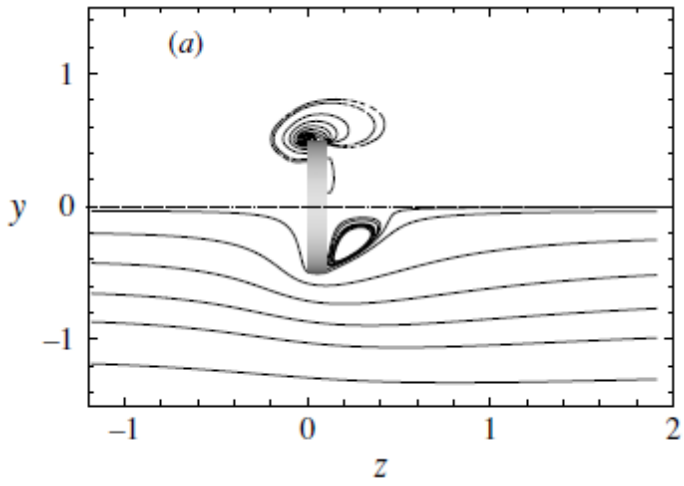

Figure 28: Flow around a disk at Re = 10

Furthermore, the length of the vortex region shown in Figure 28 becomes longer as the Reynolds number increases. The relation between the length of the vortex region and the Re is shown in Figure 29.

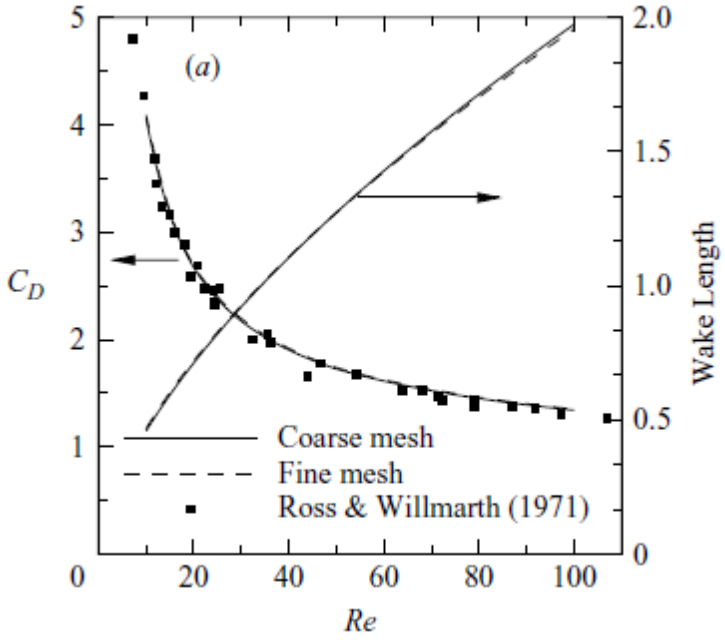

Figure 29: Length of wake (in disk diameters) versus Re taken from Shenoy and Kleinstreuer (2008)

Chapter 3: Experimental Set-Up

Five experiments were conducted to determine the structure of the de-fluidized hood. They were aimed at:

- Determining the forces on a submerged object within a fluidized bed while varying the size and shape of the object, fluidizing medium and location of the object within the bed to determine the effect of these parameters on the force
- Determining the shear within the de-fluidized hood due to the particles
- Determining the drag within the de-fluidized hood due to the air flow to determine the influence of the hood on a neighboring structure
- Determining the radial penetration of the de-fluidized hood at various submerged object depths
- Determining the normal force exerted by the de-fluidized hood at various submerged object depths

3.1 The Fluidized bed

The fluidized bed, an FB-08 Fluidized Calibration Bath provided by the Techne Corporation, is made of stainless steel and has an inside diameter of 23 cm and height of 43.2 cm. The bed was oriented vertically and is open to the atmosphere at the top. Air was fed into a plenum chamber through a 0.3175 cm inlet. The inlet was located at the wall and air was injected into the plenum in the radial direction. The plenum was approximately 3.5 cm high. The plenum chamber buffered the air flow and dispersed it evenly through a perforated plate with holes less than 45 microns in diameter. Above the perforated plate was the fluidized medium.

The compressed air was provided by Rutgers University and was set at 85 psi (586 kPa). A valve first dropped the pressure to around 1 psi (6.89 kPa). The compressed air was then further regulated by a rotameter. The rotameter is essentially a valve with a maximum volume flow rate of 40 scfh (1.13 m^3/hr). It could be set through the use of a dial that would open or close the valve. The instrument read out in percentages of 40 scfh. A pressure gauge was located after the rotameter and before the air inlet to the fluidized bed. The pressure gauge was an Omegadyne PX309 – 005G5V 0-5 psig pressure transducer. It was powered by a 0-25 V external power supply. A schematic of the set-up can be seen in Figure 30. A photograph of the basic set-up can be seen in Figure 31

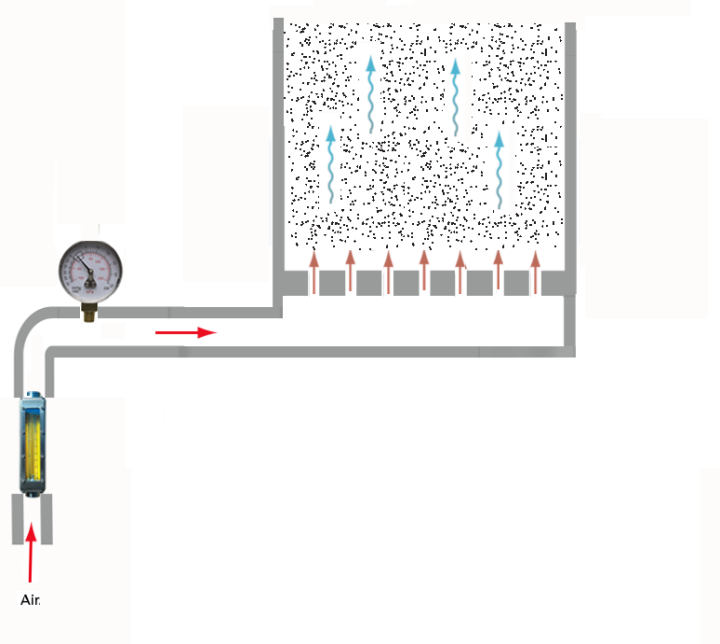

Figure 30: Schematic of basic fluidized bed set-up

Figure 31: Photograph of fluidized bed set-up

3.2 Fluidized particles

Two different types of particles were used as the fluidizing medium: ground Al_2O_3 and round glass beads.

3.2.1 Properties of ground Al_2O_3

Ground alumina oxide (ranging in diameter from 45 to 125 microns) with a density of 3989 kg/m^3 was used as the fluidizing medium. The particles were Geldart size A. The bed was filled with enough alumina oxide such that the aspect ratio (ratio of the height of the fluidized bed at incipient fluidization to the diameter of the bed) was kept at 1.5. The minimum fluidization velocity was determined to be 0.0100 m/sec and the pressure drop at U_{mf} was 7900 N/m^2/m. (*Appendix A*: Determination of Umf)

3.2.2 Properties of round glass beads

Round glass beads were used with a density of 2475 kg/m3 in the size range of 45 to 90 microns. The particles are Geldart size A as well. Similarly, the bed was filled with glass beads such that the aspect ratio was kept to 1.5. The minimum fluidization velocity was determined to be 0.0106 m/sec and the pressure drop at U_{mf} was 9935 N/m^2/m. (*Appendix A*: Determination of Umf)

3.2.3 Difference in behavior between glass beads and Al_2O_3 particles

The manner in which the particles will pack is dependent on many parameters, but most generally it is dependent on the particle shape. Table 2 gives some generic values for voidages (not to be mistaken with “voids” which is the term for excess gas in the bed which appear like bubbles) for particles of different shapes, particle size distributions, and packing methods. ‘Loose’ refers to packing without any agitation of the material, whereas ‘tapped’ refers to agitating or vibrating the material to allow for tighter packing.

	Round				Ground	
	Ordered - monodisperse	Loose - monodispere	Tapped - monodisperse	Tapped – multisize	Tapped - monodisperse	Tapped - multisize
Voidage	0.26 – 0.66	0.41	0.36	0.29 – 0.361	0.21 – 0.94	0.552

Table 2: Selected voidages from German [1989].

German [1989] states when providing porosity values for monodisperse (multiple sized) non-spherical particles, "each case must be treated on an individual basis".

Some specific properties of the ground alumina oxide (Al_2O_3) and round glass beads used in the experiments are shown in the table below:

	Shape	Dia (μm)	$\rho_{material}$ (kg/m^3)	ρ_{loose} (kg/m^3)	ρ_{tapped} (kg/m^3)	$\varepsilon_{loose,\ packed}$	$\varepsilon_{tapped,\ packed}$	$\varepsilon_{fluidized}$	Bed height rise
Al_2O_3	Ground	45 – 125	3989	1035	1066	0.740	0.733	0.766	10%
Glass Beads	Round	45 - 90	2475	1463	1505	0.409	0.392	0.437	4%

Table 3: Properties of fluidized mediums

The loose and tapped densities were measured and the voidages calculated based on the density of the pure material. Alumina oxide can have a sphericity of 0.3 [Howard 1989], which could lead to the very high voidages seen in the table. The bed height rise was determined experimentally. Further details are provided in *Appendix A*: Determination of Umf.

Once fluidized, the voidage of the ground alumina oxide increases by ~3% while the voidage of the round glass beads increases ~7%.

The shape of the particle will also affect the local gas flow in the bed. Air flow moves around the ground and round particles differently, with the flow around round particles being more predictable than it is around ground particles. Ideally, the flow

[1] For diameter ratio (largest diameter / smallest diameter) of 2.6
[2] For irregular shaped coke particles

around each round particle should be the same whereas with ground particles, since no two particles are alike, the flow around each will be different.

3.3 Description of submerged objects

Two hollow plastic spheres of radius $R_{Large\ Sphere}$ = 4.775 cm $R_{small\ Sphere}$ = 3.334 cm and with negligible wall thickness were used as the test spheres. The large sphere has a 0.15875 cm hole made during its manufacturing while the smaller sphere has a dimple. The hole/dimple was used to stake the sphere and attach it to an 8-32 threaded rod. The large sphere weighed 36 grams while the small sphere weighed 49 grams.

In certain experiments, a disk of the same radius as the small sphere was used. The disc was 0.635 cm in height and manufactured out of Teflon. A hole for an 8-32 rod was drilled into the center of the disc. The disk was used rather than the sphere because the flat surface of the disk removed the geometry of the rounded top of the sphere. A rounded top promoted particles sliding out of the hood. As reported by Peeler [1982] and Kurusaki *et al* [1988], particles will slide down the sides of the tube from the top. By removing particle sliding due to geometric effects, particle circulation within the hood due to wake effects could be isolated.

3.4 Experiments to determine forces on submerged objects in a fluidized bed

For the experiments measuring the forces on submerged objects, both the sphere and the disk were used as test objects. The object was held in place by a support beam with two legs above the bed. The support essentially straddled the fluidized bed. Either leg of the support was anchored to a base of sand which in turn stood on scissor jacks.

Data was recorded using two methods: manual readings from a scale and automated readings using a force sensor. For experiments with manual readings, a weighing scale was placed on each of the scissor jacks and the support was placed on the scales. The weighing scales had a 1 gram resolution. The disk or sphere was attached to the support by a threaded rod (size 8-32) staked through the top of the object. The other end of the rod was threaded through the support so that when turned, the object would move in and out of the bed. Since the support was mobile, the object could be placed anywhere within the bed. Initially, it was held above the level of the fluidized bed and the scales were zeroed. The disk or sphere was turned a predetermined distance into the bed and the mass was measured on the scales. As the object was submerged, it would be subjected to the forces within the bed. A decrease in the force measured by the scales indicated an increase in the downward force on the sphere. This was repeated and readings were taken until the force on the disk or sphere was unchanged with increased penetration. Since the object was detachable, the same apparatus could be used to determine the loads on all objects tested.

Data was also taken with automated force readings. Here the scales were removed and the 8-32 threaded rod was replaced with a 4-20 rod. The rod was then screwed into a force sensor. The force sensor was a Futek LSB200 Minature S Beam Load Cell with a maximum capacity of 250 g. It was connected to a Futek Strain Gage Amplifier (Model number CSG110) which feeds data to a computer via a COM port. The amplifier receives power from an external 25V power supply. The equipment came pre-calibrated such that the output of the amplifier could be converted to grams. The data could be read out through LabVIEW. Through LabVIEW, the data sampling rate could be set. The sensor

itself was mounted to the support. The object was lowered into the bed by lowering the scissor jacks on which the support stood. Data was collected for a minimum of 30 seconds at a sampling rate of 2 Hz at each submersion depth.

Although the automated readings allowed for acquiring several data points at each level, the set-up for the manual readings allowed for deeper penetration within the bed. The set-up for automated readings was limited in the depth to which the object could be submerged by the maximum expansion/contraction of the scissor jacks. However, the depth of submersion for the manual readings was only limited by the length of the threaded rod, which is readily available in many sizes.

Experiments were run with the large sphere in Al_2O_3, the small sphere in Al_2O_3, the small sphere in glass beads, and the disk in glass beads. Experiments were also run with the small sphere in Al_2O_3 with the sphere off-center by 5 cm.

A schematic of the set-up with manual readings is shown in Figure 32, while the set up for automatic readings is shown in Figure 33. Photographs of the assembly can be seen in Figure 34 and Figure 35.

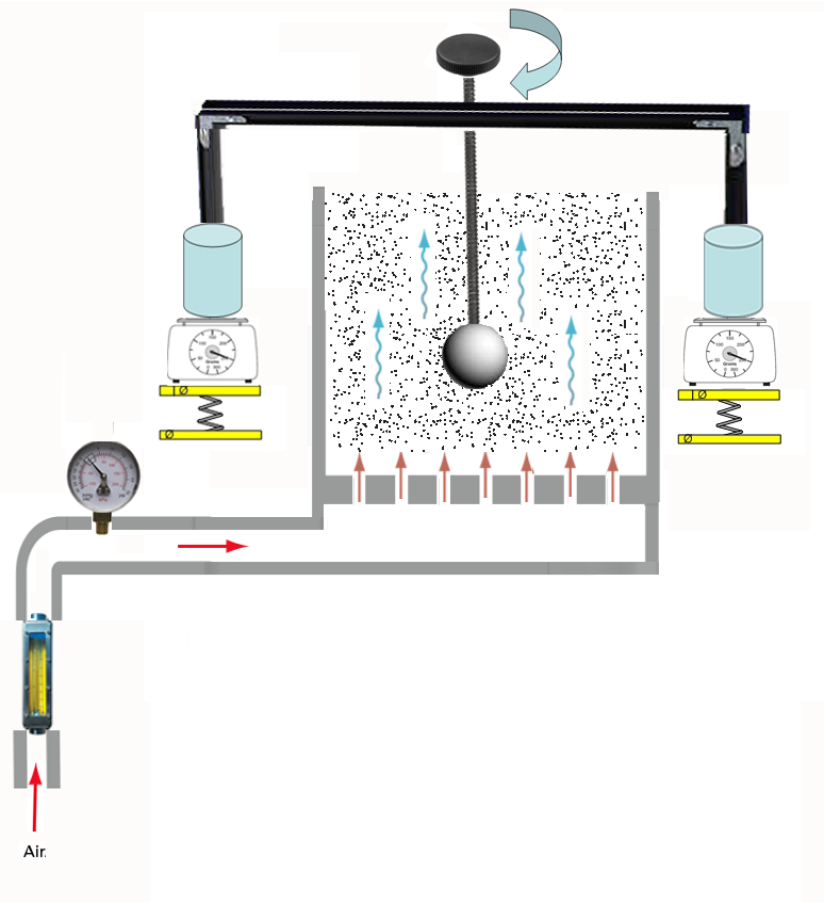

Figure 32: Set-up for experiments measuring forces on submerged objects using manual readings

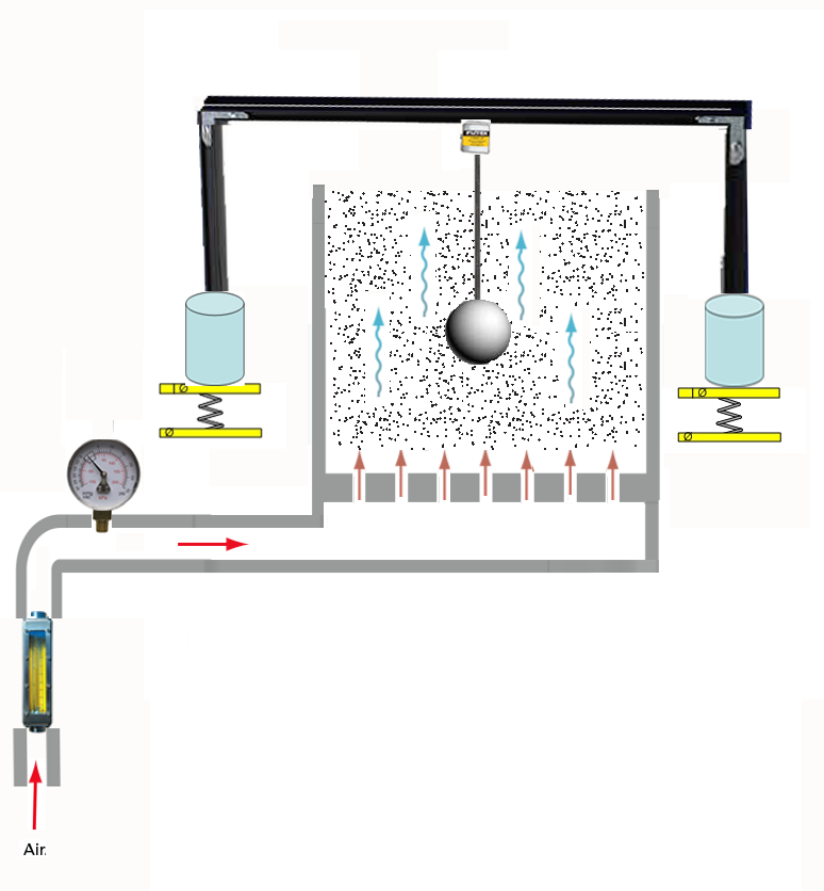

Figure 33: Set-up for experiments measuring forces on submerged objects using a force sensor

Figure 34: Photograph of assembly for measuring forces on submerged objects shown outside of bed

Figure 35: Photograph of assembly for measuring forces on submerged objects shown inside bed

3.5 Experiments testing the shear within the de-fluidized hood

Experiments were run to test the shear force within the hood due to the particles within the de-fluidized hood. A dead region of particles would exhibit a much larger resistance to motion than the fluidized region of particles. Therefore, by measuring the force required to push a rod through the de-fluidized hood, one could determine the regions of de-fluidized material and their degree of fluidization, as well as the boundary between the de-fluidized sections and the fluidized surroundings. Experiments were run with the small sphere in Al_2O_3.

A fluidized bed is a very stochastic environment, meaning that at any two instants, the bed may experience different shear forces at the same location. The size of particles occupying the space, the existence of a void or a void wake, slight variations in

bed pressure could all lead to different local bed properties at different instants. Therefore, in order to make any conclusions regarding the frictional resistance of the de-fluidized hood, it is necessary to conduct the same experiment several times. In order to gain a large number of data sets, an experiment was constructed that was automated and could continuously take data over a long period of time (on the order of 10 hours).

An automated experiment was devised where a rod would be pulled through the bed at various heights above a submerged object. The rod was attached to a motorized trolley carrying the aforementioned Futek force sensor. As it was pulled through the bed, the rod would rotate a pivot on the trolley, causing a load to be applied to the force sensor installed on the trolley. This would give a measure of the force required to pull the rod through the bed. The trolley was connected to a traversing screw that was turned by an automated motor. By controlling the motor with a computer, the experiment could be run several times. The number of iterations was limited by the potential for the sensor or the motor to overheat. A small nut was added to the tip of the rod to amplify the shear force.

The pivot was a block of acrylic with impinging stampers affixed vertically on both ends, and it had a horizontal hole in the center for which a rod could be screwed. The pivot was attached to the base of the trolley with a bolt through the center horizontal hole. The bolt was situated within a double walled ball bearing. This allowed for frictionless rotation of the pivot. The trolley base had a force sensor attached to it. As the pivot moved back and forth, the stamper on the pivot would compress the force sensor. Forces were measured during one-direction of travel and therefore only one side of the trolley required a force sensor.

Figure 36 shows a diagram of the trolley in the loaded position.

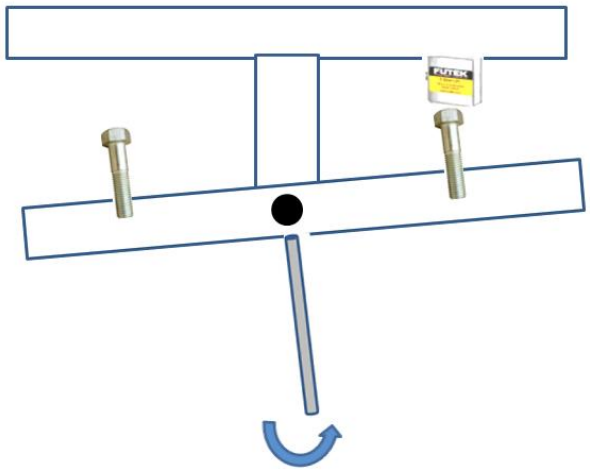

Figure 36: Schematic of trolley

The pivot and the trolley base made up the trolley. The trolley was attached to the previously mention traversing mechanism, which was a 13" Velmex® Unislide. The Unislide is a ball screw that moves in fine increments linearly as the screw is turned. This particular Unislide moves 0.025" per turn of the ball screw. The ball screw had a mounting plate attached via a ball screw nut. The trolley was mounted to this plate.

The turning mechanism for the Unislide was connected to a motor through a flexible shaft coupling. The motor turned the Unislide, thus moving the trolley. The motor is an integrated stepper motor with a stepper motor drive and controller manufactured by Lin Engineering (model Silverpak 17C). It has a maximum holding torque of 84.8 oz-in. One revolution of the motor is 256 microsteps. A full step rotates 1.8^0. The motor has a step revolution of ½ to 1/256, meaning that it can move in these fractional increments of 1.8^0. This allows for extremely precise position control. A motor control program created by Lin Engineering used LabVIEW to control motor speed, position, and direction. Other control features included looping and delaying the motor.

The trolley, motor and Unislide assembly were attached to a four legged structure that saddled the fluidized bed. Slots were made in the top of the structure such that the

assembly could traverse across any chord of the fluidized bed and measure shear forces at various locations off center.

In order to measure the resistance of the de-fluidized hood, the sphere could no longer be suspended from its vertical axis because the force sensing rod would collide with the rod suspending the sphere. Instead, the sphere was staked along its horizontal axis by a rod. The rod was connected to a 90^0 couple which connected to a vertical rod. The vertical rod was installed onto a smaller 4" Unislide. The Unislide was mounted to the wall of the fluidized bed. The mechanism for suspending the sphere allowed for vertical positioning of the sphere. Figure 37 shows a schematic of the entire set-up.

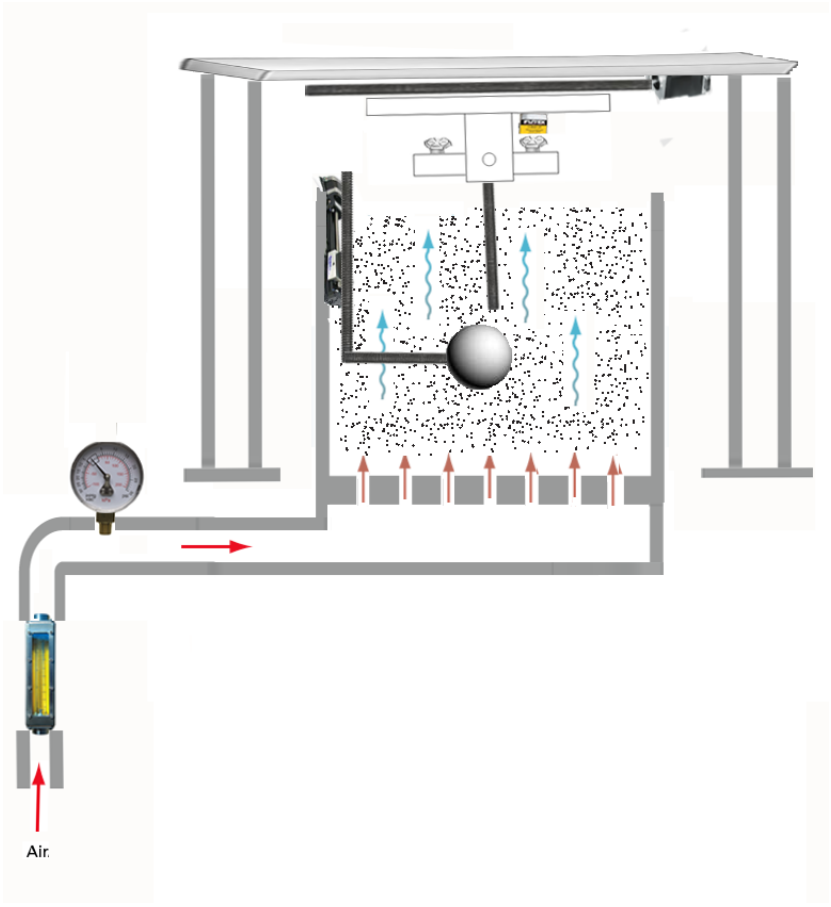

Figure 37: Set-up of experiments to measure resistance of de-fluidized hood

3.6 Experiments to measure drag on a spherical probe within the de-fluidized hood

In an attempt to measure the influence of the hood on the air flow around a neighboring structure, an experiment was designed where the drag on a probe of R = 1.27 cm placed behind the small sphere of R = 3.334 cm was measured. The bed was fluidized with glass beads. The sphere was positioned using the same mechanism as in section *3.5 Experiments testing the shear within the de-fluidized hood* For all experiments, the submerged sphere was placed 11.43 cm below the surface, or 3.43R deep. The probe was attached to a 4-40 rod. The rod was attached into a 4-40 threaded hole manufactured on the Futek force sensor.

The probe and the sphere were placed at the center of the fluidized bed. The probe was placed directly over the center of the sphere. The height to which the probe submerged could be varied by using rods of different lengths. The probe was placed while the bed was still fluidized – the air flow was at U_{mf}. The force on the probe would now be recorded continuously as the flow rate would be decreased to $0.5U_{MF}$ and raised back to U_{mf}. Data was collected at 20 Hz with LabVIEW. The probe would then be attached to a different length 4-40 rod which submerged the probe to a different depth, and the experiment would be repeated. A schematic of the set-up is shown in Figure 38.

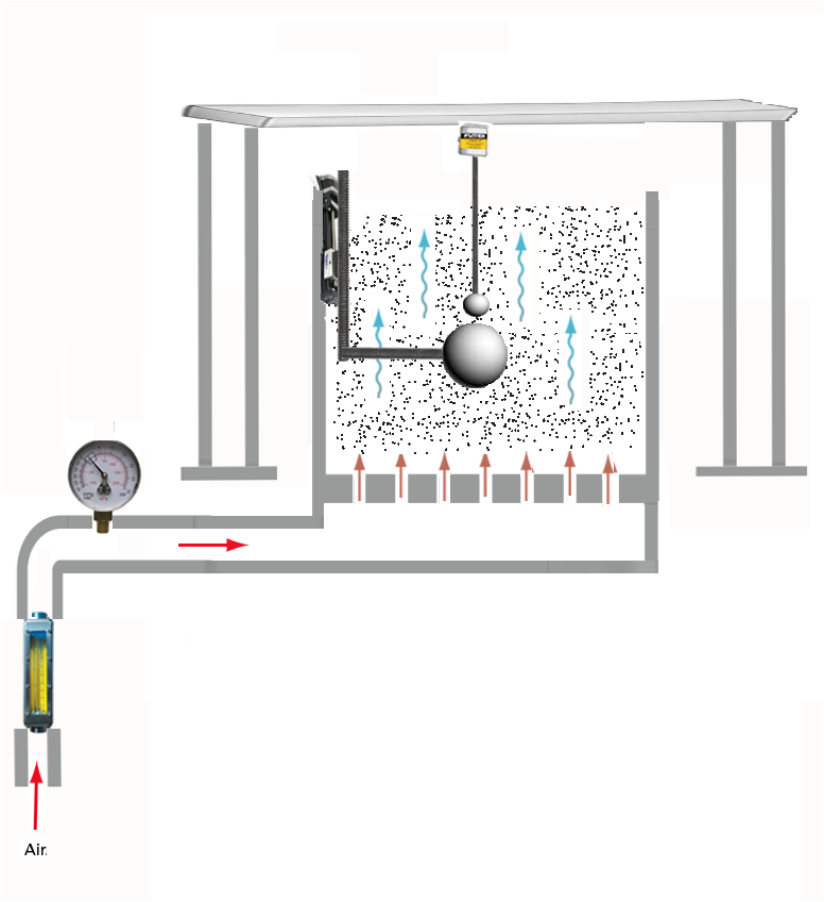

Figure 38: Schematic of set-up to measure drag on a probe within the de-fluidized hood

3.7 Experiments to determine the radial extent of the de-fluidized hood

In order to better determine the structure of the de-fluidized hood, bed collapse experiments were conducted with the disc submerged in the fluidized bed. The bed would begin in a fluidized state and the air flow rate to the fluidized bed would be cut off. The bed would collapse, and the bed height was measured at various points above the submerged object and around it. As the air flow rate to the bed was cut off and the bed collapsed, a mound would form above the submerged object. The depth at which the surface collapsed to the same height everywhere would be considered the depth at which the de-fluidized hood re-fluidizes.

An experiment was conducted to measure the surface height change over the submerged object. The set up was the same as the set-up for measuring the forces on a submerged object with a few alterations. The weighing scales were no longer needed and removed. More importantly, a grid with a 10 mm vertical and horizontal resolution was placed within the bed to measure the bed surface height. The grid was aligned with the dead bed height. The surface height at various radial distances was measured using this ruler. Furthermore, the submerged object was changed from a sphere to a flat disk of 0.6 cm height. Its radius was kept the same as the small sphere – 3.334 cm. The reasons mentioned for replacing the sphere with a disc were discussed in section *3.3 Description of submerged objects.* Glass beads were used as the fluidizing medium. Figure 39 shows a schematic of the set-up.

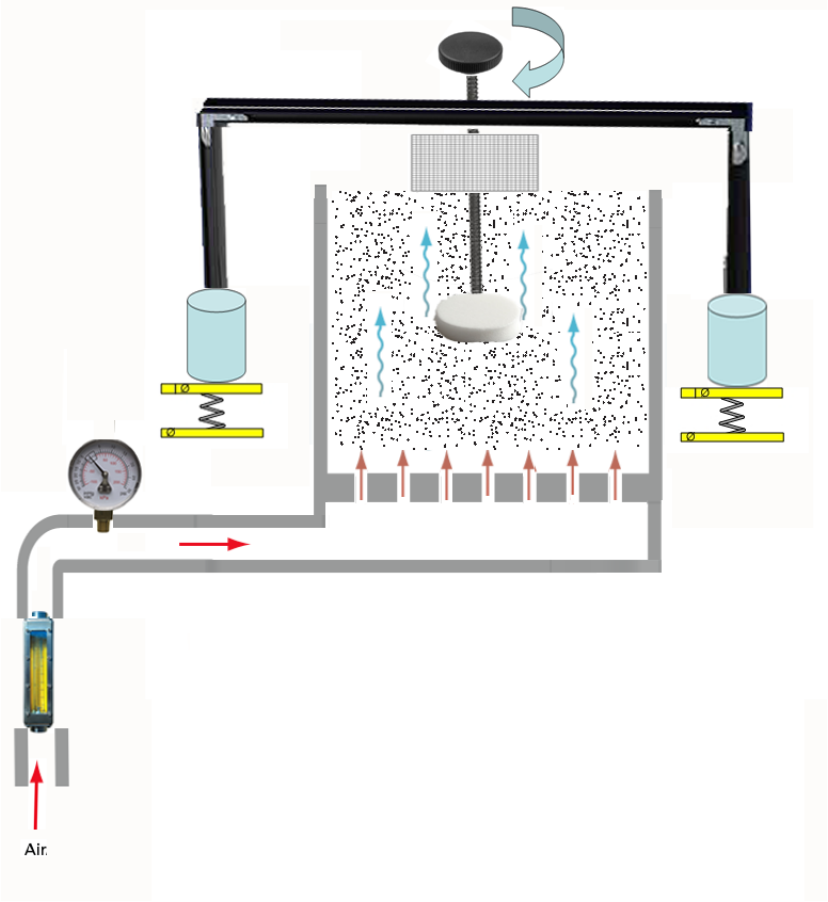

Figure 39: Schematic of set-up to measure collapsed bed height above disc

3.8 Experiments to determine the normal force exerted by the de-fluidized hood

The normal force exerted by the de-fluidized hood would provide a measure of the air flow within the hood. The normal force exerted by a dead bed would be extremely high whereas the normal force exerted by a fluidized bed would be negligible. At air flow rates between fluidized and dead, i.e. percolating regimes, the normal force would be between zero and the normal force at dead bed. The upward drag imposed by the air flow would lower the effective normal force, as alluded to by Liu [1960], Batchelor [1988],

and Anjaneyulu and Khakhar [2001]. Using this principle, an experiment was designed to test the normal forces within the hood.

The same set-up as used in Figure 39 was used for these experiments. The bed was fluidized with a submerged disc using the glass beads. The air velocity was held to U_{mf}. The ruler was unnecessary and removed. Weights of the same shape and volume were placed at the surface of the bed above the submerged disk. The radial position along the disk at which the weight sunk was measured and recorded. Inward of this position (towards the center of the disk) the hood supported the weight. Outward of this position, the bed could not support the weight and it would sink. With the disk at the same depth, another weight was tested. This gave multiple normal forces along the radius of the submerged disk at a particular depth. The depth of the submerged disk was then increased and the experiment was repeated.

The weights were ¼-20 nuts made of different materials – aluminum, steel, brass and titanium. Additionally, a brass nut whose center was filled in with plastic and another brass nut with a steel center were used. The aluminum nut weighed 1.089 grams, the titanium nut weighed 1.853 grams, the steel nut weighed 3.143 grams, the brass nut weighed 3.402 grams, the brass/plastic nut weighed 3.499 grams, and the brass/steel nut weighed 4.329 grams.

Chapter 4: Experimental Results

The following section presents the results of the experiments described in Chapter 3: Experimental Set-Up

4.1 Forces on submerged objects within a fluidized bed

The following section presents the results of the experiments described in section *3.4 Experiments to determine forces on submerged objects in a fluidized bed.* Object size, particle type, distance from the fluidized bed wall and object shape were tested in order to identify some of the variables affecting the de-fluidized region.

4.1.1 Forces on different sized objects within the same medium

The forces on the large sphere submerged in Al_2O_3 were obtained in Rao 2009. In order to determine the effect of object size on the weight force of the de-fluidized hood, the same experiment from Rao 2009 was conducted on a smaller sphere. The results are compared and shown in Figure 40.

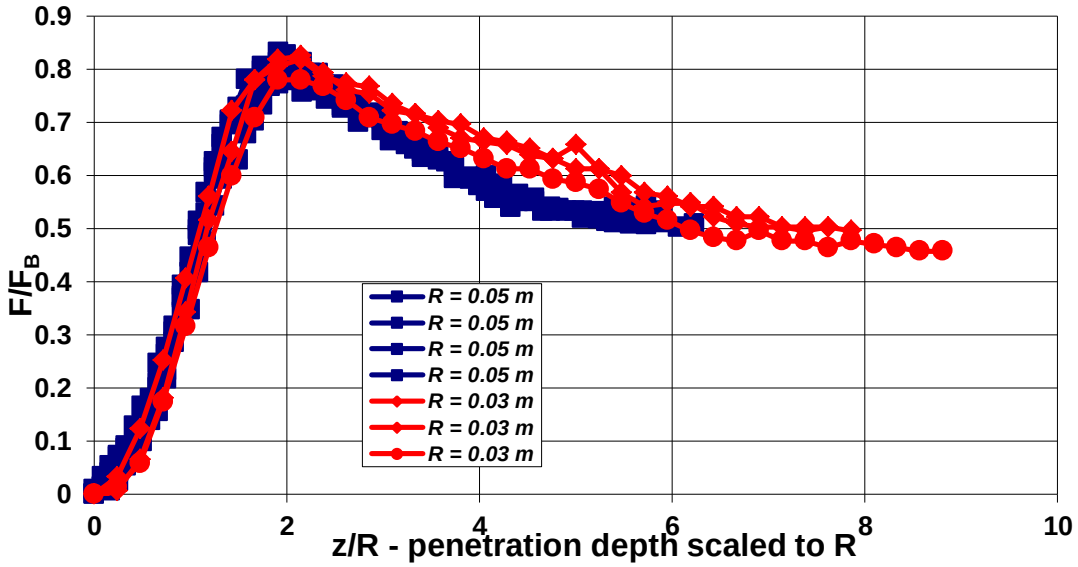

Figure 40: Comparison of force on two objects (R = 0.05 m and 0.03 m) in Al_2O_3

In Figure 40, the submerged object penetration, z, has been scaled to the radius of the sphere, R. The force has been scaled to the buoyant force, F_B on the fully submerged object. This is calculated through Equation 19.

$$F_B = \rho_{mf} g V = \frac{\partial P}{\partial z} V$$

Equation 19

where

F_B = buoyant force

ρ_{mf} = density at minimum fluidization

g = gravitational acceleration

V = volume of submerged sphere

dP/dz = pressure gradient around submerged sphere (measured in Rao 2009)

The data shows three regions with regards to the force development. In the region from $0 \leq z/R < 2$, there is an increasing upward loading on the sphere. In this region, the sphere is partially submerged in the fluidized bed and the bed is exerting a buoyant force on the sphere. At $z/R = 2$, the sphere is completely submerged. After $z/R \geq 2$, the forces begin to decrease, indicating that a downward load is being exerted on the sphere. This is the load due to the de-fluidized particles above the submerged sphere which will act to sink the sphere. At some depth, the slope of the force data goes to zero. This indicates that the de-fluidized region ceases to grow, and consequently the downward loading on the sphere no longer increases. At this distance away from the submerged sphere, the bed has re-fluidized.

The scaled force for the two spheres (R = 0.05 m and R = 0.03 m) matches in the range of $0 \leq z/R \leq 2$, indicating that buoyancy is the primary force exerted on the sphere

over this range. However, neither maximum is at $F/F_B = 1$. Both have a maximum of $F/F_B = 0.8$. In the case of a sphere submerged in a single phase fluid, such as a tank of water, F/F_B at $z/R = 2$ should equal 1 indicating that the buoyancy on the sphere is the only load on the sphere. However, in a fluidized bed the de-fluidized region takes shape and exerts a force before the sphere is completely submerged. The similarity in maximum force between the different sized spheres indicates that the initial development of the de-fluidized hood is the same for objects of the same shape but different size.

When $z/R > 2$ the force diverges, with the height of the de-fluidized region being smaller for the larger sphere than it is for the smaller sphere. The de-fluidized region on the large sphere was affected by wall effects and these same effects render it difficult to delve deeper into the de-fluidized region behind the large sphere. The de-fluidized hood height as measured from the center of the spheres ($z/R = 1$) was 6.15 R for the small sphere and 4.1R for the large sphere.

4.1.2 Forces on the same object within the different fluidizing media

In order to determine the effect of different particle types on the overall force balance of a sphere, the smaller sphere with $R = 0.0334$ m was weighed at different depths within a fluidized bed of ground Al_2O_3 and round glass beads. The differences in particles have been detailed in section *3.2 Fluidized particles.* The results are show in Figure 41

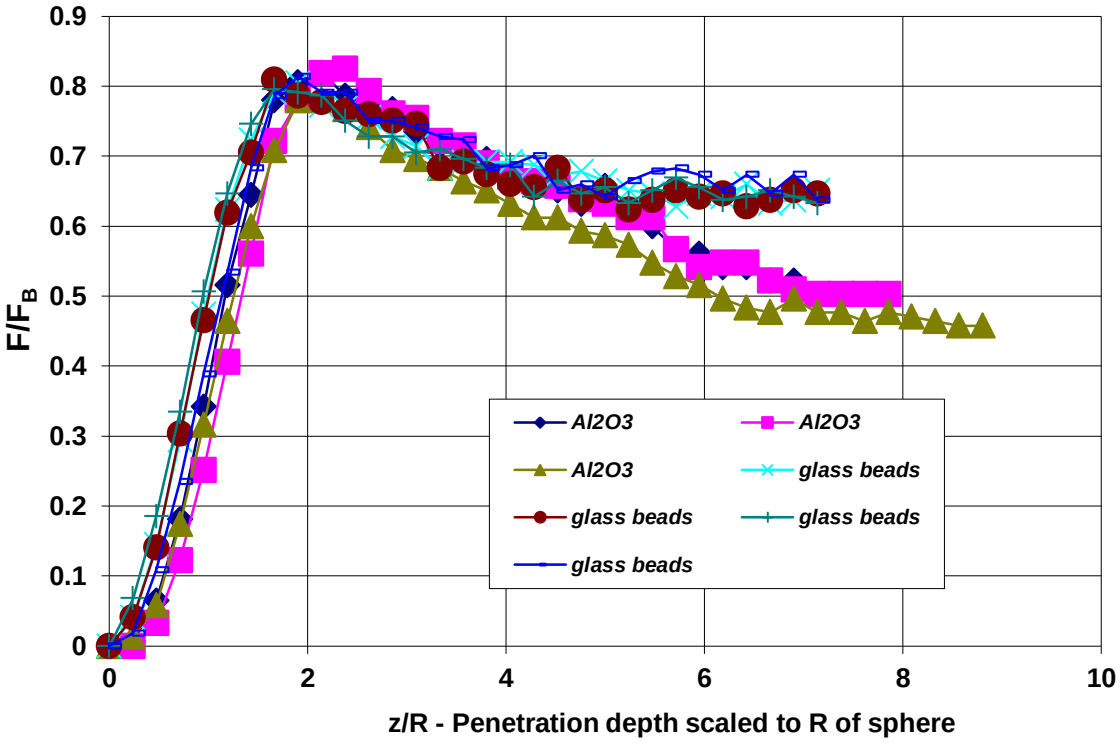

Figure 41: Effect of fluidizing media on forces on submerged sphere (R = 0.03 m)

The results have been scaled to the buoyant force of the sphere, while the penetration depth has been scaled to the radius of the sphere. The three regions in the force development are again evident. The impact of the de-fluidized hood is less on the sphere in glass beads compared to the impact on the sphere in Al_2O_3. The de-fluidized hood height as measured from the center of the sphere (z/R = 1) is 6.15R for the Al_2O_3 and 4.25R for the glass beads. The de-fluidized region thus re-fluidizes at a shallower height for the glass bead media. From this, it is evident that due to packing characteristics round particles, provide an easier path for air flow thus allowing for quicker re-fluidization than ground particles.

The de-fluidized hood weight is $0.53F_B$ in Al_2O_3 and $0.33F_B$ in glass beads. The hood thus weighs less in the glass bead media. The difference in weight of the de-fluidized regions can also be attributed to the particle packing. Round particles will have

a higher voidage than ground particles. Therefore, the de-fluidized region for the round glass particles will be occupied by more air than for the ground Al_2O_3 particles. Additionally, the Al_2O_3 is denser than the glass beads, with the density being 3989 kg/m^3 for the former and 2475 kg/m^3 for the latter.

4.1.3 Wall effects on the de-fluidized hood

The effect of the sphere position within the hood on the overall force balance was tested as well. The prime concern was to eliminate wall effects. The large sphere had an object to bed radius ratio of ~0.42 whereas the small sphere had an object to bed radius ratio of 0.29. As has already been seen, the wall effects may have played a role in reducing the size of the de-fluidized region for the large sphere compared to the size for the small sphere.

The force on the small sphere located at the center of the fluidized bed was compared to the force on the small sphere located 5 cm off center. The results are shown in Figure 42.

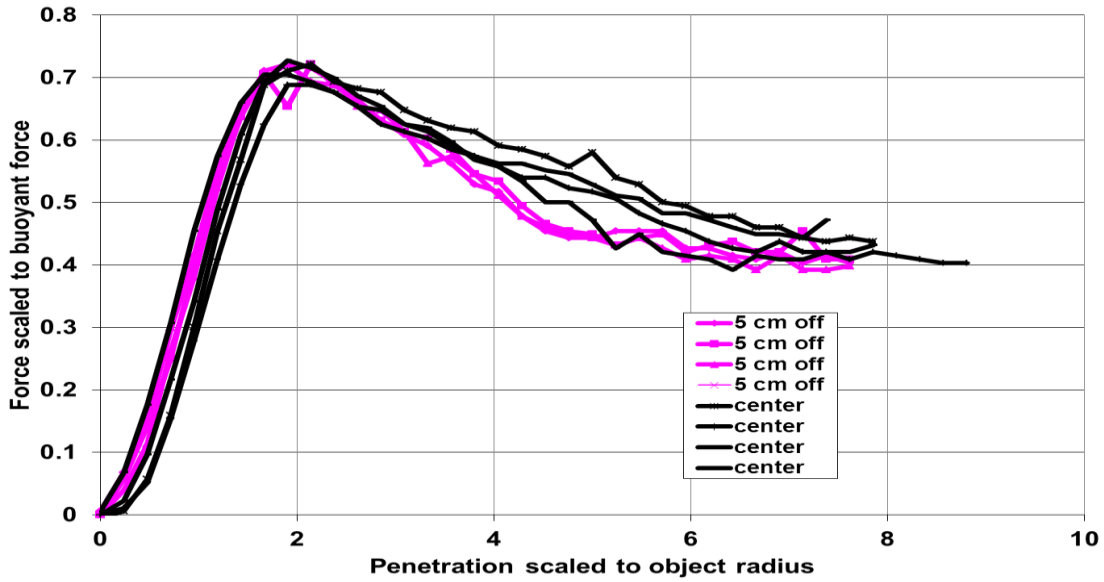

Figure 42: Effect on object position on small sphere (R = 0.03 m)

The sphere was moved 1.5 $R_{Small\ Sphere}$ off center. However, the final force and shape due to the de-fluidized hood as inferred by the weight on the object is negligible. Oscillations in the data for the sphere aligned with the center may be due to the increased likelihood of finding a void at the center.

For all subsequent experiments, objects of radius 0.03334 m were used. This radius best replicates an object in a fluidized bed of infinite radius, thus eliminating wall effects on the de-fluidized hood.

4.1.4 Forces on a submerged disk

In order to compare the effect of different shaped objects on the de-fluidized region, a disk of radius 0.03334 m was inserted into the bed of glass beads and the force was measured using the Futek force sensor. The results are shown in Figure 43.

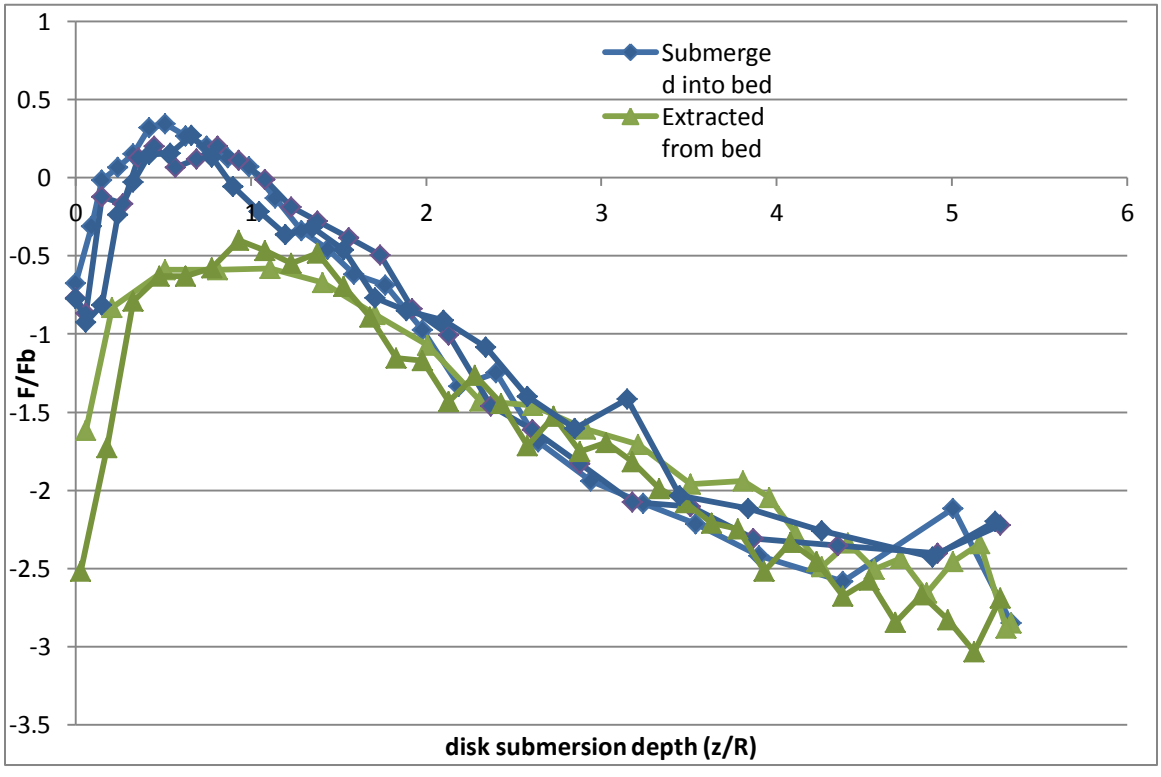

Figure 43: Force on a disk as it is submerged and extracted from a fluidized bed of round glass beads

The y-axis has been scaled to the buoyant force on the disk while the x-axis has been scaled to the radius of the disk. Regarding the scaling of the x-axis, while scaling to the height of the disk would allow for determining the weight force at the depth corresponding to complete submersion, it would make comparison to the data on the sphere difficult because the length scales for comparing the size of the de-fluidized regions would be different. Therefore, the same scaling as used for the sphere data has been applied here as well.

While submerging the disk, the weight force at $z/R = 0$ (when the disk is out of the bed) is negative, indicating a downward loading on the disk. Voids cause particles to splash and sit on top of the disk even before the disk has been submerged. The weight force of these particles causes the initial measurement at $z/R = 0$ to be negative. While voids were present for the sphere as well, the initial measurement at $z/R = 0$ for the sphere was $F/F_B = 0$. Particles splashed on top of the sphere as well but could not rest on the surface as readily as they could on the disk surface due to the curvature of the sphere.

The hysteresis seen between submerging and extracting the disk from the bed in Figure 43 is due to the action of pulling something out of a fluidized bed versus submerging something into a bed. While pulling a flat disk out, particles will accumulate on the surface of the disk and be pulled out as well. While submerging the disk, there are not nearly as many particles sitting on the disk. These extra particles pulled out while extracting the disk will increase the downward load as it is being pulled out of the bed.

The de-fluidized hood height above the disk as determined by the above experiments is 4.15R. The sphere of the same radius in glass beads had a hood height of

4.25R. This comparison shows that the de-fluidized height is very similar for objects of the same radius but different geometry.

The weight force on the disk due to the hood is $3.45F_B$. The weight force on the sphere due to the hood was $0.55F_B$. While the de-fluidized hood height may be the same for the two structures, the weight of the hood relative to the object is very different.

4.2 Shear within the de-fluidized hood

As described in section *3.5 Experiments testing the shear within the de-fluidized hood,* experiments were conducted to measure the shear by running an 8-32 rod above a submerged object. A rod was initially positioned at 7.62 cm from the fluidized bed wall in order to be sufficiently far away from the boundary layer of the fluidized bed (total fluidized bed radius was 11.5 cm). The rod was run 7.62 cm across the center of the fluidized bed with the rod crossing the center axis of the sphere after it had traveled 3.81 cm. To avoid any inertial effects, the rod moved at 0.127 cm/sec. After the rod traveled 7.62 cm, the motor reversed direction and the rod returned to its initial position. This was repeated 5 times. The sphere was lowered in 1.27 cm increments and measurements were taken at each depth. Data was sampled at 20 Hz.

The experiments brought to light an interesting feature of measurement techniques within fluidized beds. Within potentially de-fluidized regions, successive paths were influenced by the previous path. As the rod traveled through the bed, it plowed a path through the medium. It was observed that the path would not ‘clear’ or return to its initial state due to a lack of air flow over the experimental area. Experiments were run where the rod was paused for several minutes after each one-way travel.

Regardless of the delay time, it was observed that the path would never return to its undisturbed state.

The experiments provided results concerning the ‘degree of fluidization’ within the bed. The results shown in Figure 44 are taken from the experiment described above. The 5 sets of data from each depth are averaged. Only data from when radial positions between 4.5 cm (x/R = 1.35) to 5.7 cm (x/R = 1.72) across the bed are considered. Within this range, the force had reached a steady state value.

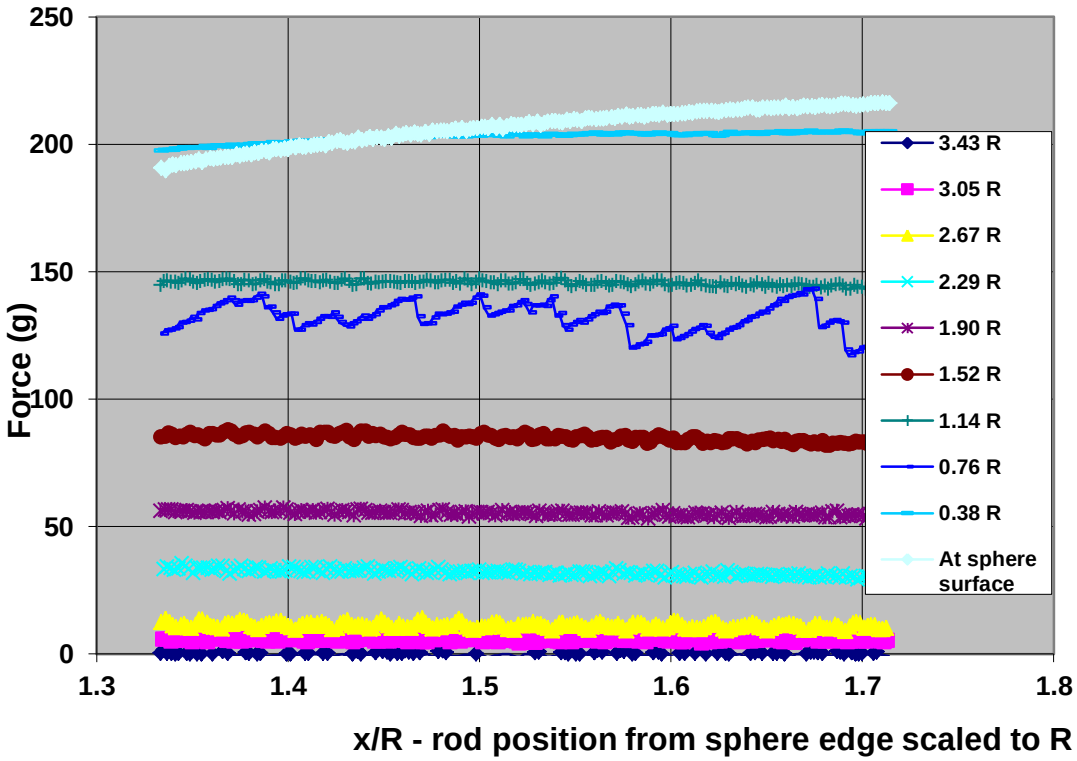

Figure 44: Shear within the de-fluidized hood

The x-axis describes the rod position along the sphere and has been scaled to the sphere radius. At x/R = 0, the rod would be at the edge of the sphere, while at x/R = 1, the rod is directly above the center of the sphere. The y-axis shows the resistance from the bed felt by the rod in grams.

Each line corresponds to a distance from the top of the sphere. At the sphere surface, the resistance from the de-fluidized region on the rod was highest at over 200 grams. At 3.43R away from the sphere surface, the rod felt no resistance from the de-fluidized region. The results show an increase in the force required to move the rod through the bed with increasing penetration depth.

The data at 0.76R shows an interesting characteristic. It has the same saw tooth pattern observed by Albert *et* al [2001] in Figure 20 characteristic of the stepped regime. The authors attribute this regime to the manner in which force chains propagate and proximity to a rigid surface. At 0.76R, the rod may be a critical distance away from the nearest rigid surface.

4.3 Drag on a spherical probe within the de-fluidized hood

The experiments described in section *3.6 Experiments to measure drag on a spherical probe within the de-fluidized hood* were conducted in order to get a better measure of the drag within the de-fluidized hood, and subsequently a measure of the air flow within the hood. Experiments were conducted with and without the submerged sphere. The flow rate was cycled between $0.5U_{mf}$ to $1U_{mf}$ and back to $0.5U_{mf}$. This corresponds to bed pressures of 3.96 kPa at $0.5U_{mf}$ and 5.92 kPa at $1U_{mf}$.

The experiment was conducted with the probe located 0R, 1.5R, and 3R away from the sphere surface. The goal was to determine the distance from the sphere at which the load on the probe would be unaffected by the existence of the submerged sphere. Figure 45 displays the average maximum load on the probe over several runs (three data sets with the submerged sphere, five data sets without the submerged sphere). The load

has been adjusted to account for the weight of the probe. As a result, 0 g indicates that there is no load on the probe.

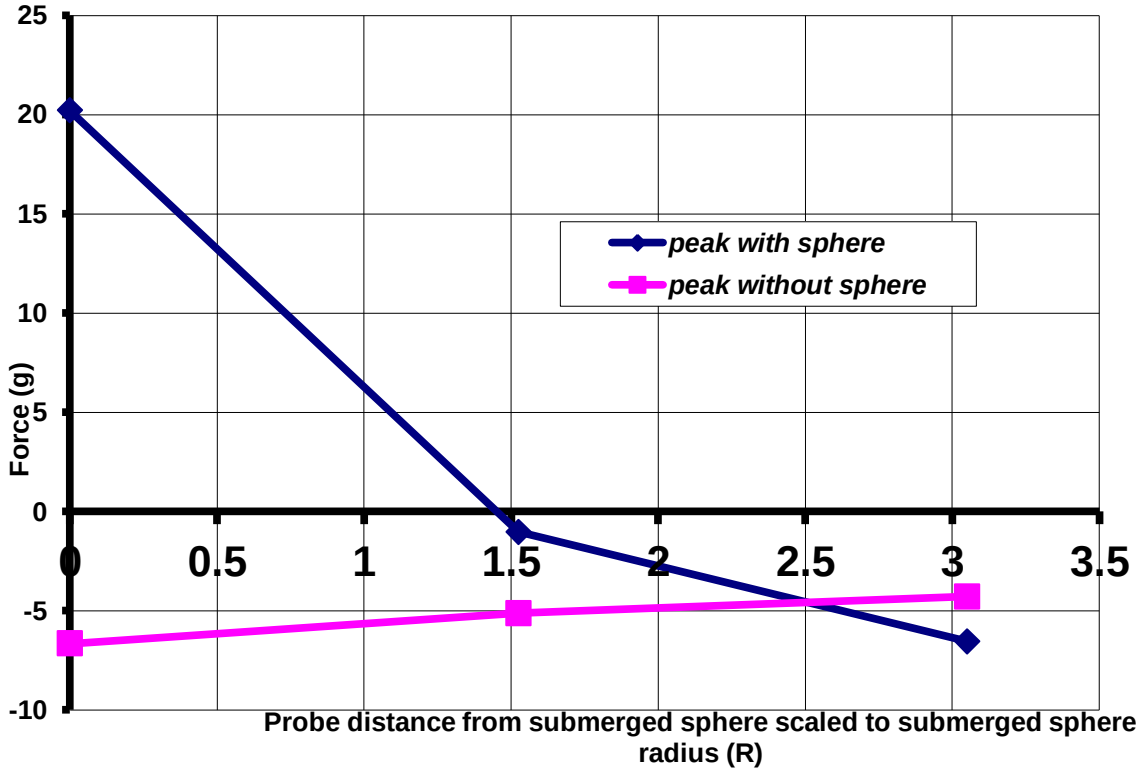

Figure 45: Maximum load on probe with and without submerged sphere at various depths

The peak with the probe directly above the submerged sphere surface is 20 g. This indicates that the probe is supported by the de-fluidized material in the hood of the sphere. The peak at this depth without the submerged sphere is -6.5 g. The probe itself will have a de-fluidized hood which would create a downward force on the probe. When the probe is approximately 2.5R away from the top surface of the submerged sphere (or 3.5R from the center of the sphere), the submerged sphere no longer has an effect on the load on the probe. In both cases, the load on the probe is the same. This indicates that at this distance away from a submerged sphere, a neighboring structure will be unaffected by the de-fluidized region.

4.4 Bed height collapse over a submerged objects

The experiments outlined in section *3.7 Experiments to determine the radial extent of the de-fluidized hood* were conducted with the disk with a radius of 0.03334m in a bed of the glass beads. Figure 49 shows pictures of the bed surface at fluidization and at collapse above the submerged disk at depths of 0.76R and 2.67R. The pictures are of the reflection of the surface on a mirror.

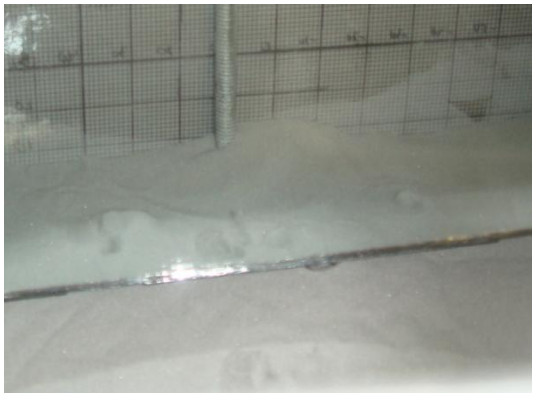

Figure 46: Fluidized bed surface above a disk submerged 0.76R deep

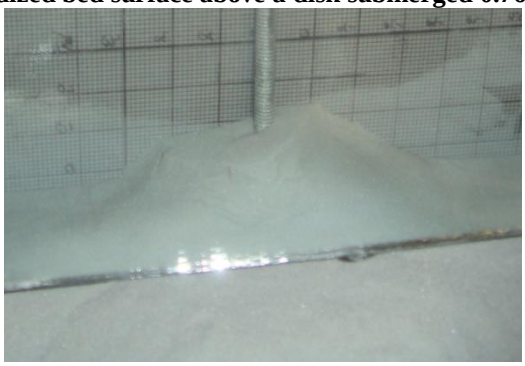

Figure 47: Collapsed bed surface above a disk submerged 0.76R deep

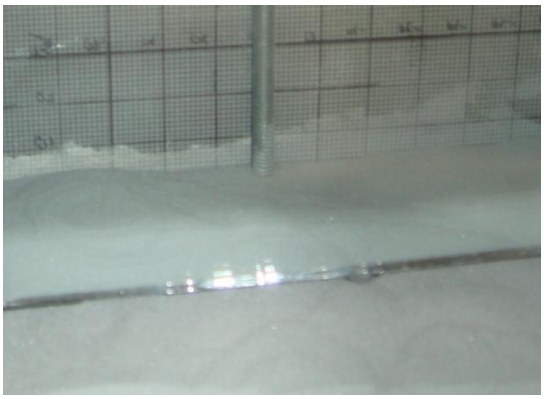

Figure 48: Fluidized bed surface above a disk submerged 2.67R

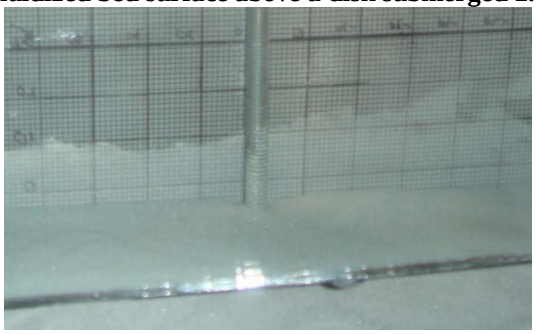

Figure 49: Collapsed bed surface above a disk submerged 2.67R

The change in surface heights from fluidized to collapsed were measured and shown in Figure 50 at various depths of the submerged disk. Voids were present along the periphery of the disk which disturbed the particles along the periphery, similar to what has been reported in the literature (Peeler 1982 and Kurusaki 1988). Therefore, in order to capture the effect of the de-fluidized region on the results and eliminate secondary effects due to voids, the collapse along the centerline, the point furthest away from the influence of the voids is the most relevant data to consider.

The change in the center line heights between fluidization and collapse from Figure 50 are shown in Table 4.

Distance from disk surface (scaled to disk radius R)	Height change (mm)
0.38R	0
0.76R	0
1.14R	-3
1.52R	-3
1.90R	-5.5
2.29R	-5
2.67R	-8

Table 4: Centerline collapse over a submerged disk

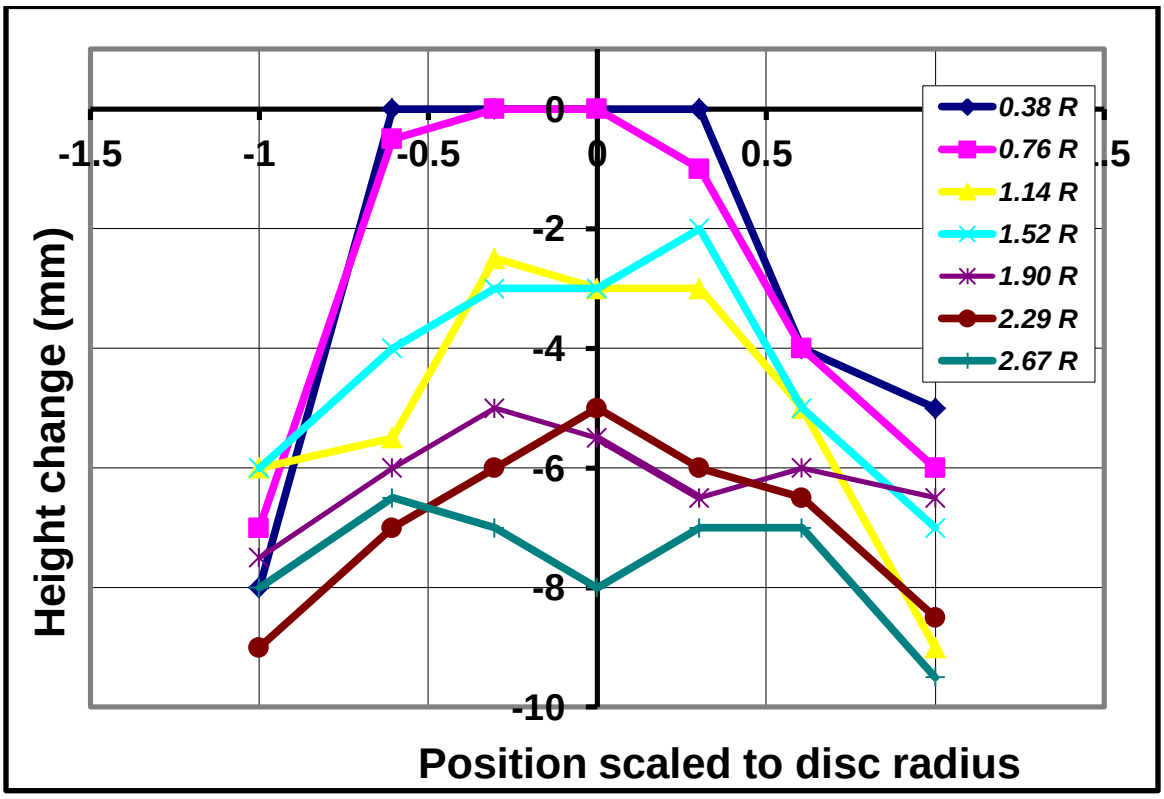

Figure 50: Change in bed surface height from fluidized to collapsed above a submerged disc at various depths

At a depth of 0.38R and 0.76R, the surface directly above the center of the disk did not collapse, indicating that the particles in this region are not fluidized and are stagnant. At depths above 0.76R, the surface above the center of the disk appears to collapse. It does not, however, collapse to the height of the surrounding fluidized region.

This indicates that this region is not collapsing because it was previously expanded, but rather that this region is percolating and experiences particle circulation with particles flowing out of the bottom of the hood and flowing in from the fluidized region into the top of the hood. Once the air flow is cut off, the particles in this region flow out of the hood without any fresh particles to replenish them. This would give the appearance of a collapsing surface. These observations of stagnant regions and particle circulation are key in describing the characteristics of the de-fluidized hood, which will be described in Chapter 5: Discussion of Results.

4.5 Normal force exerted by the de-fluidized hood

The experiment described in section *3.8 Experiments to determine the normal force exerted by the de-fluidized hood* was conducted to determine the normal force supported by the hood at various radial locations and disk submersion depths. The results are shown in Figure 51.

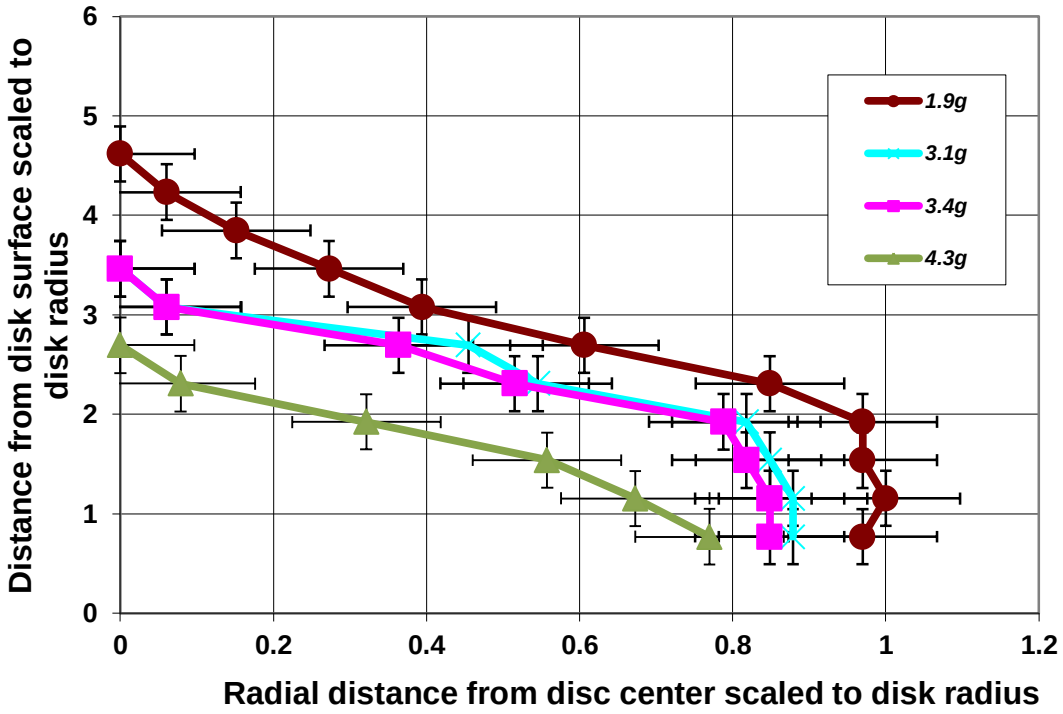

Figure 51: Normal force along disc at various disc submersion depths[3]

Figure 51 shows lines of constant normal force along the disk radius and heights above the disk surface. Below each line, the respective weights will be supported by the de-fluidized region and above the line the weight will not be supported. Error bars have been included representing the spatial resolution associated with the geometry of the ¼"-20 nut. The data shows the normal force decreasing further away from the disk and increasing towards the center of the disk.

Due to voids along the periphery of the disc, the normal force contour lines slope sharply down as they approach the edge of the disc. As the voids pass, particles inside the hood slide into the fluidized section of the bed.

[3] The 1.089 g weight has not been shown because it floated at every position, meaning that it was buoyant within a fluidized bed.

The normal force exerted by the bed will correspond to a flow velocity. As the air velocity increases, the normal force, which will be the sum of the drag on the particle and the weight of the particle, will decrease. At fluidization, the normal force supported by the bed would be 0 N (refer to Appendix *B.2 Force balance on a section of particles*). Each normal force obtained in Figure 51 will correspond to an air velocity. In order to determine these corresponding velocities, each weight used in the experiments was placed in a dead bed without a submerged object, and the air velocity at which the weight sunk was recorded. The correlations are presented in Table 5. Using these values, lines of constant velocity within the de-fluidized region above the disk are experimentally determined.

Normal Force (g)	*Superficial Velocity (m/sec)*
4.329	.005623
3.402	.006091
3.143	.00656
1.853	.007967

Table 5: Relation between normal force and fluidizing velocity

Chapter 5: Discussion of Results

The following section will use the results from Chapter 4: Experimental Results to determine the structure of the de-fluidized hood, including its dependence on the variables that were tested, the levels of de-fluidization and the air flow within the hood. A model is constructed predicting the weight force on a submerged object. Comments will be made concerning the de-fluidized region's effect on bed performance.

5.1 De-fluidized region dependence on particle type

Experiments were run varying several parameters in order to determine the effect of these parameters on the de-fluidized region. The results presented here suggest that the de-fluidized region and the force on a submerged object are dependent on the type of particle used in the fluidized bed. Beyond particle density, particle packing characteristics will alter the size of the region. Round particles, which have a lower angle of repose and higher voidage in packing, will exhibit a shorter de-fluidized hood compared to ground particles, which have a higher angle of repose and pack together "tighter" leaving less space for air flow to pass. Above the same immersed object, the round particle fluidized bed was found to have a de-fluidized region that was 1.9R shorter in height than the region for the ground particle bed.

5.2 Regions within the de-fluidized hood

Previous research has been unable to determine the fluidization levels within a de-fluidized hood. The region has been treated as being completely dead. If that were the case, the force on a submerged object would drop drastically as it was sunk into the bed.

Two hypothetical cases, one in which the region in the wake is entirely fluidized and one in which the de-fluidized region is entirely dead, are compared to the experimental data for the force on a small sphere in glass beads. If the wake were completely fluidized, the sphere would be buoyant. If the wake were completely dead, the sphere would experience a high downward force. The experimental data splits between the two hypothetical cases indicating that the wake region is neither completely dead nor completely fluidized but is of an intermediate state. The comparison can be seen in Figure 52.

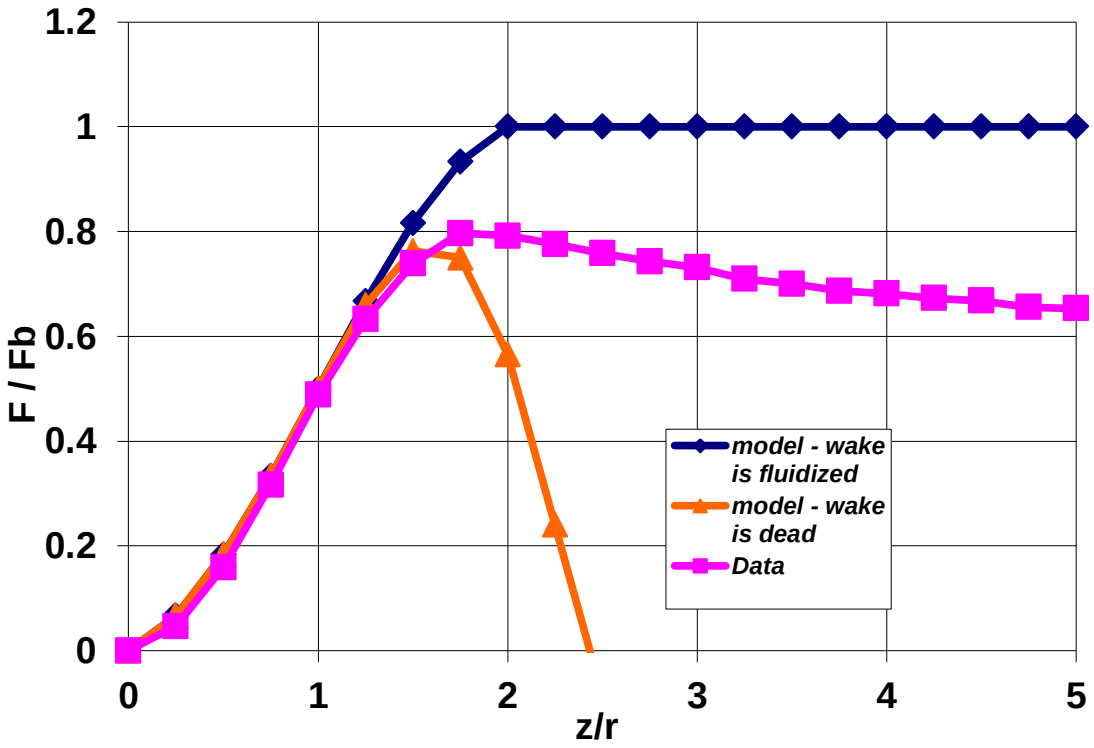

Figure 52: Completely fluidized wake, completely dead wake, and data compared for the smaller sphere in glass beads

The findings presented herein suggest that the wake region is not uniform in de-fluidization but has varying levels of de-fluidization. The results suggest the existence of five distinct regions within the de-fluidized hood. Starting at the surface of the submerged object and moving upwards, the regions are: I) a rigid dead region, II) a rigid percolating

region, III) a non-rigid percolating region, IV) a weightless non-expanded and non-rigid region, and V) fully expanded and fluidized region. The term “rigid” is used here to indicate that the region being described can transmit an applied load to the submerged object. This will be discussed in more detail when buoyancy in a fluidized bed is discussed.

Using the results obtained from this study, Figure 53 and Figure 54 have been constructed outlining the different de-fluidization levels and their respective heights in the de – fluidized region of a disk and a sphere.

The arrows indicate the airflow re-entering the wake. The streamlines for air flow behind the disk will be similar in shape to the streamlines presented by Shenoy [2008] and Miyagi [1993] and for the sphere they will be similar in shape to those seen Figure 24 and Figure 25 for low Re flow around a sphere. The dead region shown in the figures encompasses both the dead region as well as the rigid percolating region. The expanding region is shown as a thin halo outlining the top of the percolating non-rigid region. Voids have been shown as empty circles along the periphery of the de-fluidized zone. The role of voids on the re-fluidization mechanism is critical and will be discussed in the subsequent sections.

Using visual inspection techniques alone, like those employed by previous researchers, the levels within the de-fluidized region cannot be determined. Throughout the wake, the particles will be in contact with each other and the entire wake will appear in a photograph to be uniform in de-fluidization intensity. However, the data collected for the present study, determines the change in fluidization regimes within the wake.

A deeper description of the de-fluidization levels within hood are given in the following sections.

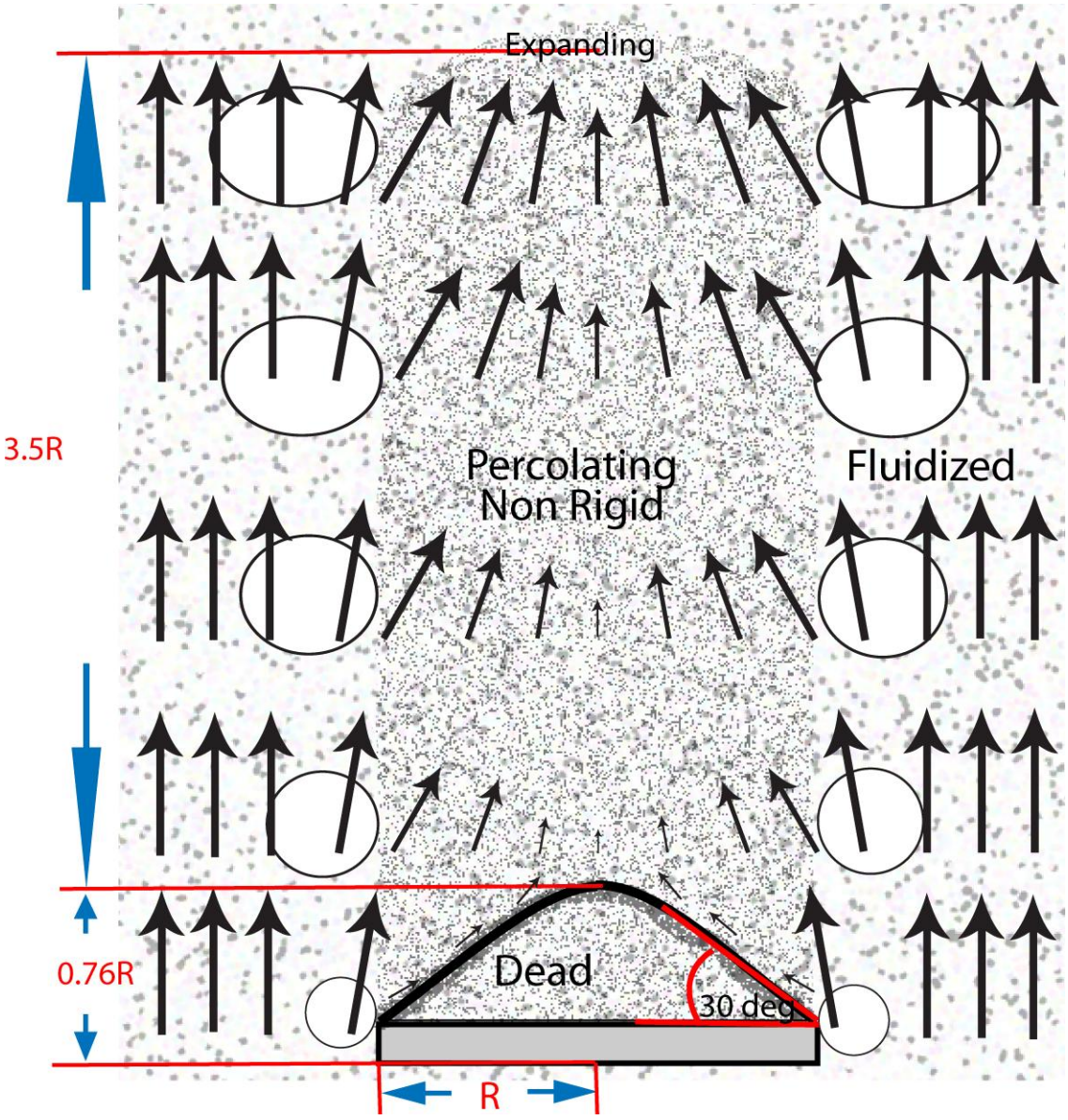

Figure 53: De-fluidized regions and streamlines within the wake of a disk

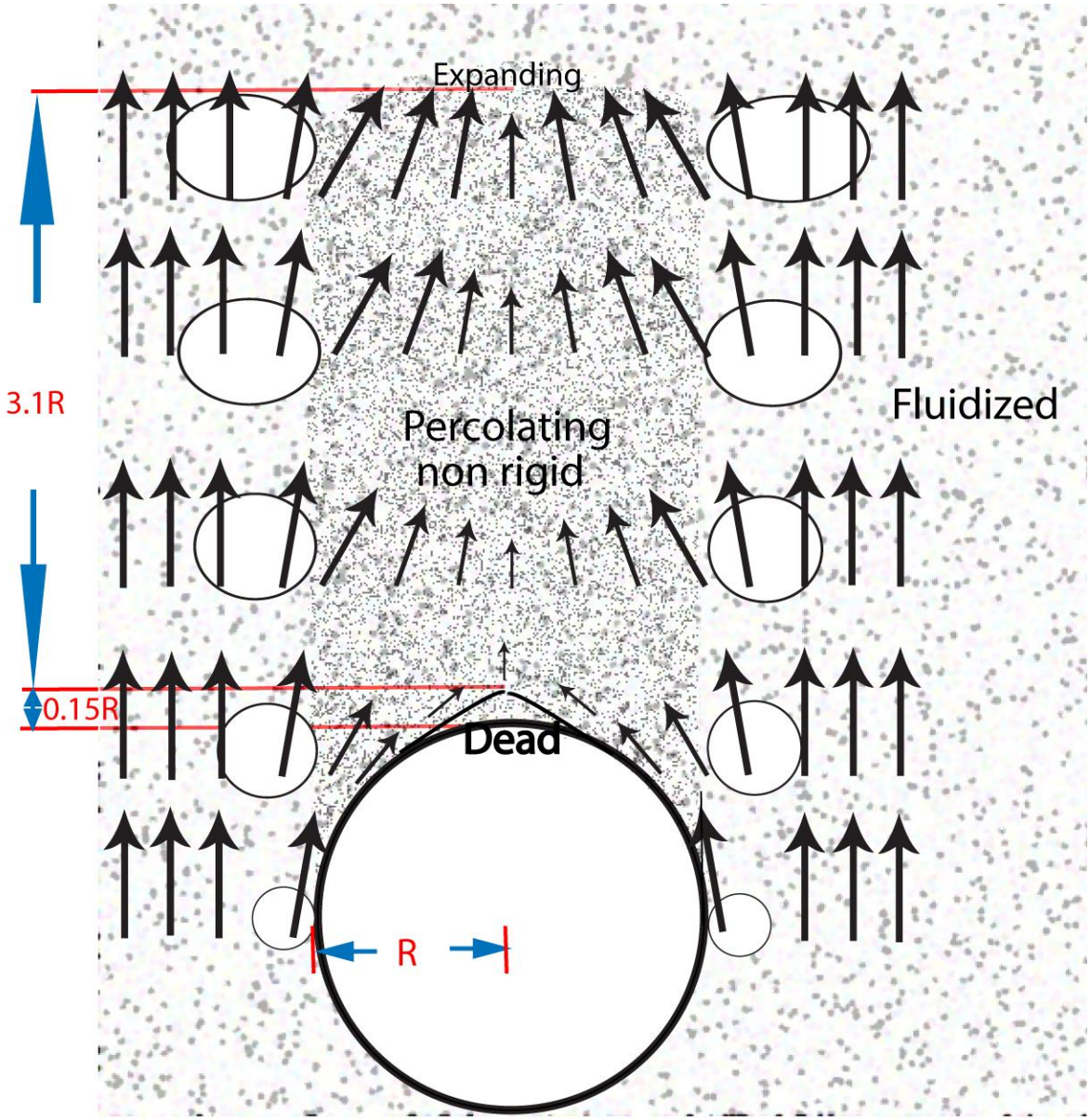

Figure 54: De-fluidized regions and streamlines within the wake of a sphere

5.2.1 Description of dead region in wake

Disc:

The findings of Shenoy [2008] and Miyagi [1983] indicate the at small Reynolds numbers the flow separates from the disk and that there is no air flow behind the disc (see Figure 27). While the flow around a disk in a single phase fluid will be different than the flow around a disk in a multiphase fluid, the streamlines are expected to be self-similar. Therefore, without any airflow, the region behind the disc should be dead.

The size of this dead region will be dictated by the angle of repose, discussed in section 1.3.3 Angle of repose. If the particles are piled on a flat surface, they will form a cone elevating to the angle of repose. Any dead region found on top of the obstruction will form in this same manner and will be cone-shaped with an angle equivalent to the angle of repose. Any additional particle accumulation leading to a greater angle than the angle of repose will result in the particles sliding off of the dead region until the stable slope attributed to the angle of repose is reached. Lab measurements conducted show that for the glass beads used in the present study, the angle of repose is 30^0 and for the Al_2O_3 particles the angle of repose is 33^0. It follows then that for a disk with a radius of R, the maximum height above the top of the disk surface to which a dead region of glass beads can rise will be 0.578R. With a disk thickness of 0.19R, the maximum height of the dead region as measured from the bottom of the disk would be 0.767R (as seen in Figure 53).

Experimental evidence confirms the presence of a dead region with a maximum height of 0.76R for the disk in a bed of glass beads. The results presented in section *4.4 Bed height collapse over a submerged objects* were aimed to determine the change in

surface height within the hood at different disk depths. Figure 55 shows the change in height of the bed directly over the center of the disk.

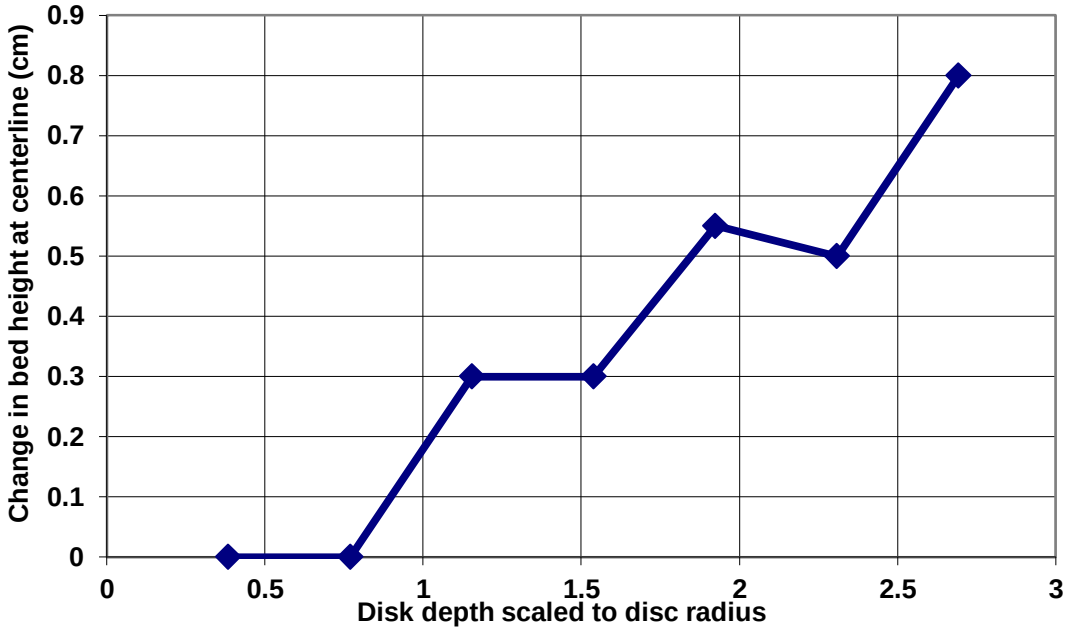

Figure 55: Change in bed height over the centerline of the submerged disc

Until 0.76R the centerline region shows no change in height. Moreover, no particle motion was observed in this region. This indicates that this region is completely dead.

Sphere:

In the case of the sphere, the completely dead region will be significantly smaller than that of a disk. The curvature of the sphere will not support a large dead region. The dead region will be no larger than 0.15R above the sphere surface as dictated by the angle of repose (see Figure 54).

5.2.2 Description of rigid percolating region

Disk:

If the airflow curves into the wake at an angle less than the angle of repose, there will be a region of stagnant percolating particles above the dead region. The particles will be stagnant because they have yet to form higher than the angle of repose and are therefore stable. With the addition of airflow, the angle of repose will be less, but this rigid percolating region will exist up to the maximum height dictated by the angle of repose. Beyond the angle of repose, the particles will slide off of the surface until the angle of repose is regained. Without any particle motion within this region, it will act as a rigid body in that an external force applied to this region will transmit to the disk without the shape of the region being deformed.

Sphere:

In the case of the sphere, the curvature of the sphere does not permit a large stagnant region of particles to "sit" on the top of the sphere. Therefore, like the dead region, if the rigid percolating region does exist in the hood of the sphere, it will be negligibly small.

5.2.3 Description of non-rigid percolating region and re-fluidization mechanism

The non-rigid percolating region will be the largest section within the wake for both objects. It will begin immediately after the dead and rigid percolating regions once the airflow has curved back into the wake behind the object.

Sphere:

Previous studies have modeled the entire wake as dead. However, as shown in Figure 52, the results herein suggest otherwise. Furthermore, the results from the experiments in section *4.2 Shear within the de-fluidized hood*, indicate the resisting force on the rod is strongest closest to a submerged sphere and decreases downstream from the sphere. A summary of the average shear at each depth is provided in Figure 56. It clearly shows a lower resistance force on the rod as measurements are taken further away from the sphere.

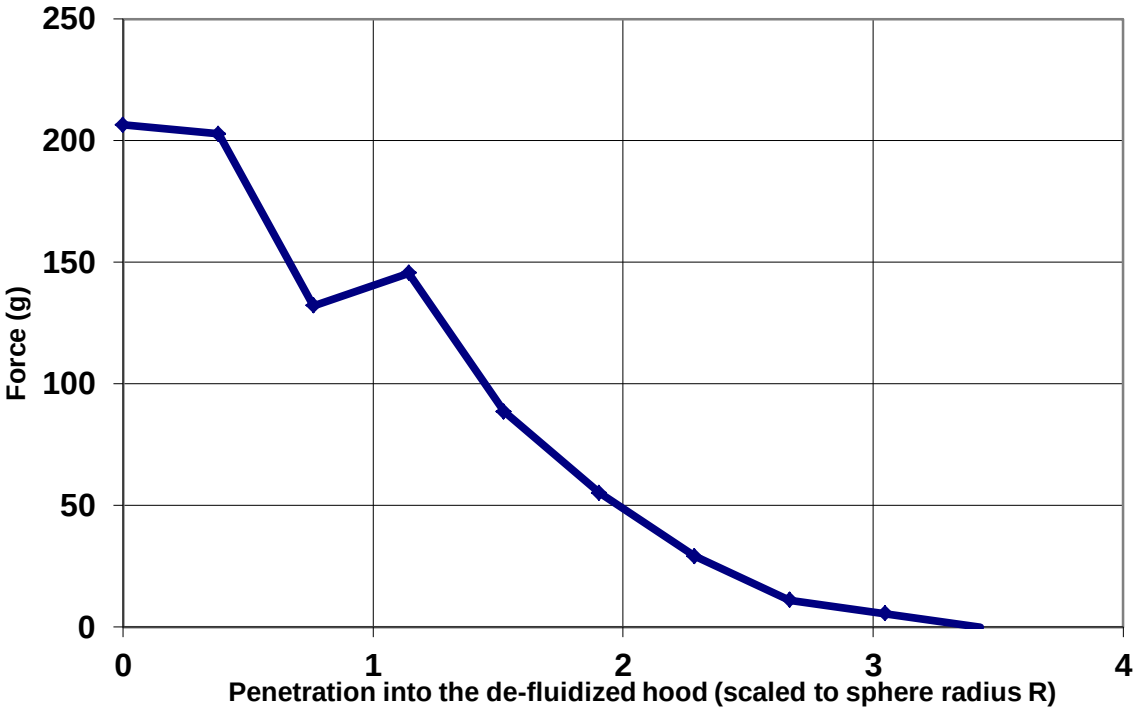

Figure 56: Force required for 8-32 rod to move through the de-fluidized hood at different depths

Tardos *et al* [1998] studied the shear imposed by a uniformly packed bed and found the shear to vary linearly with depth. The results in Figure 56 do not show a linear dependence between the shear and the depth. The non-linearity of the current results suggests that the de-fluidized region is not uniform in packing as is the case in Tardos *et al* [1998].

For the sphere, at 3.25R from the sphere surface (or 4.25R from the center of the sphere), the de-fluidized hood ceases to exhibit any shear, as seen in Figure 56. In the experiments measuring the force on the sphere as it was submerged, the hood height was also determined to be 4.25R away from the center of the sphere. Both experiments indicate a cessation of the de-fluidized hood at 4.25R from the center of the sphere.

The uptick in the force in in Figure 56, matches the observation of Albert *et al* [2001] as shown in Figure 22. It is hypothesized to be the transition from a periodic to a stepped behavior in the transmission of the force chains.

This non-uniform region will be non-rigid in that under an external load, the particles will move and the structure will deform to accommodate the force. Therefore, a load applied to this region will not transmit to the submerged object.

Disk:

For the disk, air is reintroduced past the dead region. Thus, the percolating non rigid region will exist in the wake of the disk as well.

Shape of the percolating non –rigid region for both objects

For both objects, visual inspection verifies that the shape of the percolating non-rigid region resembles a cylinder with a rounded top, as seen by Rees [2008]. Visual observation of the surface of the sphere as it is submerged in the bed shows voids outlining the perimeter of the de-fluidized region. This can be seen in the picture of the sphere of radius 0.03334 m submerged 4.1R deep in a bed of Al_2O_3 shown in Figure 57. The voids appear as ‘bubbles’ on the surface. This image shows the de-fluidized region,

the region within the void ring, to have the same radius as the submerged sphere. This region exhibited less particle activity and more surface features – such as ripples – than the surrounding fluidized medium.

Figure 57: Bed surface picture of sphere of radius 0.03334m submerged 4.1R in fluidized bed of Al_2O_3. Voids outline the perimeter of the submerged sphere.

The steep slope of the region's shape would not be feasible were it not for voids along the side of the de-fluidized region creating a physical separation between the un-fluidized and fluidized sections. As observed by several authors (Glass and Harrison 1964, Harrison 1971, Loew 1979, Duursma 1994, Rahman 2002, Umekawa 1999) voids form around submerged objects. The air flow, initially at U_{mf}, must accelerate around the submerged object as it passes and in doing so achieves a velocity greater than U_{mf}. This

causes voids to form which escape through the bed. The voids outline the perimeter of the submerged object indicating that the air flow separates from the object at the hemisphere for the sphere and at the side walls for the disk.

The particles within the de-fluidized region will flow out of the hood as the region tries to regain its stable shape as dictated by the angle of repose, but the presence of the voids prohibits sufficient air flow from entering from the outside into the wake. The space left by the exiting particles is filled by new particles supplied from the upper regions of the wake. This process is continually occurring and leads to a steep percolating structure. As discussed in the results from the bed collapse over a disk experiments, particle circulation was observed to cause a decrease in the surface level height above 0.76R. A similar finding concerning particle circulation was made by Hager and Schrag [1976] and captured in Figure 8. Furthermore, particle motion was shown by Loew [1979], where particles slide from the top surface of submerged objects as bubbling occurs.

The particle circulation plays an important role in the re-fluidization mechanism by inhibiting air flow into the wake. The particle motion out of the bottom of the wake will create an outward flux of material from the wake, thus counteracting any potential inward flux of air.

In spite of the hindrances presented by the voids and the particles, air will eventually re-enter the wake in this region. The air in the fluidized section will be traveling much faster than the air within the wake. This will cause a transfer of momentum across the boundary of the wake. Some of this momentum will be lost to the escaping voids, but some will accelerate the air in the wake. This will cause air flow to

curve back into the wake in order to maintain a continuity of mass. One can expect the air flow over the object to be similar to that shown in Figure 28 for a disk in a single phase fluid and Figure 24 for a sphere in a single phase fluid. The actual streamlines will differ in a fluidized bed due to the presence of the particles.

The top of the percolating structure will elevate to an angle smaller than the angle of repose because the airflow will reduce the sliding friction of the particles. Therefore, the top of the percolating region is gently rounded and not very steep at any location.

5.2.4 Description of the expanded/weightless region and the fully fluidized region

Between the percolating region and the fluidized region, there is a region in which the particles are no longer in contact with one another. The particles have separated, but they have not reached their maximum interstitial distance and are therefore not completely fluidized. The range of air flows over which this occurs is very small and for Geldart A particles, whose transition from percolating to bubbling occurs immediately, this region is very small. However, in a fluidized bed of non-Geldart A particles, one may expect to see a more significant weightless and expanding region beyond the percolating region.

Beyond the expanding region, the de-fluidized hood is completely fluidized and the submerged object no longer influences the flow field.

5.2.5 Graphic with particle circulation

An illustration of the particle circulation within the de-fluidized hood behind a disk is provided in Figure 58. The boundary below which particles exit the wake and

above which particles enter the wake has been theorized to correspond to the intersection of a cone with a 30^0 slope (corresponding to the angle of repose for glass beads) of the same volume as the de-fluidized hood with the de-fluidized hood.

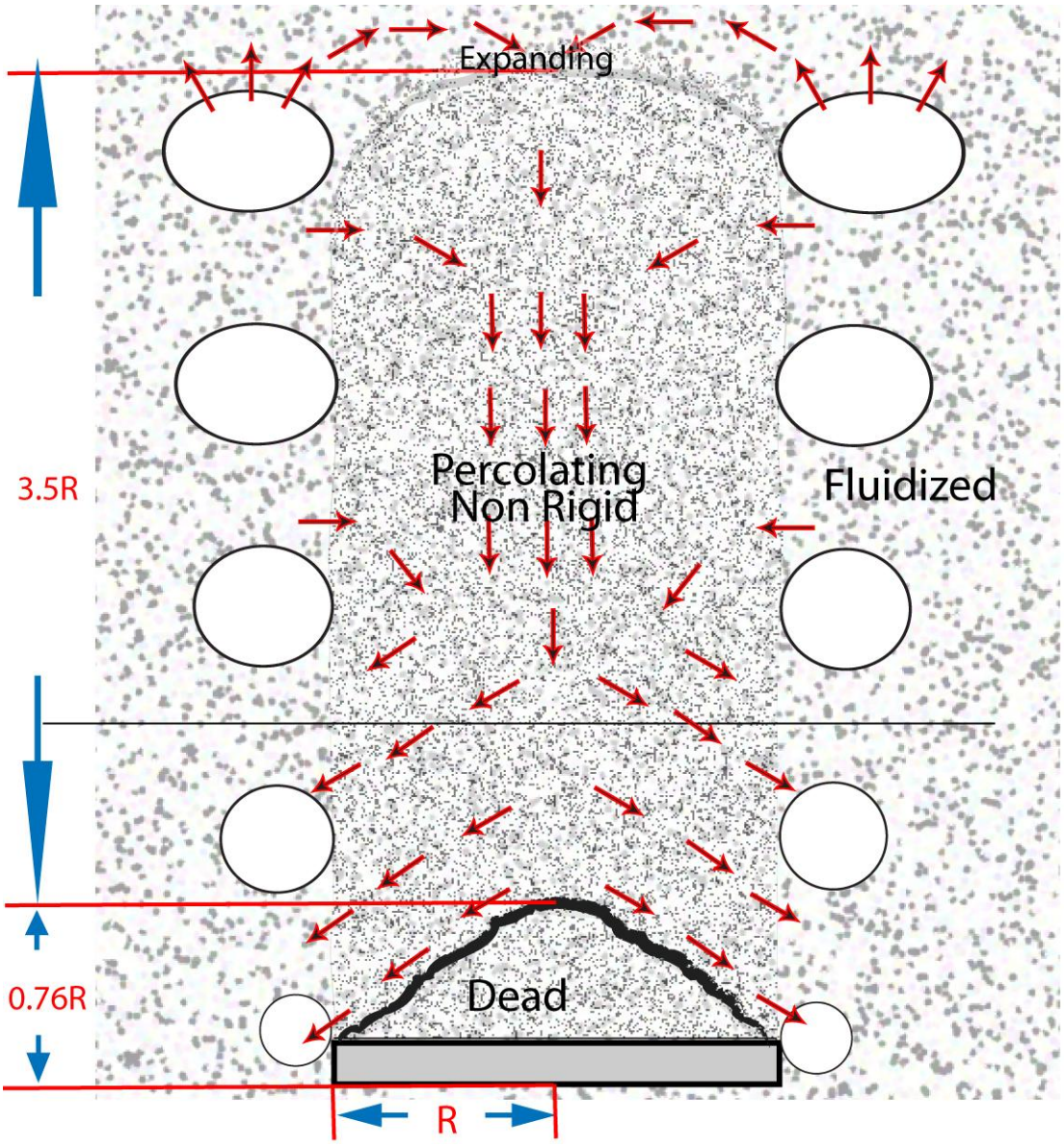

Figure 58: Particle flow in the wake behind a disk

Figure 59 shows the particle circulation in the de-fluidized region of the sphere. The location of the exiting particles has been determined in the same fashion used for the disk

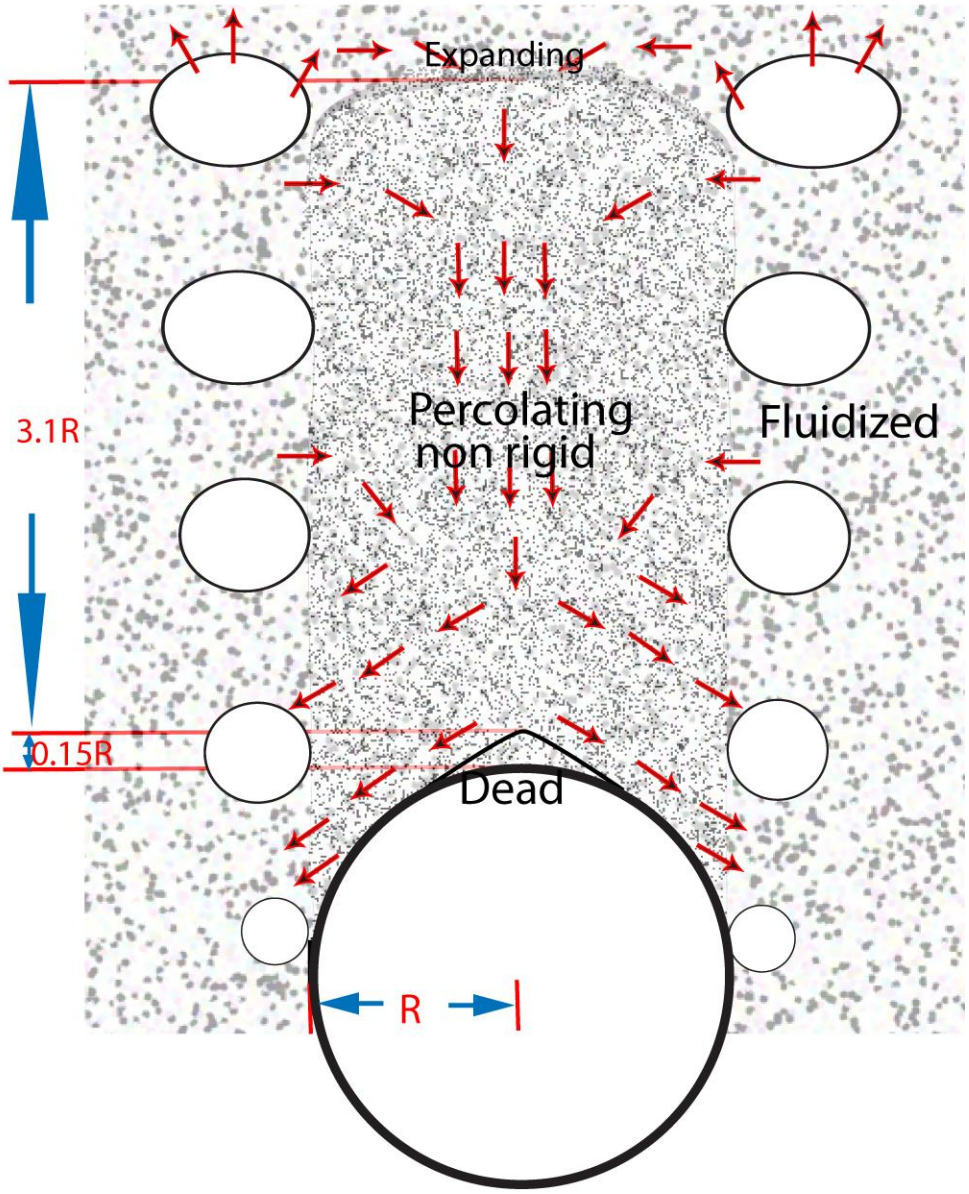

Figure 59: Particle flow in the wake behind a sphere

5.3 Model of force balance on submerged objects

With an understanding of the de-fluidization levels within the de-fluidized region, a model can be created which will predict the forces on submerged objects within a fluidized bed.

The force balance on a submerged object will be the balance in Equation 20.

$$\sum F_z = F_{D,a} + F_B - F_{D,p} - F_{dead} - F_{perc} - F_W$$

Equation 20

Where

F_z = the net force

$F_{D,a}$ = the force due to air drag

F_B = force due to the air pressure in the fluidized bed

$F_{D,p}$ = force due to the drag from the particles

F_{dead} = force due to the dead region

F_{perc} = force due to the percolating regions

F_w = force of weight of the object due to gravity

The weight of the actual object due to gravity was not reflected in the data collected because the sensors were zeroed to the object weight while outside of the fluidized bed. The drag forces imparted by the air will be ignored since it will be negligibly small by the arguments made by Nguyen and Grace [1978]. Finally, the drag force due to sliding particles will be initially assumed to be negligibly small. This assumption will be validated upon presentation of the force model for the sphere.

5.3.1 Model of force balance on a disk

Disk:

As a flat disc is submerged into a fluidized bed, it experiences the expected pressure force due to the air, but it also experiences an extra weight due to the de-fluidized particles.

F_{dead}: Force due to dead particles

The angle of repose of the glass media was found to be 30^0, indicating that glass beads could not form a slope steeper than 30^0 when formed into a pile. With this angle determined, the size of any dead region above the submerged disk would be a cone with a radius equivalent to the radius of the disc (R) and a height 0.76R measured from the bottom of the disk. Therefore, the maximum load on the disc from the dead region is found using Equation 21.

$$F_{dead} = \rho g V_{dead}$$

Equation 21

Where

ρ = particle packed density, kg/m^3

g = acceleration on particles, m/s^2

V_{dead} = volume of a 30^0 with base 2R, m^3

This force will begin right when the disk is fully submerged and cease once the disk is 0.76R below the bed surface.

F_{perc}: Force due to percolating regions

The force due to the percolating region can be found using the same relation as Equation 21. However, the volume is no longer a cone but the de-fluidized region resembles a cylinder with a rounded top. The rounding of the top will be at an angle less than 30^0 since this is the maximum angle of repose for dead particles.

Within this region, the particles weigh effectively less downstream in the wake because the increased air flow counteracts the weight of the particle itself, as described in *Appendix B.2 Force balance on a section of particles*. This effect is captured by making the acceleration on a particle in the percolating region, *g*, a function of z and r.

Using the results presented herein, a relation for acceleration on the particles in the percolating region behind a submerged object has been proposed and is shown in Equation 22.

$$g\ z,r\ = -9.8(A \times [1 - \frac{z}{h_{hood}}]^m) \times [1 + \frac{r}{r_{object}}]^n$$

Equation 22

Where, h_{hood} is the height of the de-fluidized region, z is measured from the object surface, r_{object} is the radius of the object, r is the position radially along the object and A is a constant accounting for the object geometry. Using values of A= 0.61, m = 0.53, and n = 4 provided an excellent fit for the force data in the percolating region

F_B: Pressure force on disc

The pressure force on the disc is due to the air pressure within the fluidized bed. The pressure drop through the fluidized bed was measured and found to be:

$$\frac{dP}{dz} = 9935\ \frac{\frac{N}{m^2}}{m}$$

The force due to this pressure acting on an object is found using Equation 23

$$F_B = \frac{dP}{dz} \times h \times SA$$

Equation 23

Where,

dP/dz = pressure gradient in fluidized bed, Pa/m

h = depth of submersion, m

SA = surface area, m^2

It is important to note that the pressure gradient in a fluidized bed will be due to the resistance to air flow due to the particle packing of the medium. This is not the same as the pressure gradient in a static single phase fluid in which it is due to the hydrostatic pressure.

The surface area for calculating the force from below due to the pressure force is the area of the disk. The surface area used for calculating the force due to the air pressure from above will be different, and the surface area used will be that of the dead region sitting on the disk. The pressure force due to air will act upon solid bodies within the flow. Since the dead region is rigid, it can be treated as a solid body within the flow. Therefore, air pressure acts upon this geometry.

Results:

The relations for F_B, F_{dead} and F_{perc} are inserted into Equation 20. Further descriptions of the forces acting on a submerged body can be found in *Appendix B: Force balances on objects in a fluidized bed*. The net force on the disk is the summation of the above loads. The resulting model is compared to the data and can be seen in the Figure 60.

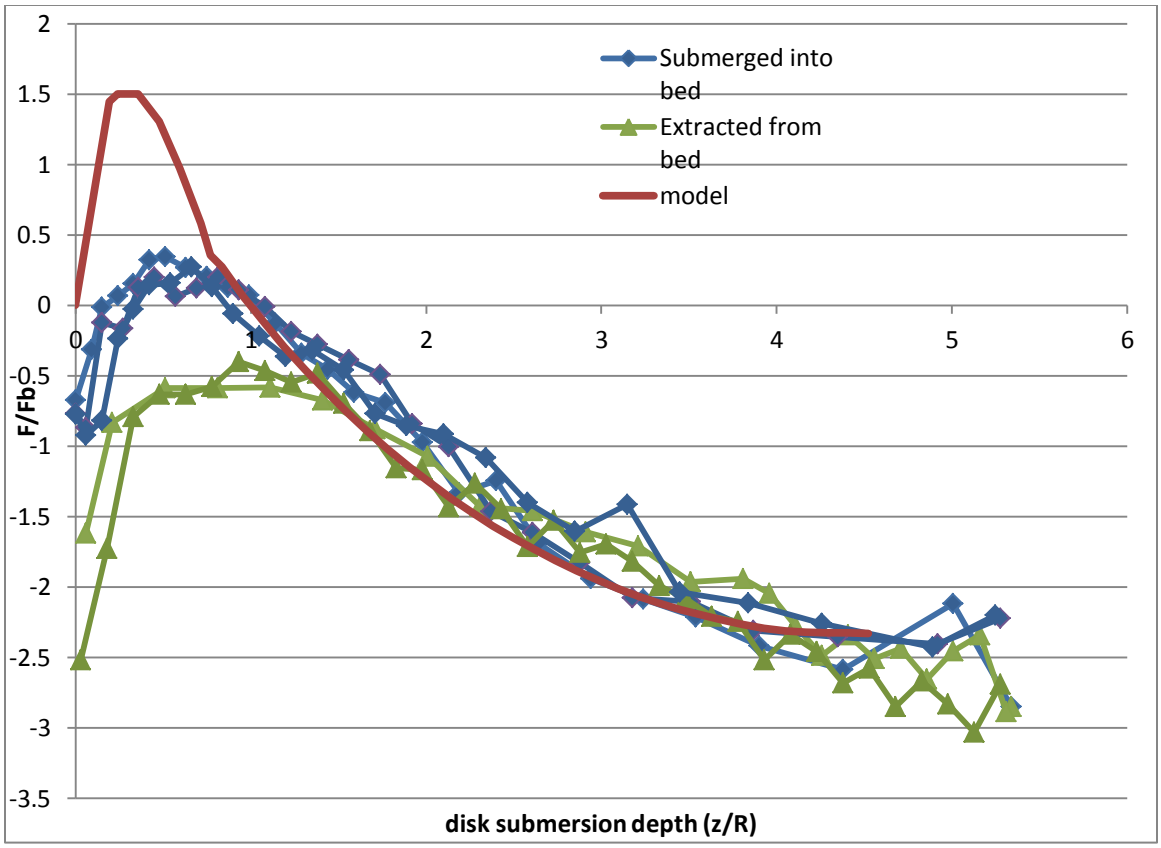

Figure 60: Model of forces on a submerged disk in a fluidized bed compared to experimental values

Differences between the model and the data:

The first data point is taken with the disk out of the bed. The force should be 0 N as the disk experiences none of the above forces. The experimental force, however, is not 0 N. Particles from exploding voids splash on top of the disk creating a load on the disk even before it is submerged. This effect is not modeled since it is an effect of the voids rather than an effect of the wake. This splashing effect continues to add particles to the disk in excess of the model's prediction until the disk is submerged deep enough such that the dead region is completely formed. This occurs at 0.76R. Beyond 0.76R, the particles splashed by the voids will become part of the particle circulation within the hood and slide off the disk. The model and the data agree beginning at 0.76R.

Validation of percolating region fit with other experimental results:

The acceleration of the particles in the percolating region, g(z,r) in Equation 22, was found to vary with r^4 and $z^{0.53}$. As shown in *Appendix B.2 Force balance on a section of particles*, the force exerted by the particles on a body is dependent on the drag on the particles. It therefore varies with the velocity, U, by U^2. Since the force in percolating region varies with r^4 and $z^{0.53}$, it can be extended that the velocity will vary with r^2 and $z^{0.71}$.

The data corresponding to the experiments in section *4.5 Normal force exerted by the de-fluidized hood* provides lines of constant normal force within the hood. As discussed in that section, each line of constant normal force in Figure 51 will correspond to a velocity. Therefore, the results from the experiment provide lines of constant air velocity within the de-fluidized hood. Comparing this data with a modeled flow varying with r^2 and $z^{0.71}$ shows good agreement between the data and the theorized relationship for the air velocity within the de-fluidized region. The comparison is shown in Figure 61. The velocities have been scaled to the minimum fluidization velocity (U_{mf}), and both the x- and the y-axis have been scaled to the radius of the disk.

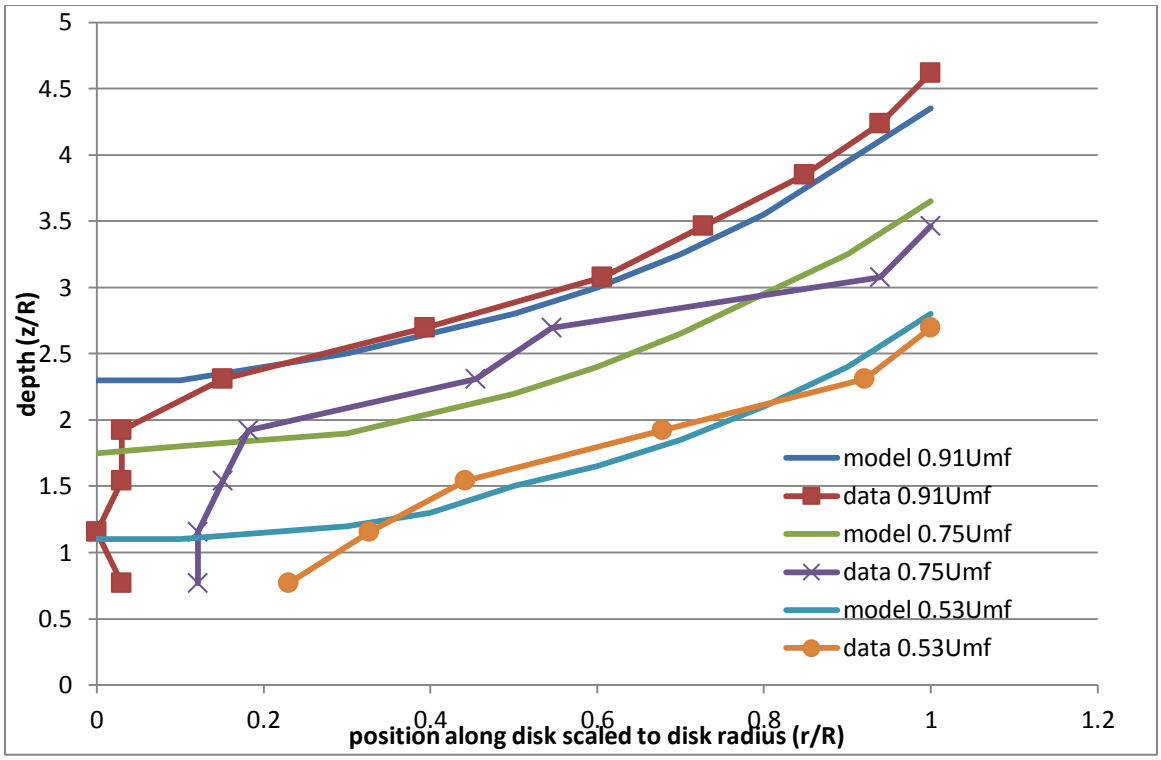

Figure 61: Experimental data for air velocity within de-fluidized region compared to modeled flow

The relationship used in Figure 61 is given in Equation 24. This relationship is used for verifying the relationship developed for the force in the percolating region in the de-fluidized region behind a disk.

$$U\ r,z\ \sim -r^2 + Cz^{0.71}$$

Equation 24

Where

U = air velocity

r = radial position

z = height above disk

C = coefficient, 0.5

Regarding the velocity gradient moving away from the submerged object, the velocity in the z-direction is found to vary with $\sim z^{0.5}$. This would indicate a slow approach to the free-stream velocity. The findings of Shenoy [2008] suggest the wake at Re = 10 behind a disk to be approximately one diameter in length (Figure 29). In the current case, the wake is more than twice this length. Therefore, the air flow takes a longer time to re-enter the wake in a multiphase flow than it does in a single phase flow. Particle exit from the percolating region as well as the presence of voids will inhibit the re-entry of air flow into the de-fluidized region. This will lead to a larger wake than in a single phase fluid.

5.3.2 Model of force balance on a sphere

Sphere:

The regions within the wake of the sphere will be the same as those found behind the disk. Predictions for the forces due to the regions will be similar, but some difference will exist.

F_{Dead}: Force due to dead region

The force due to the dead region can be calculated using Equation 21. The volume will be much smaller. It will be the volume of a cone circumscribing a sphere. The cone will begin at the position along the sphere corresponding to the angle from the top of the sphere equivalent to the angle of repose. A diagram is provided in Figure 62 for illustration where θ is the angle of repose.

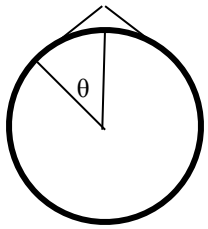

Figure 62: Reference for dead volume behind sphere

F_{perc}: Force due to percolating region

The force due to the percolating region can be calculated using Equation 21 and by applying the same relation found in Equation 22, with m = 0.53, n = 4, but using A = 0.53

F_B: Pressure force on sphere

When determining the pressure forces on the submerged object, only the vertical components of the pressure force need to be considered because any horizontal component will cancel due to symmetry. Also, considering the dead and percolating region are relatively small, the only body about which the pressure force acts can be considered to be the sphere itself.

Results:

The relations for F_B, F_{dead} and F_{perc} for the sphere are inserted into Equation 20. The resulting model is compared with the data in Figure 63.

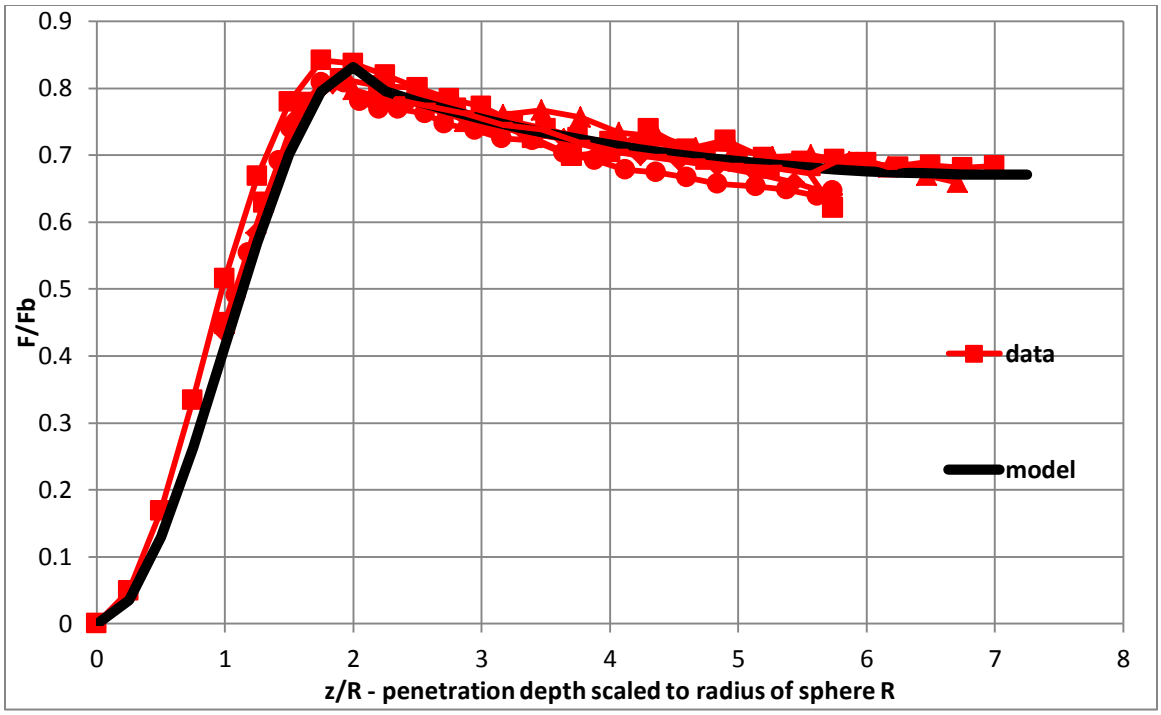

Figure 63: Comparison of force on a sphere of radius 0.03334m in glass beads with model

Validation of assumption of negligible contribution from drag force due to particles:

While the sphere is partially submerged, the force is predicted well by the pressure force on the sphere. This validates the assumption that a drag force imparted by the particles to the surface of the submerged object is negligibly small.

5.3.3 Comparison between disk and sphere model

As discussed, the dead region behind the disk will be significantly larger than the dead region above the sphere owing to the inability of the sphere to support a dead region due to the curvature of the surface. The dead region will rise 0.57R above the disk top surface and 0.15R above the sphere surface.

However, the percolating regions show a similarity in their dependence on the spatial variables r and z, with the force in the both percolating regions varying with r^4 and $z^{0.53}$. This suggests that there is commonality in the re-fluidization and wake air velocity

re-entry for the two obstructions. Moreover, past the point of separation, the two objects will similar size wakes. This finding is supported by a comparison of the total volume of the area impacted by the de-fluidized region.

Table 6 compares the geometries of each of the regions within the de-fluidized hoods for both objects. The final column compares the total volumes of the areas impacted by the de-fluidized zone. The impacted area is any area within the wake past the air flow separation point. For the sphere this is at the hemisphere and for the disk this is at the side walls. Therefore, the impacted area for both objects includes the back half of the object plus the de-fluidized wake. The total impacted volumes are within 2% of each other.

	Height of dead region above object centerline	Height of percolating region above dead region	Total height of de-fluidized region above object centerline	Total volume of region impacted by wake (m^3)
Disk	0.672R	3.87R	4.15R	$4.83x10^{-3}$
Sphere	1.15R	3.1R	4.25R	$4.95x10^{-3}$

Table 6: Geometric comparisons of regions impacted by de-fluidized wake

Once the air flow separates, the two driving mechanisms inhibiting air re-entry and subsequent re-fluidization are the presence of the voids and the particle circulation within the wake. Both of these phenomena occur for the disk and the sphere. This will lead to similar impacted volumes once separation has occurred.

5.3.4 Findings on buoyancy of a submerged object in a porous medium

In single phase studies, the buoyant force is due to a difference in hydrostatic pressure above and below a fully submerged rigid object. When calculating the pressure force experienced by a disk submerged in a tank of water, the pressure can be integrated about the surface of the disk. In the current study, the buoyant force cannot be calculated in the same manner because the de-fluidized section adds a mass and a volume to the object. There is potential for this additional volume to also be impacted by the pressure forces.

For an object with a rigid dead section, such as a disk, the pressure forces will act on the rigid surface. While the entire de-fluidized section will experience a force due to the pressure gradient, the ability for the percolating region to support a load will decrease as the region re-fluidizes. If the force due to the pressure gradient across the particle is greater than the load which can be supported by the particle, then the particle will not transmit to the disk, but will instead yield and move. The dead region, however, is rigid and the particles can support a larger load than those in the percolating region. Therefore, the pressure force acting on the dead region will transmit to the disk. Thus, it is theorized that for a disk, the dead region should be considered as part of the object volume when considering the buoyancy of a submerged object in a fluidized bed. The case for the sphere is simpler since the dead region is significantly smaller. For a sphere, the pressure can be approximated to act only about the sphere surface.

The increased buoyant area explains one key feature of the force data – the “s”-shaped curve observed immediately after the disk is submerged. In this curved region, the weight of the dead particles serves to lower the net force on the disk. Acting alone, this

increased weight would create a sharp downturn in the force data (as seen in Figure 52 for the model of a sphere with the wake being entirely dead). However, since the rigid body is still experiencing upward loading due to the air pressure, the severity of the increased weight load is lessened creating the "s"-shaped curve observed in the data. Once the dead region is fully submerged (at a depth of 0.76R), the buoyant force no longer increases but reaches its steady value. At depths past 0.76R, the force data follows the relation determined in Equation 23.

5.5 Ramifications on heat exchanger tubes

The dead region and the percolating region will lead to less particle turnover in the de-fluidized hood of the submerged object as compared to other regions around the object, such as the sides. This will have an effect on the performance of the submerged objects within a fluidized bed such as a heat exchanger tubes.

5.5.1 Reduced heat and mass transfer

As stated by several authors (Kim 2002, Molerus 1995, Kurusaki 1988, Peeler and Whitehead 1982) the particles within a fluidized bed are the heat carriers, meaning that particles transfer heat to the heat exchanger tubes within the bed. The rate of heat transfer to the tube will be dependent upon many variables. As Howard [1989] states in identifying the key parameters effecting particle-surface heat transfer, small densely packed particles with high heat capacities that are replaced frequently in a gas with a high thermal conductivity will exhibit the best heat transfer. Small and dense particles will allow for more particle-surface contact area, while a high heat capacity will allow the particles to maintain a high temperature while in contact with the colder tube. High particle replacement rates will also allow for more hot particles to come in contact with

the tube. A highly thermal conductive gas will allow for more of the particles heat to be transferred to the tube.

The most commonly used method for calculating the heat transfer from a surface is to employ the "packet" or "cluster" model. This model states that there are three forms of heat transfer to a surface – convection from the surrounding gas, conduction from particle packets coming in contact with the surface, and radiation. For small particles (<100 μm) and low temperatures (<800^{0}C), the conduction from particle packets is the dominant form of heat transfer. This term is called "particle-convection" in that it is dependent upon the movement of the particles through the bed. As a particle comes in contact with a surface – i.e. either a tube or another particle - there is conduction between the particle and the surface and conduction through the air gap between the particle and the surface. In cases of a round particle on the surface of a round object, even though air is a poor conductor of heat, the contact area between the particle and the surface would be very small and conduction through the air gap would dominate the heat transfer. Once the bed reaches U_{mf} and reaches incipient fluidization, the particles will separate. This will increase the air gaps between the particles and surfaces. Without any mixing of the particles, the increased separation would serve to lower the overall heat transfer. However, once mixing occurs, the surface of interest will be in contact with new particles. These new particles will be hotter than a particle that was in contact with the surface for a long period of time. Therefore, the temperature difference between the particle and the surface in a mixed bed would be higher than the temperature difference between the particle and the surface in a non-mixed bed.

Gelperin and Einstein [1971] provide a summary of the method for predicting the overall heat transfer coefficient in a small particle, low temperature medium using the 'packet' model. The heat transfer coefficient, h, in this case is estimated as:

$$h \cong \ 1 - f_0 \ h_a$$

Equation 25

Where f_0 is the fraction of heat transfer surface occupied by bubbles and h_a is the particle convective heat transfer coefficient. Howard [1989] gives an expression for the maximum h_a as:

$$h_{a,max} = 35.8\rho_p^{0.2} k_f^{0.6} d_p^{-0.36}$$

Equation 26

Where ρ_p is the particle density, k_f is the thermal conductivity of the gas, and d_p is the particle diameter. Howard recommends using 70% of the $h_{a,max}$ in order to account for variations in fluidization velocity and void activity.

A simple method of finding f_0 is presented by Gelperin and Einstein [1971] where

$$f_0 = 1 - \frac{bed\ height\ at\ fluidization\ velocity}{bed\ height\ at\ minimum\ fluidization\ velocity}$$

The overall heat transfer coefficient, h, will fluctuate over time and the time averaged h, $\overline{h}$, can be found by integrating over the mean contact time between the particles and the surface t_m

$$\overline{h} = \frac{1 - f_0}{t_m} \int_0^{t_m} h_a dt$$

Equation 27

The packet method assumes uniform bed properties around the tube. The findings presented here suggest that the region above a tube as far away as 6.15R from the center

of a round tube in a ground particle bed and a surface area swept by the angle of repose will exhibit different characteristics than the rest of the bed. First, the region will have a higher particle packing density than its surroundings, with the density in the hood being that of the packed bed. This will serve to create smaller air gaps in the hood compared to the air gaps in the surrounding medium. Second, for a bed operating at U_{mf}, the region around the tube occupied by the dead region will not experience any voids. Therefore, the total area of the tube contacting a particle in this region will be higher than elsewhere along the tube. However, the de-fluidized region will also feature less particle replacement than the surrounding medium.

In determining the effect of the hood on the heat transfer to a heat exchanger tube, it is important to delineate between a mixed bed and a non-mixed bed. In a non-mixed bed, where particles are separated but not moving, the heat transfer from the hood should be higher because the air gaps are smaller in the hood than they are in the surrounding medium. However, if the particles in the surrounding medium are fluidized and mixing, than the hood will see less heat transfer because the other regions in the tube are in contact with hotter particles. If the velocity is increased even further, where there is frequent bubbling, not only will the gas convective heat transfer begin to play a larger role, but the hood will be continually be replenished thus effectively defeating the hood. The application for which the fluidized bed is being is used is very important to consider. In some applications, particle carry out from the bed is minimized – drug coating, powder drying. In these applications, mixing will be kept to a minimum and the de-fluidized region may in effect aid in overall process efficiency. However, in cases such as those

using a circulating fluidized bed where carry out occurs, the de-fluidized hood, if it still exists, will lower heat transfer rates.

5.5.2 Increased loading on heat exchanger tubes

As seen in the results presented herein, the de-fluidized region will add an extra load to any internal structure. This extra mass will add stress to the internal structure and could lower its lifespan.

For scale up of a fluidized bed for larger applications, the weight force of the de-fluidized region should be considered when calculating the stress on the internal structures as the hood will scale with the size of the structure. Materials and proper supports for the internal structures should be selected with knowledge of this additional mass.

The findings from this work show that a rounded object is less impacted by the hood weight than a blunt object such as a disk. The findings suggest that for a spherical object, the load due to the de-fluidized hood can be as much as half the buoyant force on the submerged object. The load on a blunt object like a disk can be as much as 3.55 times the buoyant force.

5.5.4 Orientation of heat exchanger tube banks

Rarely will a fluidized bed have only one heat exchanger tube submerged within it, but it will have several. The experiments from *4.3 Drag on a spherical probe within the de-fluidized hood* provide evidence that at a distance of 2.5R away from the top of a submerged tube bank in a round particle fluidized bed, the air velocity will recover enough to support fluidization once again. Therefore, heat exchanger banks with tubes oriented less than 2.5R away from the top of another can expect to have their

performance influenced by the surrounding tubes. If located in the de-fluidized region of a neighboring tube, the surface of a heat exchanger tube in a tube bank can experience more contact with particles, but the particles in contact will not replenish as quickly compared to a single tube.

Appendix A: Determination of U_{mf}

The minimum fluidization velocity was determining by measuring the bed height rise as the air flow to the bed was increased. To measure the bed height, a photodiode connected to a PC and analyzed through LabVIEW was inserted into the bed. The sensor was installed in a plexiglass case measuring 13.5 cm x 4.5 cm x 2.5 cm and connected to a long aluminum threaded rod that could screw into the top of the bed. The diode was placed such that it was partially submerged in the fluidized bed and slightly offset from the wall radially. Voltage potentials could be measured at each end of the diode and a voltage drop could be measured across the diode and outputted in LabVIEW.

The diode was divided into two regions – the top half and the bottom half. Shadows on one end would reduce the potential observed on that same end. A 250 W light bulb was used as a strong light source to increase the amplitudes of the observed voltage drops. The light was installed on a fixture that could also be screwed onto the top of the bed. The diode was essentially a photovoltaic and therefore a decrease in exposed light would decrease the potential on the side that was being covered. Thus, as more of the diode was covered up, the voltage difference between the two ends would change.

Bed pressure was logged using an Omegadyne 0-5 psi pressure transducer. The pressure outputted to the same PC and the data could be read through LabVIEW. The pressure transducer was powered by an external 0-25 V power supply.

The bed was initially at rest. Air flow was slowly introduced to the bed, with the photodiode recording the bed height and the pressure transducer recording the pressure. The flow rate was increased until the bed was violently bubbling. The experiment was

conducted with both Al_2O_3 and glass beads. Results from the experiment are shown in Figure 64

The alumina oxide fluidized at 0.79 psi while the glass beads fluidized at 0.86 psi. This corresponds to an air velocity of 0.0100 m/sec for the alumina oxide and 0.0106 m/sec for the glass beads.

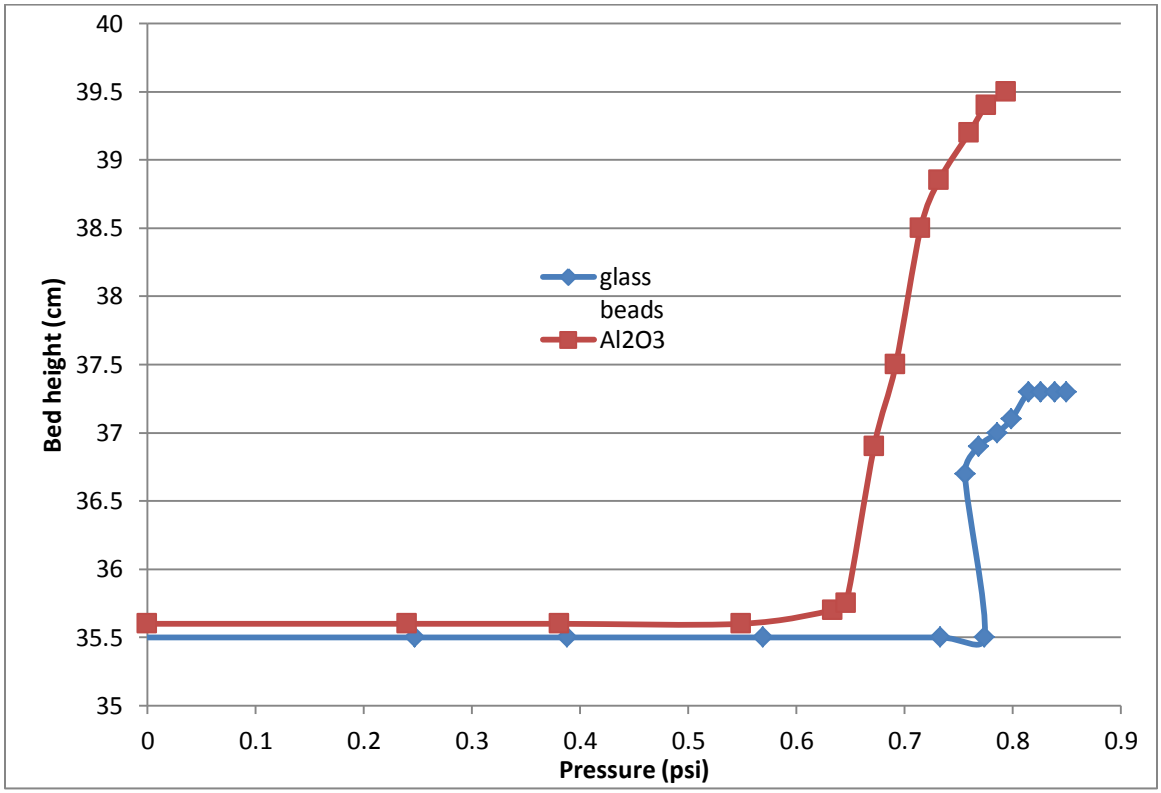

Figure 64: Bed height rise with pressure for alumina oxide and glass beads

Appendix B: Force balances on objects in a fluidized bed

The following appendix will: 1) develop a force balance on a submerged object within a fluidized bed and 2) a force balance on a section of particles within a fluidized bed.

B.1 Forces on large submerged bodies

A force balance on the submerged object must be determined before the impact of the de-fluidized hood can be resolved.

The possible forces on a sphere submerged in a fluidized bed are described in the free body diagram in Figure 65 followed by a description of each force. The force balance on the disk will be the same as it is on a sphere.

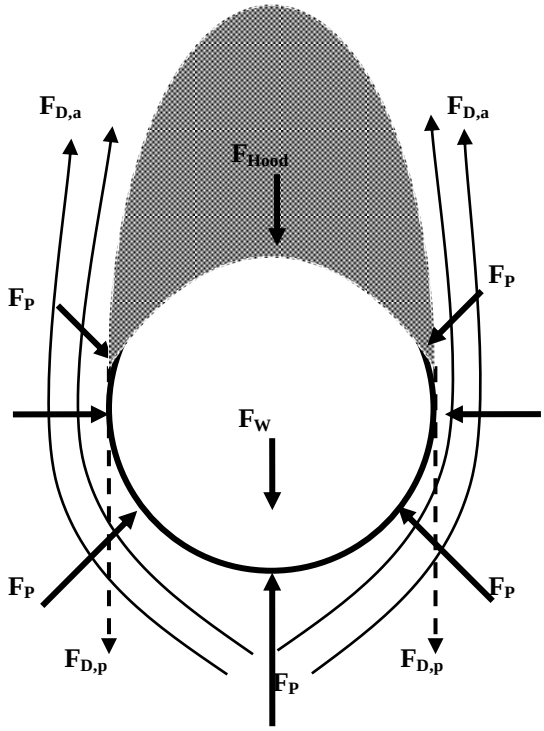

Figure 65: Force balance on a submerged sphere within a fluidized bed

B.1.1 Drag Force of air, $F_{D,a}$:

The drag force, $F_{D,a}$ due to air can be expressed as:

$$F_{D,a} = \frac{1}{2} C_D \rho_f U^2 A$$

Equation 28

Where,

C_D = drag coefficient, determined experimentally

ρ_f = density of air

U = velocity of air

A = surface area

For the experiments run, the air velocity was the minimum fluidization velocity. This velocity is essentially the terminal velocity of a particle in the medium. The submerged objects used in the present study were at approximately 900 times greater in diameter than the fluidizing medium. Therefore, the drag force due to air is not expected to be a significant component of the force balance on the submerged objects. This conclusion was also reached by Nguyen and Grace [1978].

B.1.2 Pressure Force, F_P:

The pressure force is the force due to the air pressure at the upper surface of the object being less than the air pressure at the lower surface. The force on the sphere due to the air pressure gradient can be found by the following relation:

$$F_P = \left(\frac{dP}{dz} hA \right) \cos(\theta)$$

Equation 29

Where,

dP/dz = pressure gradient in fluidized bed, Pa/m

h = depth of submersion, m

A = surface area of submerged object, m^2

θ = angle denoted in Figure 51

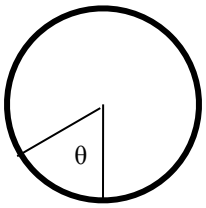

Figure 66: Definition of θ used in equation

The cosine (θ) term is included in order to isolate the vertical component of the pressure force.

It is important to note that the pressure gradient in a fluidized bed will be due to the resistance in air flow due to the particle packing of the medium. This is not the same as the pressure gradient in a static single phase fluid in which it is due to the hydrostatic pressure.

B.1.3 Drag Force of Particles colliding with the object, $F_{D,p}$:

The no slip boundary condition applies to the surface of the submerged object. As a result, particles within this region are not fluidized and are moving downward. The particles impart a frictional force against the surface of the submerged object. This is assumed to be negligible.

B.1.4 Weight force, F_W:

The submerged object has a gravitational weight force associated with the object itself. This is the weight of the object if placed on a scale outside of the fluidized bed. In all experiments, the weight of the actual object is constant.

B.1.5 Weight force of the de-fluidized region, F_{hood}:

The velocity deficit above the submerged object prevents the particles in this region from fluidizing. Consequently, weight force of the particles in the de-fluidized region is not balanced by the drag imparted by the, as they would be under fluidization. Furthermore, if the particles are not fluidized, then they are in contact with each other. Therefore, the particles contribute a downward force onto the submerged object.

The magnitude of this force can be expressed as:

$$F_{hood} = \rho g V$$

Equation 30

Where,

ρ = particle packed density, kg/m^3

g = acceleration on particles, m/s^2

V = volume of the de-fluidized region, m^3

The gravitational acceleration would equal 9.8 m/s^2 for the completely de-fluidized case and 0 m/s^2 for the completely fluidized case. Furthermore, ρ, the bed density, would equal the packed density for the dead and percolating cases and the fluidized density for the completely fluidized case.

The overall force balance on the submerged object is:

$$\sum F_z = F_{D,a} + F_p - F_{D,p} - F_{hood} - F_w$$

Equation 31

B.2 Force balance on a section of particles

Fluidization occurs when the weight of the particle is matched by its upward drag and buoyancy. The minimum fluidization velocity is in effect the terminal velocity of the particle.

The upward drag force on the particle can be found using Equation 32 [Batchelor 1988]

$$F_D = -2\pi a^2 \rho_f U|U|C_D$$

Equation 32

Where,

a = the radius of the particle

ρ_f = the density of the air

U = local air velocity

C_D = drag coefficient

The drag coefficient is dependent on the Reynolds number, defined as:

$$\mathrm{Re} = \frac{2a|U|\rho_f}{\mu}$$

Equation 33

If the particles are small, than $C_D \sim \mathrm{Re}^{-1}$ [Batchelor 1988]. If the particles are large, inertial forces will dominate the viscous forces, making the drag force inconsequential.

The weight of the particle and the buoyant effect is combined and found using Equation 34.

$$F_W = \frac{4}{3}\pi a^3(\rho_p - \rho_f)g$$

Equation 34

Where,

ρ_p = density of the particle

g = gravitational acceleration

In Rao 2009, it was shown that Equation 34 could be written as

$$F_w = \frac{\partial P}{\partial z}V$$

Equation 35

The normal force, F_N, exerted by the particles in the bed at a specific velocity would be:

$$F_n = F_D - F_W$$

Equation 36

Using the relations in Equation 32 and Equation 33, Equation 36 becomes:

$$F_n = -2\pi a^2 \rho_f U|U|C_D - \frac{4}{3}\pi a^3(\rho_p - \rho_f)g$$

Equation 37

At fluidization, the weight force balances the drag force, and the terminal velocity can be solved as:

$$U_T = \sqrt{\frac{2gr(\rho_p - \rho_f)}{3C_D\rho_f}}$$

Equation 38

Where,

U_T = terminal velocity of a particle

Using the relation that $C_D \sim Re^{-1}$, the above relation for the terminal velocity becomes:

$$U_T = \frac{gd^2(\rho_p - \rho_f)}{6\mu}$$

Equation 39

Where,

d = diameter of the particle

Geldart [1973] gave a more precise relation for the minimum fluidization velocity (Equation 40).

$$U_{MF} = \frac{8\times10^{-4} g d_{SV}^2 (\rho_p - \rho_f)}{\mu}$$

Equation 40

Where,

U_{MF} = minimum fluidization velocity

d_{SV} = surface area / volume of particle

The terminal velocity developed in Equation 39 is for a single particle, whereas the terminal velocity presented by Geldart [1973] in Equation 24 is for a cluster of particles.

Nomenclature

A = submerged object surface area

a = object radius

C_D = drag coefficient

d = immersed object diameter

D = bed diameter

D_{diff} = diffusion coefficient

D_{sphere} = sphere diameter

D_{tube} = tube diameter

$d_{s,v}$ = effective diameter of a particle

F_B = buoyant force

F_D = drag force due to air

$F_{D,P}$ = drag force due to particle impact

F_f = Force of friction

F_{Hood} = weight force of de-fluidized hood

F_n = Normal force

F_{sphere} = force on submerged sphere

F_W = weight force

g = gravitational acceleration

h = heat transfer coefficient

H_{hood} = height of hood

j = correction to the drag coefficient in a fluidized bed

k_p = mass transfer coefficient

k_w = wall correction factor

L = bed height

L_D = jet height

P = pressure

$R_{Large\ Sphere}$ = radius of large sphere

$R_{Small\ Sphere}$ = radius of small sphere

Re = Reynolds number

Re_r = Reynolds number based on relative velocity of particle to gas

S = specific surface of a particle

Sh = Sherwood number

U = gas velocity

U_{mf} – Minimum fluidization velocity

U_T = terminal velocity

u = gas velocity in x-direction

u_r = radial velocity

u_θ = tangential velocity

u^* = average velocity through a channel

v = gas velocity in y-direction

V = volume displaced by submerged object

V_{hood} = hood volume

Vol_t = total volume of particles

Greek Letters:

λ = thermal conductivity

θ = angle to which bed rises on submerged object

θ_2 = jet initial angle

Δ = shape correction factor

α = shape correction factor for Ergun equation

β = shape correction factor for Ergun equation

ε = voidage

ε_{mf} = voidage at minimum fluidization

υ_p = specific gravity of particles

υ_f = specific gravity of fluid

Φ = spherecity

ρ_{db} = dead bed density

ρ_f = fluid density

ρ_s = particle density

ρg = force per unit volume of de-fluidized hood

μ = gas viscosity

References

1. **Abrahamsen, A.R., and Geldart, D. (1980), "Behaviour of Gad-Fluidized Beds of Fine Powders Part 1: Homeogenous Expansion," Powder Technology, 26, pp. 35 – 46.**

2. **Albert, I., Tegzes, P., Albert, R., Sample, J.G., Barabasi, A.- L., Viscsek, T., Kahng, B., and Schiffer, P. (2001), "Stick – slip fluctuation in granular drag", Physical Review E, 64, pp.**

3. **Anjaneyulu, P., and Khakhar, D.V. (1995), "Rheology of a gas-fluidized bed," Powder Technology, 83, pp. 29-34.**

4. **Asif, M. (1998), "Segregation velocity model for fluidized suspension of binary mixture of particles," Chemical Engineering and Processing, 37, pp. 279 – 2876.**

5. **Batcheler, G.K (2000), An Introduction to Fluid Dymanics, Cambridge University Press, New York, NY.**

6. **Batchelor, G.K. (1988), "A new theory of the instability of a uniform fluidized bed," Journal of Fluid Mechanics, 193, pp. 75 – 110.**

7. **Bowen, B.D. and Masliyah, J.H. (1973), "Drag force on axisymmetric particles in Stokes' flow," The Canadian Journal of Chemical Engineering, 51, pp. 8-15.**

8. **Clift, R. and Gauvin, W.H. (1970), "The motion of particles in turbulent gas streams," Proc. Chemeca, 1, pp. 14.**

9. **Clift, R., and Rafailidis, S., (1993), "Interparticle stress, fluid pressure, and bubble motion in gas-fluidised beds," Chemical Engineering Science, 48, pp. 1575 – 1581.**

10. **Crowe, C., Sommerfield, M. and Tsuji, Y. (1998), Multiphase Flows with Droplets and Particles, CRC Press, New York.**

11. **Courant, R. and Hilbert, D. (1953), Methods of Mathematical Physics, Interscience Publishers Inc., New York.**

12. **Davidson, J.F., Harrison, D. and Guedes de Carvalho, J.R.F. (1977), "On the Liquidlike Behavior of Fluidized Beds," Annual Review of Fluid Mechanics, 9, pp. 55 – 86.**

13. **Duursma, G.R., Ockendon, J.R., and Hogan, S.J.. (1994), "Obstacle-induced voids in two dimensional gas fluidized beds," Chemical Engineering Science, 49, pp. 233 – 244.**

14. Ergun, S., and Orning, A.A.. (1949), "Fluid flow through randomly packed columns and fluidized beds," Industrial and Engineering Chemistry, 41, pp.1179 – 1184.

15. Fakhima, S., and Harrison, D.. (1980), "The voidage fraction near a horizontal tube immersed in a fluidised bed," Trans IChemE., 58, pp. 125 – 131.

16. Garim, M.M., Freire, J.T. and Goldstein, R.J. (1999), "Local mass transfer coefficients around a cylinder in a fluidized bed," Powder Technology, 101, pp.134 – 141.

17. Geldart, D. (1973), "Types of Gas Fluidization," Powder Technology, 7, pp. 285 – 292.

18. Gelperin, N.I. and Einstein, V.G. (1971). Heat Transfer in Fluidized Beds. In Davidson, J.F. and Harrison, D., Fluidization (pp. 471 – 540). New York: Academic Press.

19. German, Randall M. (1989), Particle Packing Characteristics, Metal Powder Industries Federation, Princeton NJ.

20. Gilbertson, M.A. and Eames, I. (2001), "Segregation patterns in gas-fluidized systems," Journal of Fluid Mechanics, 433, pp.347 – 356.

21. Glass, D.H., and Harrison, D. (1964), "Flow patterns near a solid obstacle in a fluidized bed," Chemical Engineering Science, 19, pp. 1001 – 1002.

22. Glicksman, L.R., Hyre, M., and Woloshun, K. (1993), "Simplified scaling relationships for fluidized beds," Powder Technology, 77, pp. 177 – 299.

23. Grace, J.R. and Hosney, N. (1985), "Forces on horizontal tubes in gas fluidised beds," Chem. Eng. Res. Des., 63, pp. 191 – 198.

24. Hager, W.R., and Schrag, S.D. (1976), "Particle circulation downstream from a tube immersed in a fluidized bed," Chemical Engineering Science, 31, pp. 657 – 659.

25. Harrison, D., and Grace, J.R. (1971). Fluidized Beds with Internal Baffles. In Davidson, J.F. and Harrison, D., Fluidization (pp. 599 – 626). New York: Academic Press.

26. Howard, JR (1989), Fluidized Bed Technology: Principles and Applications, Adam Hilger, New York.

27. **Huilin, L., Yurong, H., Gidaspow, D., Lidan, Y. and Yukun, Q. (2003), "Size segregation of binary mixture of solids in bubbling fluidized beds," Powder Technology, 134, pp. 86 – 97.**

28. **Jackson, Roy (2000), The Dynamics of Fluidized Particles, Cambridge University Press, New York.**

29. **Kim, S.W., Ahn, J.Y., Kim, S.D. (2005), "Heat transfer and bubble characteristics in a fluidized bed with immersed horizontal tube bundle," International Journal of Heat and Mass Transfer, 46, pp. 399 – 409.**

30. **Kulkarni, A. (1987), "Defluidized zone over a horizontally immersed tube in a fluidized bed," Chemical Engineering Science, 42, pp. 1245 – 1247.**

31. **Kurosaki, Y., Ishiguro, H., and Takahashi, K. (1988), "Fluidization and heat-transfer characteristics around a horizontal heated circular cylinder immersed in gas fluidized," International Journal of Heat and Mass Transfer, 31, pp. 349 – 358.**

32. **Lamb, H (1963), Hydrodynamics, Cambridge at the University Press.**

33. **Liu, F. and Orr, C. (1960), "Apparent Viscosity of Gas-Solid Fluidized Systems," Journal of Chemical and Engineering Data, 5, pp. 430 – 432.**

34. **Loew, Oded, Schmutter, Benjamin, and Resnick, William (1979), "Particle and Bubble Behaviour and Velocities in a Large-Particle Fluidized Bed with Immersed Obstacles," Powder Technology, 22, pp. 45 – 57.**

35. **Marzocchella, A., Salatino, P., Di Pastena, V. and Lirer, L. (2000), "Transient fluidization and segregation of binary mixtures of particles," AIChe Journal, 46, pp. 2175 – 2182.**

36. **Miyagi, Tosio, and Kamei, Takahiro (1983), "The standing vortex behind a disk normal to uniform flow at small Reynolds number," Journal of Fluid Mechanics, 134, pp. 221 – 230.**

37. **Molerus, O., Burschka, A., and Dietz, S. (1995), "Particle migration at solid surfaces and heat transfer in bubbling fluidized beds – I. Particle migration measurement systems," Chemical Engineering Science, 50, pp. 871 – 877.**

38. **Molerus, O., Burschka, A., and Dietz, S. (1995), "Particle migration at solid surfaces and heat transfer in bubbling fluidized beds – II. Prediction of heat transfer in bubbling fluidized beds," Chemical Engineering Science, 50, pp. 879 – 885.**

39. Nguyen, T.H. and Grace, J.R. (1978), "Forces on objects immersed in fluidized beds," Powder Technology, 19, pp. 255-264.

40. Oshitani, J., Trisakti, B. and Tanaka, Z. (2001), "Evaluation of fluidized particle flow by measurement of apparent buoyancy," Advanced Powder Technology, 12, pp. 95 – 104.

41. Peeler, J.P.K. and Whitehead, A.B. (1982), "Solids motion at horizontal tube surfaces in a large gas-solid fluidized bed," Chemical Engineering Science, 37, pp.77 - 82.

42. Perry, R.H. and Green, D.W. (1998), Perry's Chemical Engineers' Handbook, McGraw-Hill, New York.

43. Qiaoqun, S., Huilin, L., Wentie, L., Yurong, H., Lidan, Y. and Gidaspow, D., (2005), "Simulation and experiment of segregating/mixing of rice husk-sand mixture in a bubbling fluidized bed," Fuel, 84, pp. 1739 – 1748.

44. Rafilidis, S., Clift, R., Addis, E.J., Bagshaw, W., Cheesman, D.J., and Yates, J.G. (1992). The effect of horizontal tubes on bubble motion, in *Fluidization VII: proceedings of the Seventh Engineering Foundation Conference in Fluidization*, May 3 – 8, 1992, Brisbane, Australia, 875 – 883. New York, NY: Engineering Foundation.

45. Rahman, K. and Campbell, C.S. (2002), "Particle pressures generated around bubbles in gas-fluidized beds," Journal of Fluid Mechanics, 455, pp. 103 – 127.

46. Rao, Prakash (2009). *Buoyancy Considerations in a Fluidized Bed of Ground Particles*. M.S. Thesis. Rutgers, the State University of New Jersey: U.S.A.

47. Rathbone, R.R., Ghadiri, M., and Clift, R., (1989), "Measurement of particle velocities and associated stresses on immersed surfaces in fluidized beds," in Fluidization VI, Engineering Foundation, New York, pp. 629 – 635.

48. Rees, A.C., Davidson, J.F., Dennis, J.S. and Hayhurst, A.N. (2005), "The rise of a buoyant sphere in a gas-fluidized bed," Chemical Engineering Science, 60, pp. 1143 – 1153.

49. Rees, A.C., Davidson, J.F., Dennis, J.S., Fennell, P.S., Gladden, L.F., Hayhurst, A.N., Mantle, M.D., Muller, C.R., and Sederman, A.J., (2006), "The nature of the flow just above the perforated plate distributor of a gas – solid fluidized bed, as imaged using magnetic resonance," Chemical Engineering Science, 61, pp. 6002 – 6015.

50. Rees, A.C., Davidson, J.F., Dennis, J.S. and Hayhurst, A.N. (2007), "The apparent viscosity of the particulate phase of the bubbling gas-fluidized beds: A comparison of the falling or rising sphere technique with other methods," Chemical Engineering Research and Design, 85, pp.1341 – 1347.

51. Rietama, K (1991). The Dynamics of Fine Powders, Elsevier Applied Science, New York.

52. Rios, G.M., Tran, K.D., and Masson, H., (1986), "Free object motion in a gas fluidized bed," Chem. Eng. Commun., 47, pp. 247 – 272.

53. Shenoy, A.R, and Kleinstreuer, C., (2008), "Flow over a thin circular disk at low to moderate Reynolds numbers," Journal of Fluid Mechanics, 605, pp. 253 – 262.

54. Taneda, S. (1979), "Visualization of Separating Stokes Flows," Journal of the Physical Society of Japan, 46, pp. 1935 – 1942.

55. Tardos, G.I., Khan, M.I., and Schaeffer, D.G., (1998), "Forces on a slowly rotating, rough cylinder in a couette device containing a dry, frictional powder," Physics of Fluids, 10, pp. 335 – 341.

56. Tee, S., Mucha, P.J., Brenner, M.P. and Weitz, D.A. (2008), "Velocity fluctuations in a low Reynolds-number fluidized bed," Journal of Fluid Mechanics, 596, pp. 467 – 475.

57. White, Frank (1974). Viscous Flow, McGraw Hill Book Company, New York.

58. Umekawa, H., Ozawa, M., Takenaka, N. and Matsubayashi, M., (1999), "Visualization of bed material movement in a simulated fluidized bed heat exchanger by neutron radiography," Nuclear Instruments and Methods in Physics Research Section A, 424, pp. 77-83.